FORSCHUNGSZENTRUM JÜLICH GmbH

Institut für Kernphysik

The Reaction $pd \rightarrow {}^3He\ \eta$ at 200 MeV Excess Energy

Martin Waters

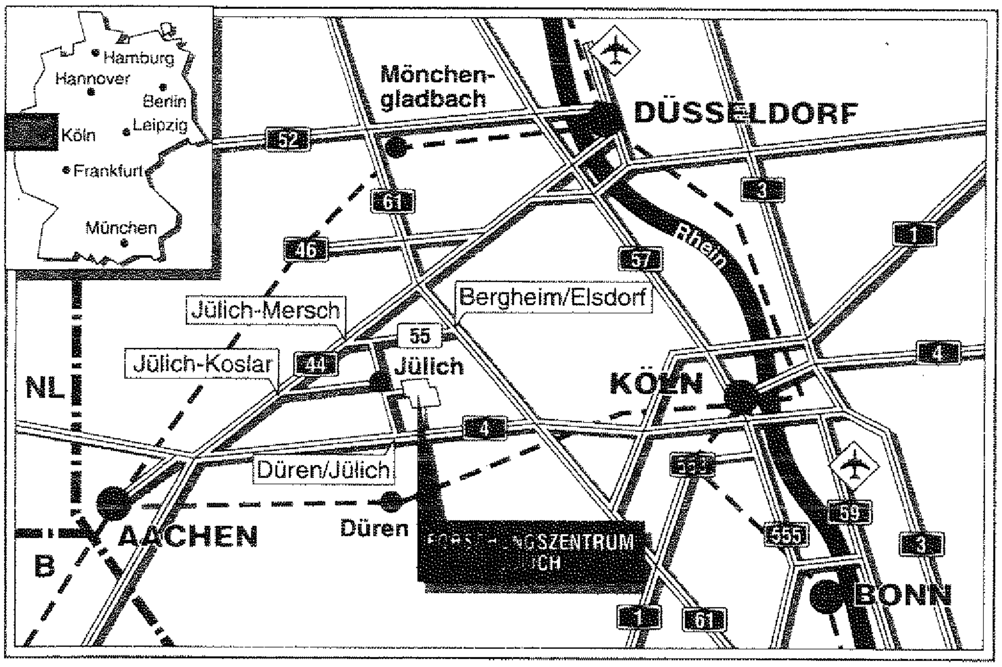

Berichte des Forschungszentrums Jülich ; 2917
ISSN 0944-2952
Institut für Kernphysik Jül-2917
D 5 (Diss. Universität Bonn)

Zu beziehen durch: Forschungszentrum Jülich GmbH · Zentralbibliothek
D-52425 Jülich · Bundesrepublik Deutschland
Telefon: 02461/61-6102 · Telefax: 02461/61-6103 · Telex: 833556-70 kfa d

The Reaction $pd \rightarrow {}^3He\ \eta$ at 200 MeV Excess Energy

Martin Waters

Contents

Preface

This work was carried out within the scope of the PROMICE[1] research program [20] at the CELSIUS [12] cooler-storage ring of the The Svedberg Laboratory in Uppsala, Sweden. The aim is to study the fundamental mechanisms for production of mesons in light ion collisions and their interaction with nuclei and nucleons. The role of different resonances in nuclei as well as meson-meson interactions will be examined. In order to enable even measurements of rare mesonic decays, the PROMICE detector setup will later be extended to the full 4π WASA[2] apparatus [22]. PROMICE/WASA is a collaboration between laboratories in Japan, Poland, Russia, Sweden and Germany. The present stage of the setup has been used to measure η production in p-d collisions by detection of the recoil nucleus in the channel d(p,^{3}He)η at beam energies of T_p=1250 and 1276 MeV using an internal cluster target.

[1]PROMICE=**PR**oduction **O**f **M**esons **I**n **CE**LSIUS
[2]WASA=**W**ide **A**ngle **S**hower **A**pparatus

He who has come so far that he no longer makes mistakes,
has stopped working.

Max Planck

Chapter 1

Motivation

1.1 Introduction

The dominant model of the nucleon-nucleon interaction involves the exchange of mesons between the nucleons (boson-exchange models). At low energies, the long-range pion exchange dominates (one-pion-exchange model), whereas at higher energies heavier mesons ($\eta, \rho, \omega, \eta'$ ...) become increasingly important.

High intensity and high precision medium-energy accelerator facilities (SATURNE, IUCF, TRIUMF, CELSIUS, LAMPF, PSI, COSY ...) have opened excellent opportunities to study the production of mesons and their interaction with the nuclear medium. Phase-space cooling of the beam leads to very good momentum resolution combined with small emittance, and the use of internal windowless targets provides high luminosity with (i) a minimum of background from secondary interactions with non-target associated particles, (ii) acceptable perturbation to the stored beam, (iii) acceptable gas load on the ring, and (iv) minimized multiple Coulomb scattering. These properties are particularly useful for precision experiments aiming at measurements close to the nucleon-nucleon threshold, where the total energy is used to produce the otherwise virtual exchange-mesons on the mass shell. The number of participating angular momentum states is restricted, and thus a comparison of experimental data with theoretical predictions is more stringent at low energies since there are fewer degrees of freedom to cope with.

The role of mesons heavier than the pion as exchange particles has received increasing attention. A comparative study of the interaction of various mesons with nuclear matter could reveal new phenomena which might contribute to a better understanding of intra-nuclear degrees of freedom. Furthermore the theoretical models which have been derived from pion production can be tested with respect to their ability to explain the interactions of heavier mesons with nuclear matter. Following pions, the η meson with a mass of (547.3 ± 0.1) MeV/c^2 [31] is the next heaviest meson to study. Due to its short lifetime ($\tau = 5.5 \cdot 10^{-19}$ s), the η cannot be used as a separate beam probe like the pion ($\tau = 8.4 \cdot 10^{-17}$ s). The high peak to background ratio found for η-production in proton-deuteron scattering [31] led to the idea of creating a tagged η beam. Investigations of the interaction of η mesons with nuclear matter are foreseen in the COSY experiments [7].

In η-production reactions, two-body final states are an attractive object to study since the measurement of only one particle in the exit channel together with the kinematical constraints from the known beam and target parameters provides sufficient information about the other particle or resonance.

1.2 Production of η mesons in proton-deuteron collisions

One of the first extensive studies on the production of neutral mesons in the reaction pd$\rightarrow$^{3}HeX was carried out in 1973 by Brody et al. at the CERN[1] missing mass spectrometer [8]. At that time not many of the predicted states below 1 GeV/c^2 had reliably been established. Within the scope of their systematic search for neutral mesons in this mass region, they reported[2] a mass for the η of (548 ± 1) MeV/c^2. The most recent result was given by F. Plouin et al. [31] in 1992. They state (547.3 ± 0.1) MeV/c^2 for the η mass. The particle data group [29] reports a value of (547.45 ± 0.19) MeV/c^2.

In 1985 Berthet et al. [2] presented results of a measurement of the reactions pd$\rightarrow$^{3}Heη and pd$\rightarrow$^{3}Heπ° at $\theta_\pi = \theta_\eta = 180^\circ$. The excitation curve shown in figure 1.1 was measured at SATURNE with the SPES IV spectrometer tuned to detect ^{3}He at 0°. The oscillatory pattern seen here is one of the most direct evidences for three-body mechanisms in p-d capture reactions since it reflects the importance of the S_{11} N*(1535) resonance near the η threshold as well as influences of higher baryonic resonances[3] like the P_{11} N*(1710). These resonances are known to have large branching ratios to the η-nucleon channel.

Another feature of this excitation curve is the depression of the π^+ cross section at the energy corresponding to the threshold for η-production. This and the fact that the backward deuteron tensor analysing power t_{20} of the reaction $\vec{\mathrm{d}}$p$\rightarrow$^{3}Heπ°, measured by Kerboul et al. [23], exhibits a narrow peak at the η threshold, points to a correlation, which could be due to a coupling of the πN and ηN channels.

Berger et al. measured the $\vec{\mathrm{d}}$p$\rightarrow$^{3}Heη reaction very near threshold [3] and found a forward-backward cross-section ratio close to 1 for ^{3}He final state center-of-mass momenta up to $\simeq 50$ MeV/c, in contrast to the analogous π° data, which display a very anisotropic behaviour [23]. This indicates the strong influence of the p-wave $\Delta(1232)$ resonance in π°-production, whereas the η-production is dominated by the s-wave N*(1535) resonance. Disregarding internal energy, the mass of the pion-

[1] Centre Européenne pour la Recherche Nucléaire, Geneva

[2] Among five different missing mass specifications, the one with the smallest error has been cited [8].

[3] The arrows in figure 1.1 indicate the thresholds for the reactions pd$\rightarrow$dX where X stands for the respective resonance.

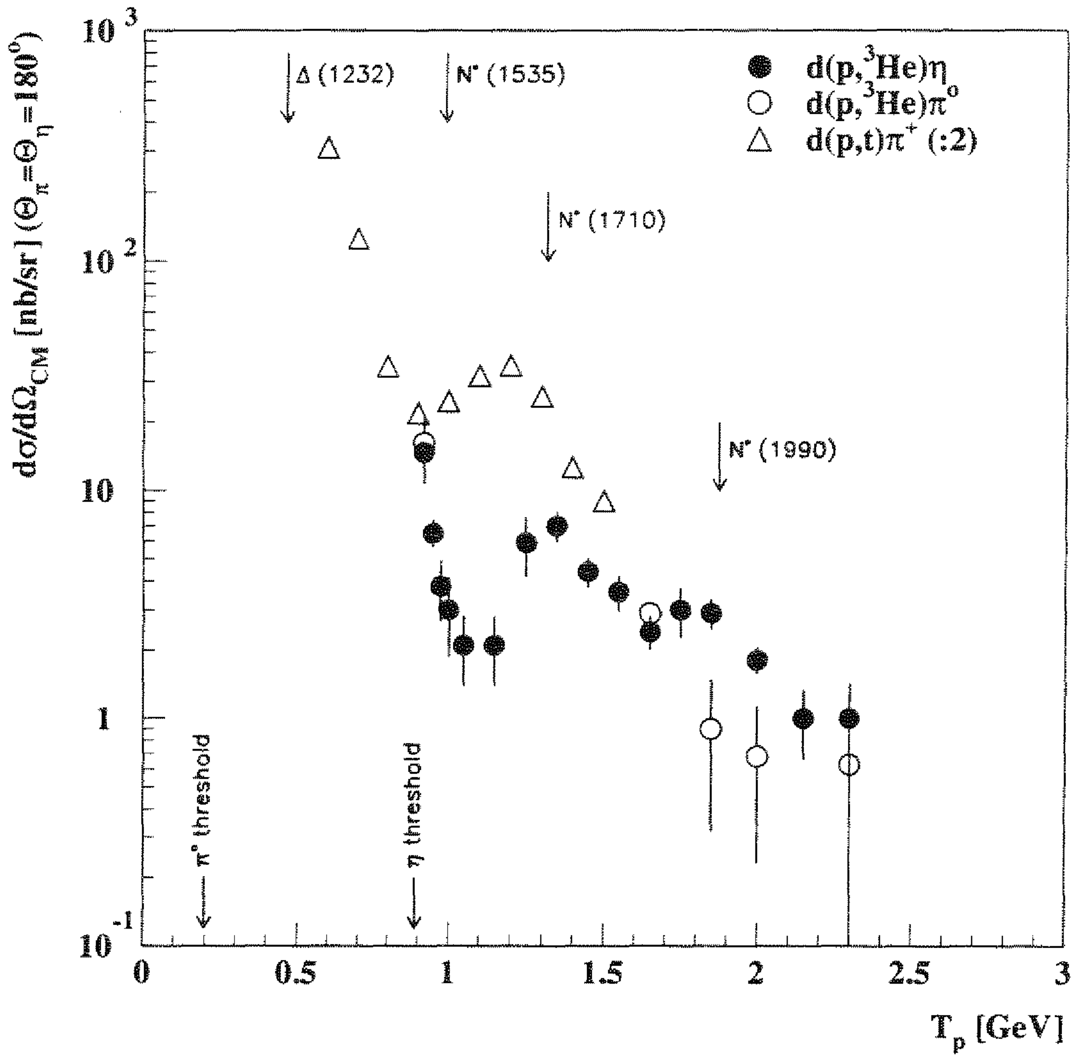

Figure 1.1: Excitation curve [2] of pd$\rightarrow$^{3}Heη and pd$\rightarrow$^{3}Heπ° for $\theta_\pi = \theta_\eta = 180°$.

nucleon system is only 160 MeV less than the mass of the Δ, and the mass of the η-nucleon system is as close as 50 MeV to the N* mass. Therefore these broad resonances will dominate the production dynamics near threshold.

Another striking feature of η production in p-d collisions was reported by Plouin et al. [30]. The threshold excitation function for the reaction pd$\rightarrow$^{3}HeX shown in figure 1.2 was obtained by focussing the SPES IV spectrometer on the highest kinematically allowed mesonic mass produced in association with ^{3}He for each incident proton energy. Two prominent peaks have been observed corresponding to π° and η production at high rates with a surprisingly high peak to background ratio. The η cross section at threshold was found to be of the same order of magnitude as the one for π°-production.

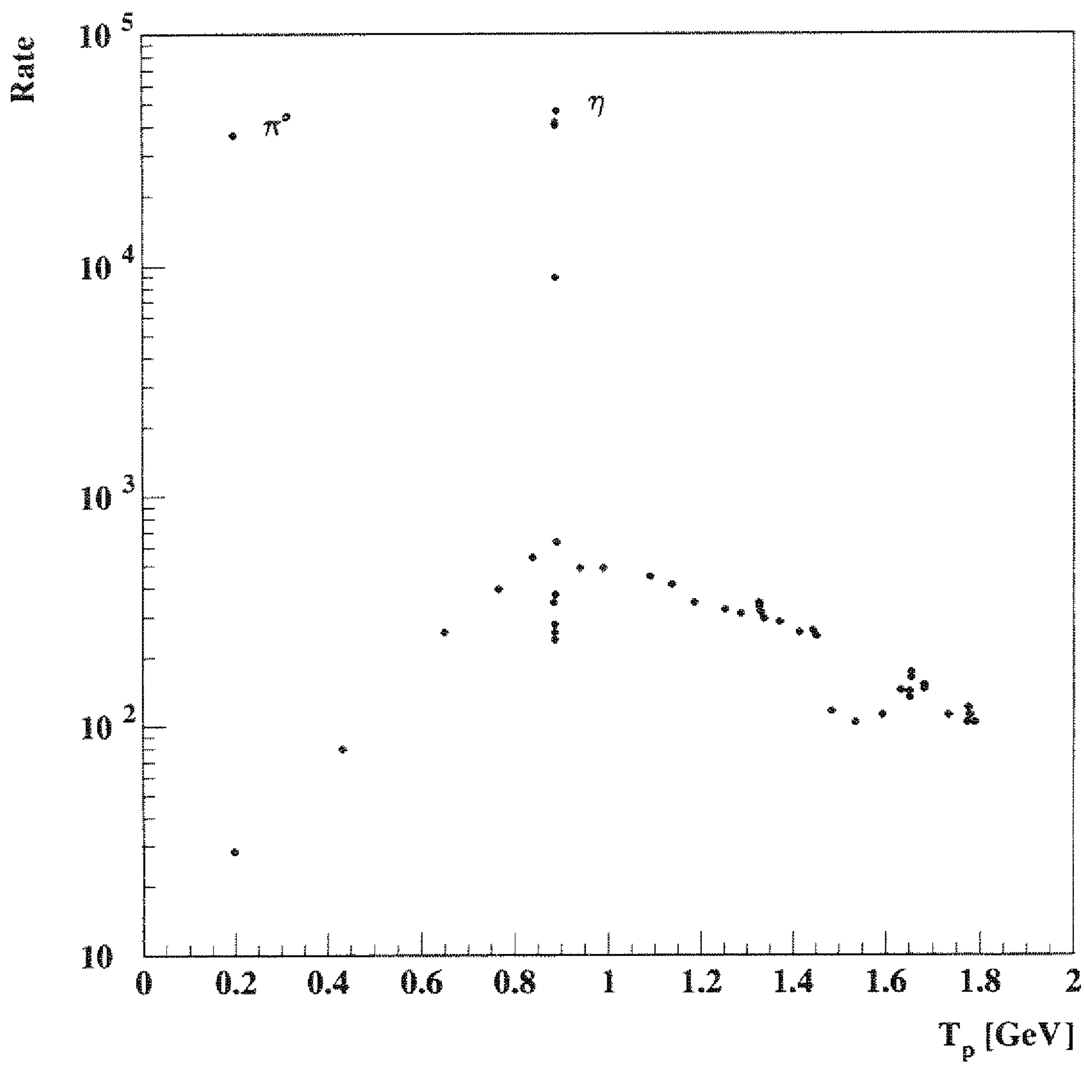

Figure 1.2: Threshold excitation curve [30] of pd→^{3}HeX.

1.3 Theoretical approaches

Basically two theoretical calculations have been performed to explain the experimental data on η-production from proton-deuteron collisions. Both are based on models previously formulated for the reaction pd→^{3}Heπ°.

1.3.1 Extensions of calculations for π°-production

In 1988, Laget and Lecolley presented a microscopic, fully relativistic calculation without any free parameters based on six diagrams, shown in figure 1.3, contributing to η production by p-d capture, which are summed coherently [25]. Compared to the

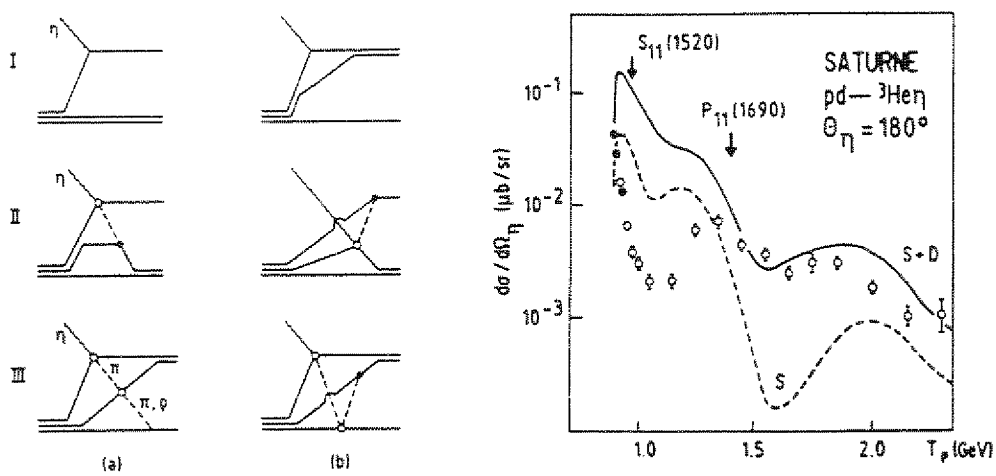

Figure 1.3: Relevant diagrams used for the calculations of [25] and result of the calculations. The dashed line includes only the S-wave part, the full curve S- and D-part of the wave function of the nucleon which interacts with the η. Data from references [2] (open circles) and [3] (full circles). I, II and III show one-, two- and three-body meson exchange graphs, respectively.

π° calculation, they included the elementary πN→ ηN amplitude, the partial waves of which are parametrized in terms of the various N* resonances. They claim that plane-wave and two-body mechanisms are suppressed due to the higher momentum transfer in η-production compared to π°-production because of the larger mass of the η, giving cross sections which are too small by two orders of magnitude. Therefore three-body mechanisms have been considered which allow the momentum transfer to be shared between all the nucleons, thus leading to a larger scattering amplitude. In addition, the amplitude is enhanced since an exchange meson in the dominating meson double-scattering process can be produced on-shell in contrast to other three-nucleon mechanisms where baryonic resonances decay by emission of two virtual mesons. As the right hand side of figure 1.3 indicates, their theoretical results are not in good agreement with the experimental points at lower energies.

In the year following this publication, Germond and Wilkin [16] presented results using the graphs displayed in figure 1.4. In this, the graph on the left hand side was included in the calculation of the upper vertex of the graph on the right hand side. The ^{3}He nucleus was assumed to be a two-body cluster (p-d or N-d*). The analysis included π, η and ρ exchange as well as D-state effects. The result underestimates the reaction rate of pd→^{3}Heη, and the deuteron tensor analyzing power t_{20} is only weakly reproduced. A problem in calculating this reaction is that huge momentum

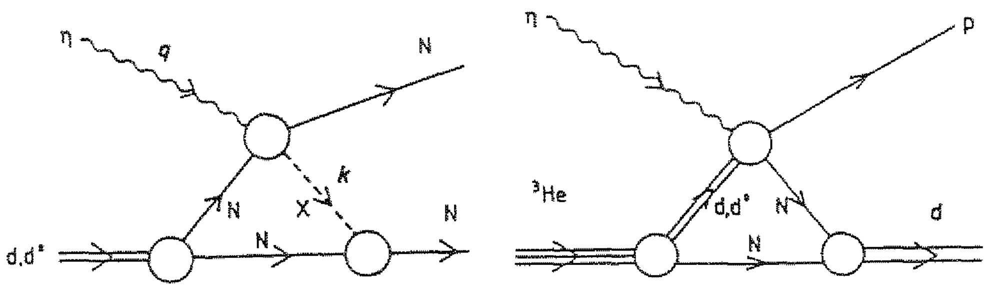

Figure 1.4: Graphs used in the calculations by Germond and Wilkin.

transfers (~13.5 fm^{-1} or 2.66 GeV/c) are involved, and thus the model is highly sensitive to poorly known wave functions. The bad agreement with the experimental data is believed to be due to the lack of three-body terms.

1.3.2 An empirical model

Kilian and Nann [24], and Germond and Wilkin [6], noticed that the meson production cross section might be enhanced by the kinematic conditions. They consider a two-step sequential mechanism of meson production as illustrated in figure 1.5. In the first step, a light intermediate particle is produced from a nucleon-nucleon

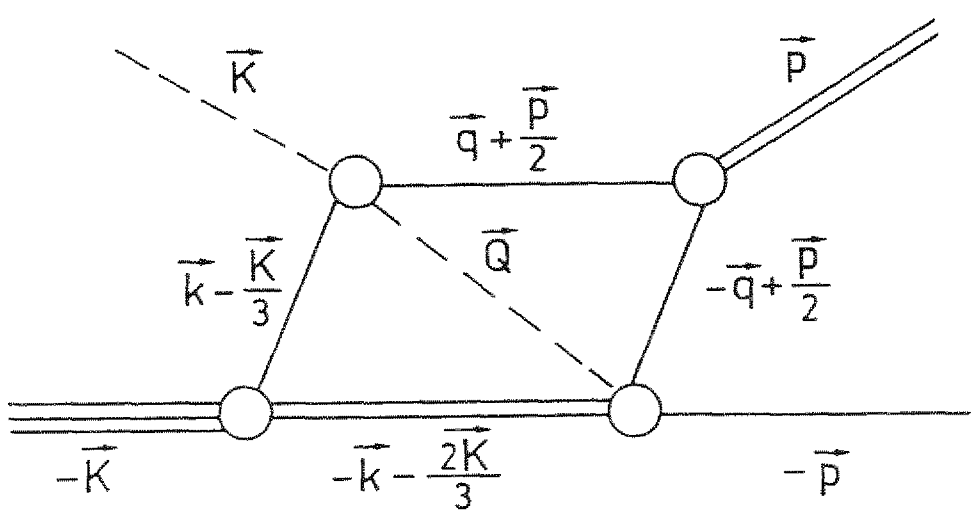

Figure 1.5: Kinematical relations in the empirical two-step reaction model [6].

collision. By interaction with a second nucleon of the same target, the intermediate particle produces the outgoing meson. These two steps combine for instance [24] like:

$$\begin{array}{ll} \text{Step A:} & \mathrm{p} \; + \mathrm{p} \rightarrow \pi^+ + \; \mathrm{d} \\ \text{Step B:} & \underline{\pi^+ + \mathrm{n} \rightarrow \mathrm{X}^\circ \; + \; \mathrm{p}} \\ \text{Total:} & \mathrm{p} \; + \mathrm{d} \rightarrow \mathrm{X}^\circ \; + {}^3\mathrm{He} \end{array}$$

The point is that if the velocities of the baryons produced in each step are matched, i.e. their relative energy ϵ is close to zero, then the fusion to a three-nucleon cluster will be enhanced since the fusion probability P increases with smaller excess energy ϵ compared to the binding energy[4] E_b of the three-body system:

$$P = \exp(-\epsilon/E_b).$$

The momentum transfer in each reaction step is of the order 900 MeV/c, i.e. 4.5 fm^{-1}. The short range of this field (corresponding to $r \sim \frac{\hbar}{p} = 0.22$ fm) is quite small compared to the dimensions of a deuteron which has a radius of the order 4.3 fm [27]. This suggests the assumption that the reaction basically proceeds as a sequence of on-shell processes, and there is no need for large Fermi momenta. Furthermore, a bump in the excitation function has, according to this model, nothing to do with a resonance.

In the example of a two-step process given above, forward going intermediate pions decrease the threshold for this two-step reaction to T_p=897 MeV compared to the nucleon-nucleon threshold of T_p=1254 MeV. This two-step threshold is as close as 6 MeV to the threshold for the over-all reaction pd$\rightarrow$^{3}Heη which is at T_p=891 MeV. This means that the reaction essentially proceeds as a sequence of on-shell processes.

Kilian and Nann performed Monte Carlo calculations on several reactions where the result of reaction step A was used as input for step B. Average Fermi momenta of 150 MeV/c were included as well as energy dependent differential cross sections. They found that the relative energy ϵ between the final baryons becomes small close to threshold giving rise to an increased fusion probability, and hence they obtained a rather narrow enhancement of the excitation function for the total pd$\rightarrow$^{3}Heη cross section close to threshold due to the "velocity matching".

A possibility to single out the importance of resonances in comparison to the two step processes would be to look at reactions involving three particles in the exit channel such as pd$\rightarrow$pdX$^\circ$ or pd$\rightarrow$ndX$^+$. If the cross sections can be well described by two-step process kinematics, then Dalitz plots of the squared masses of subsystems will show density modulations which differ from the shapes resonances would create.

[4]The fusion of a proton and a deuteron to ^{3}He releases 5.49 MeV.

1.4 Properties of the π° and η in comparison

In table 1.1 some properties of the η meson are listed in comparison to the neutral pion, both members of the SU(3) pseudoscalar meson nonet ($J^P = 0^-$). In contrast

Particle	π°	η
Mass [MeV/c^2]	134.9739 ± 0.0006 [29]	547.3 ± 0.1 [31]
$I^G\left(J^{PC}\right)$	$1^-(0^{-+})$	$0^+(0^{-+})$
Principal decay modes	2γ (98.8 %)	2γ (38.9 %) $3\pi^\circ$ (31.9 %) $\pi^+\pi^-\pi^\circ$ (23.6 %) $\pi^+\pi^-\gamma$ (4.88 %)
Main quark content	$(u\bar{u} - d\bar{d})/\sqrt{2}$	$(u\bar{u} + d\bar{d} - 2s\bar{s})/\sqrt{6}$

Table 1.1: Some properties of the η in comparison to the neutral pion.

to the isovector π°, the η is isoscalar and therefore couples only to ($I = \frac{1}{2}$)-baryons, the N* resonances, because of isospin conservation in strong interactions at the ηNN-vertex. Thus the S_{11} N*(1535) and the P_{11} N*(1710) resonances are the dominating low mass baryonic states coupled strongly to the ηN channel.

Furthermore the η has strange quark contents in its wave function (and possibly even a gluonic component). The η - as well as the η' - meson is a mixture of the pure SU(3) states

$$\begin{aligned} \eta_1 &= (u\bar{u} + d\bar{d} + s\bar{s})/\sqrt{3} \quad \text{and} \\ \eta_8 &= (u\bar{u} + d\bar{d} - 2s\bar{s})/\sqrt{6} \end{aligned}$$

which can be written as

$$\begin{pmatrix} \eta \\ \eta' \end{pmatrix} = \begin{pmatrix} \cos\theta & -\sin\theta \\ \sin\theta & \cos\theta \end{pmatrix} \begin{pmatrix} \eta_8 \\ \eta_1 \end{pmatrix}.$$

In this, θ denotes the mixing angle which is of the order [17, 32]

$$\theta = -20^\circ,$$

so that the η consists of 94 % η_8 - hence the entry for the dominant quark content in table 1.1. Unlike the π°, the η is symmetric in its u- and d-quark content and thus has positive G-parity in contrast to the pion.

Chapter 2

Experimental setup

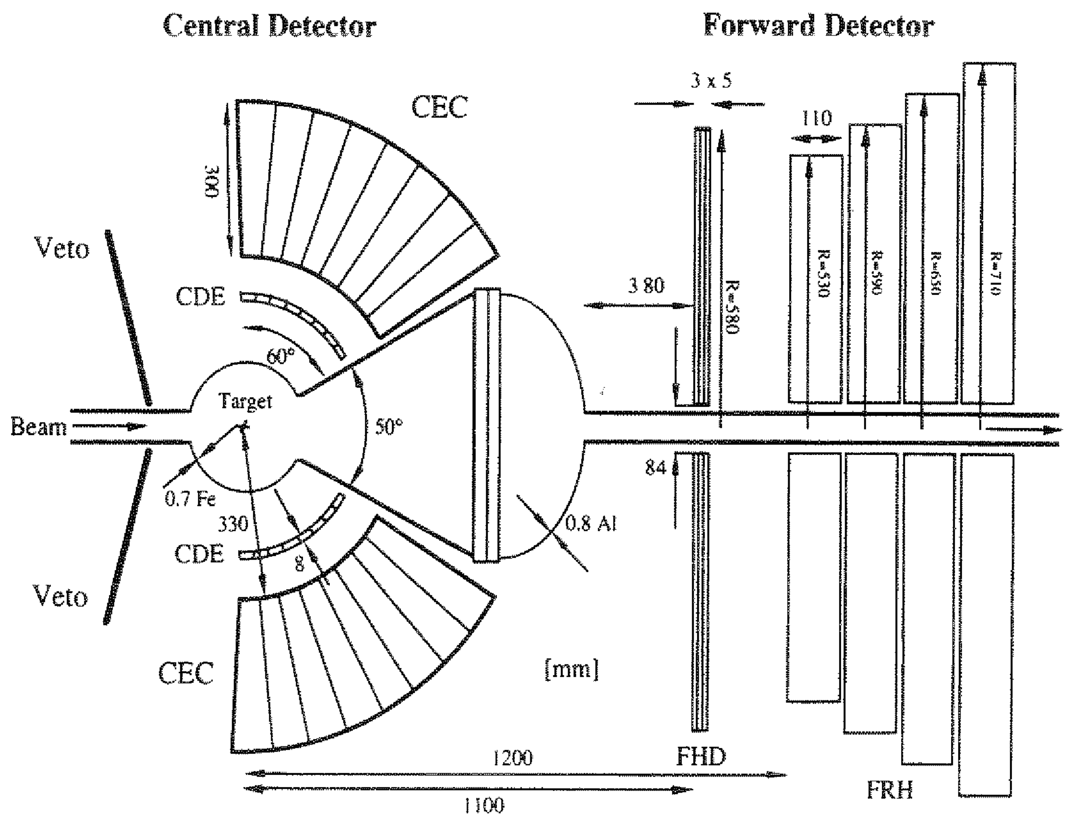

Figure 2.1: Top view cross section of the PROMICE setup as used.

Figure 2.1 shows the PROMICE detector setup used in the experiment described here. The CELSIUS proton beam enters from the left and interacts in the center of the cylindrical scattering chamber with deuteron (proton) clusters which are injected vertically (source on the top).

2.1 The CELSIUS beam

The CELSIUS storage ring is fed with ions from the Gustav Werner synchrocyclotron [21] at the The Svedberg Laboratory; the injection energy for protons is 48 MeV, using stripping injection. With a magnetic rigidity of 7 Tm, CELSIUS is able to store particles with momenta of up to 2.1 GeV/c per unit charge, corresponding to a maximum[1] proton kinetic energy of 1360 MeV. An electron cooler has been installed in order to increase the phase space density and to compensate target heating of the beam. The cooled beam has a momentum resolution of $\Delta p/p < 2 \cdot 10^{-4}$, the uncooled beam a relative momentum resolution of $\sim 2 \cdot 10^{-3}$. The electron cooler accelerates electrons up to a kinetic energy of 300 keV, thus limiting cooling to beam energies less than 550 MeV per nucleon.

2.2 Target stand

The cluster jet is produced by pressing gas under pressure-temperature conditions close to the transition point to liquid through a cooled thin nozzle. A cooled skimmer and a set of collimators is used to define the width of the target beam. A cryogenic beam dump finally collects the clusters. At the interaction point, 25 cm away from the nozzle, the clusters are ovally shaped with a cross section of 8 mm along and 5 mm vertical to the beam [13]. The target thickness is typically about $3 \cdot 10^{14}$ atoms/cm^2. With a beam width of a few millimeters and $\sim 10^{10}$ protons stored in the ring, a luminosity of 10^{30} cm^{-2} s^{-1} can be achieved with a minimum of background from secondary interactions with non-target associated particles, acceptable perturbation to the stored beam and acceptable gas load on the ring - as is a general advantage of windowless internal targets apart from the minimization of multiple Coulomb scattering. The half-life obtained for stored protons at, e.g., 600 MeV is ~20 minutes. Differential pumping along the cluster beam, instead of along the circulating beam, allows for wide angle detection of particles emitted from the interaction vertex. The scattering chamber of the CELSIUS cluster jet target opens in a forward cone with a thin 800 μm aluminium window allowing for scattering angles of up to 25° relative to the beam direction.

2.3 Central detector

The scattering chamber is surrounded by the central detector (CD) consisting of two boxes with 7×8 pyramidally shaped CsI(Na) crystals, each box nearly forming a 60° × 60° spherical sector (see figure 2.2). The crystals are 30 cm long ($\hat{=}16X_0$, X_0 = radiation length) and have a front face of 4.2×4.2 cm^2. For this experiment

[1] According to calculations, the magnetic field in the CELSIUS magnets could be increased from 1.0 T to 1.2 T without severe saturation effects, which would increase the maximum possible kinetic energy of protons to 1.75 GeV. An application for subsidy has been submitted.

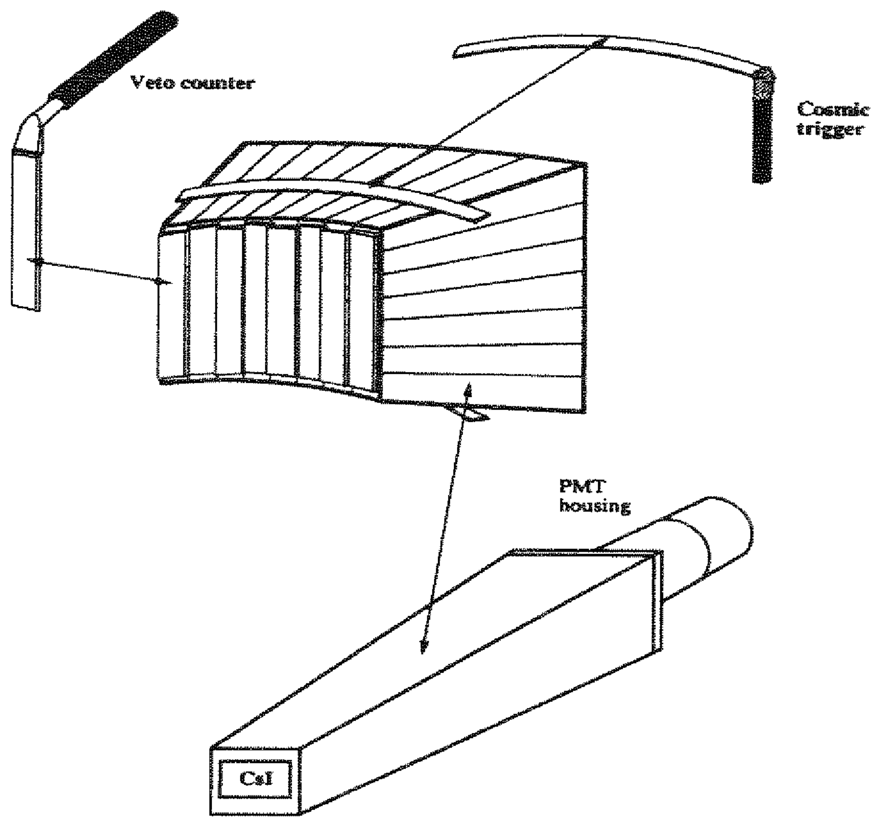

Figure 2.2: Sketch of a central detector box containing 7 × 8 CsI crystals. Also plastic scintillator veto counters are shown as well as scintillator strips to provide a trigger for calibration using cosmic muons.

the boxes have been positioned symmetrically centered at ±60° to the beam axis. Their purpose is mainly the detection of photons with high energy resolution, but also measurement of charged particles. These calorimeters are called CEC, which stands for Central Electromagnetic Calorimeter. Using conventional photomultiplier readout, the relative energy resolution is expected to be approximately 6 % (FWHM) for photons with energies of 50 MeV and above.

In front of each CsI box, a cylindrical plane of 8 vertically positioned 8 mm thick plastic scintillators is mounted to provide a veto for charged particles entering the CsI crystals, named CDE=Central Delta Energy counter. Upstream of the scattering chamber, plastic scintillator veto counters are mounted in order to veto all online triggers if a charged particle passes the target region outside the beam tube. The CsI crystals of the central detector are completely screened by these counters.

In figure 2.2, two plastic scintillator strips on top and below the CsI box are shown. These counters have been used in a first calibration using cosmic muons [35].

2.4 Forward detector

Charged particles which are emitted in a forward cone at laboratory angles between 3° and 23° with respect to the beam axis are measured in the PROMICE/WASA forward detector.

2.4.1 The forward trigger hodoscope

The geometry

At a distance of 1.1 m to the interaction vertex, three layers of 5 mm ±10 % thick plastic scintillators are mounted, named **F**orward **H**odoscope (FHD). Figure 2.3 shows a schematic view of the forward hodoscope. In reality, there is only a space of 5 mm left between the planes, but for the sake of clearness this representation has been chosen. The first two planes of this hodoscope are composed of 24 scintillators whose shape is described by archimedic spirals, i.e. the boundaries are described in polar coordinates by

$$\varphi_{\mathrm{i}}(r) = \Delta\varphi \cdot \mathrm{i} \pm k \cdot r, \quad \mathrm{i} = 1, 24$$

with

$$\begin{aligned}
\Delta\varphi &= \varphi_{\mathrm{i+1}} - \varphi_{\mathrm{i}} = 15^\circ, \\
k &= \varphi_{\mathrm{max}}/r_{\mathrm{max}}, \\
\varphi_{\mathrm{max}} &= 180^\circ, \\
r_{\mathrm{max}} &= 58 \text{ cm},
\end{aligned}$$

chosen in the present design. In this φ_{i} is the azimuthal angle for element number i, and r is the distance to the center of the detector, all measured in the detector plane. The positive sign is valid for the description of the "left" bent elements, the negative for the "right" bent, respectively. The third plane consists of 48 triangle shaped scintillators, two of these matching one wedge in the FRH.

At the maximum radius the outer edge of a scintillator is geometrically given by the straight connection of the end points of the spirals describing the edge curves of the element. The light guides which are glued to these straight ends have a rectangular cross section and a thickness of 6 mm. Since the photomultipliers used have a circular cathode with an effective diameter of 46 mm, the light guides are adiabatically carried over into a circular surface which matches the photomultiplier window.

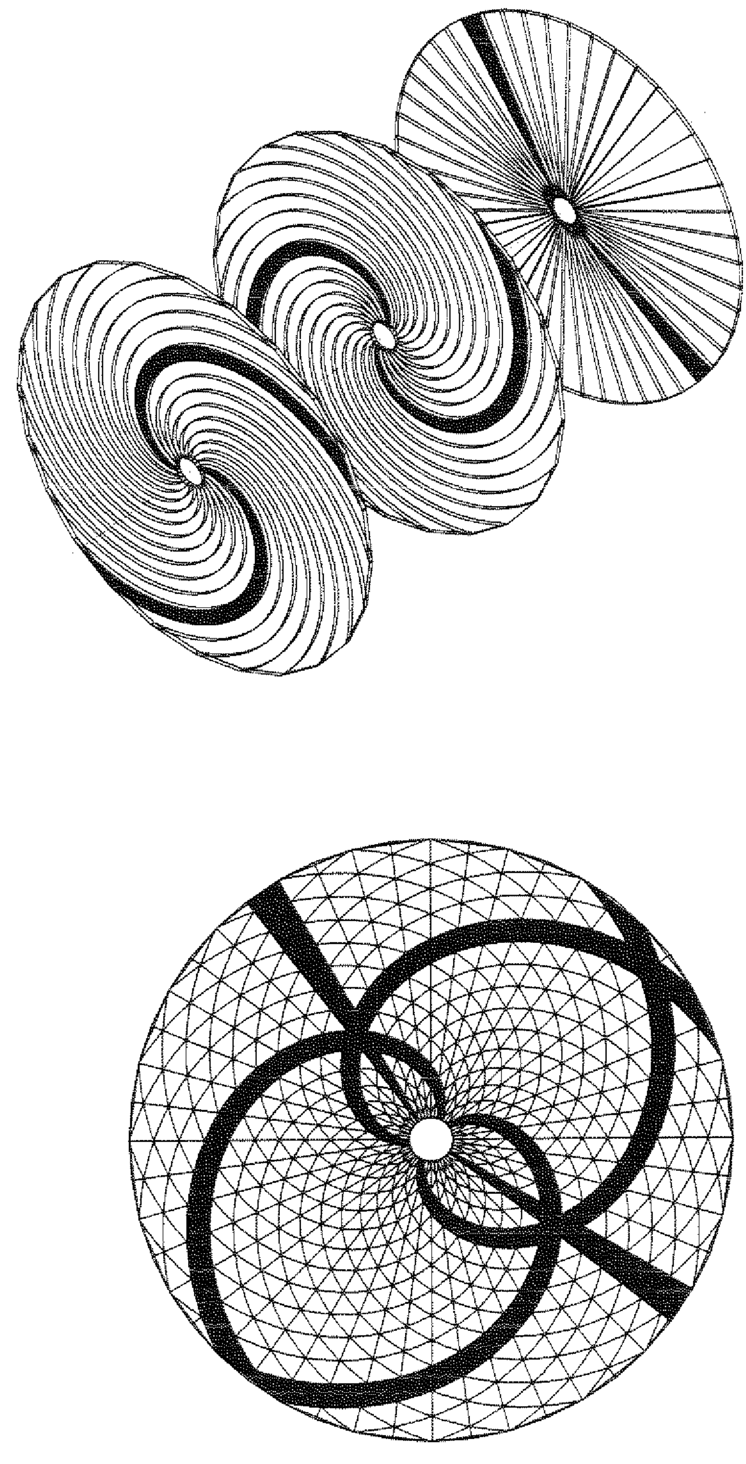

Figure 2.3: Schematic view of the forward hodoscope.

Features of this setup

Since all planes are completely symmetric under rotations around the beam axis in steps of the azimuthal angular width of an element, the forward detector plane is hence divided up into equal, radially symmetric areas. Therefore, having no polarization, all individual scintillators in a plane are exposed to the same integral counting rate since they cover the same part of the phase space. This is an advantage regarding the on-line setup, e.g. in view of the dead time.

In figure 2.3 some elements are highlighted which indicates hits by two charged particle tracks, the coincidence between signals from each plane defining a cell being the overlap area of the corresponding scintillator modules (in total 1104 active pixels, due to the hole for the beam tube which is 84 mm in diameter). By such a combination of the signals from all three planes it is off-line possible to determine the direction of a charged particle track in the forward detector and to resolve multi-hit ambiguities.

Furthermore, the hodoscope gives a fast online multiplicity and timing trigger, and allows for $\mathrm{d}E/\mathrm{d}x$ measurements. This device can even be used as a fast kinematic filter by on-line determination of polar and azimuthal angles of charged particle tracks because the hit radius is proportional to the difference between the hit right and left bent scintillators, and the azimuthal angle is related to their sum.

The solid angle resolution

The radial height of all pixels is constantly equal to

$$\Delta r = \frac{\Delta\varphi}{k} = 4.83 \text{ cm}$$

and their azimuthal width equal to

$$\Delta\varphi = 7.5^\circ,$$

taking the third FHD plane into account. Thus one might ask how the three-dimensional phase-space volume $\mathrm{d}^3r = r^2\mathrm{d}r\mathrm{d}\cos\theta\mathrm{d}\phi$ respectively the solid angle covered by a pixel behaves at different radii and distances of the detector to the interaction vertex, r being the distance to the vertex, ϕ the azimuthal and θ the polar angle in the spherical laboratory system coordinates. Illuminating the whole forward hodoscope with particle tracks, the momentum vectors of which are isotropically distributed in a sphere (center-of-momentum system), a pixel hit statistics like figure 2.4 will be obtained. Here the number of hits, normalized to the phase space distribution on input, in each one of the 23 pixels of a straight FHD element is plotted for several distances of the detector from the vertex. Small pixel numbers correspond to large radii[2]. Since the phase space density is constant in this case, the

[2]In this simulation the detector has been regarded as one plane with zero thickness containing 1104 pixels which are formed by the overlap of all the three detector planes.

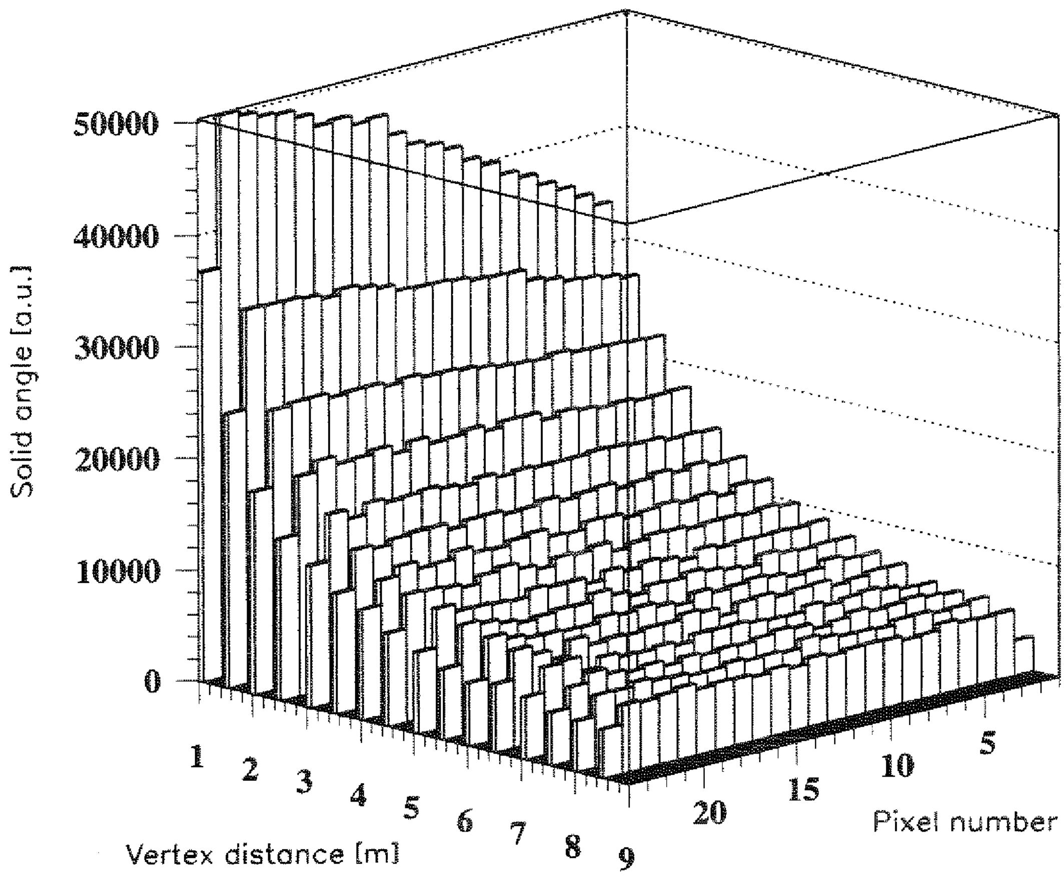

Figure 2.4: Laboratory solid angle covered by the 23 pixels in a forward hodoscope wedge at different distances to the vertex. Small pixel numbers correspond to large radii.

normalized number of hits per pixel is directly related to the phase space volume or solid angle, and according to figure 2.4 one concludes that, at small vertex distances, the solid angle covered by the respective pixels increases to small radii (high pixel numbers). This implies that, at a distance of 1.1 m to the target chosen for this experiment, the highest resolution is at outer pixels, i.e. at large scattering angles. This is very suitable since in the reaction studied here the maximum statistics is expected at large laboratory scattering angles around 16.6° (Jacobian). However, at large distances to the interaction vertex, of course all pixels cover approximately the same solid angle in the unit sphere.

At the present stage of the experimental setup, the FHD is the only device in the forward detector, delivering information about the direction of particle tracks. By 1994 a tracker will be installed consisting of four planes of thin walled ($10^{-4}X_0$) straw chambers. This will give a considerable improvement of track reconstruction, which is desirable, e.g., with respect to missing mass calculations from forward detector tracks.

The material properties

The scintillator material used in the forward detector is Bicron's BC-404; some physical properties [4] of it are listed in table 2.1. In a mixture or compound, the rate of energy loss is approximately

$$\frac{\mathrm{d}E}{\mathrm{d}x} = \sum_{\mathrm{i}} f_{\mathrm{i}} \left(\frac{\mathrm{d}E}{\mathrm{d}x}\right)_{\mathrm{i}},$$

where f_{i} is the fraction by weight of the i-th element and $\left(\frac{\mathrm{d}E}{\mathrm{d}x}\right)_{\mathrm{i}}$ the mean rate of energy loss in this element. This has been used to determine an effective charge number and atomic weight of the scintillator medium needed for the Monte Carlo calculations. Table 2.2 gives some information about the material used for the light guides [33], and table 2.3 contains data for the EMI 9954 B photomultiplier [37] used for the forward hodoscope. This photomultiplier type is black plastic sleeved with a graphite coating connected to the cathode potential, to minimize dark current. A μ-metal shield is mounted on every device in order to minimize effects of stray magnetic fields on the multiplier performance.

Since the detector is exposed to light in the experiment area, all scintillators have to be wrapped so that they are absolutely light tight. The materials used for this are listed in table 2.4. Because of the limited space between the elements in a plane, the mechanically more stable, but thicker Cobex foil has only been used on the broad sides of the scintillators. The black mylar foil used on the edges is totally light tight already in one layer, but had to be protected from mechanical stress by another thin mylar foil. The aluminium strips on the edges were folded onto the broad sides and fixed there with some strips of transparent Tesa tape. The whole wrapping sits quite loosely on the scintillator because contact with the surface decreases the probability for total reflection. The total material on the broad scintillator surface corresponds to an equivalent of $\sim$ 680 μm mylar taking into account the radiation lengths of $\lambda_{\mathrm{mylar}} \sim 28.6$ cm and $\lambda_{\mathrm{Al}} \sim 8.9$ cm respectively.

2.4.2 The forward range hodoscope

After passing through the trigger hodoscope, the energy of the charged particles is measured in a four-layered plastic scintillator hodoscope, called Forward Range Hodoscope (FRH). Each plane has a thickness of 11 cm ($\hat{=}0.25X_0$) and consists of 24 triangle shaped scintillators - wedges like the last forward hodoscope plane (see figure 2.3), but thicker. The radii of these planes are 53, 59, 65 and 71 cm in the order as seen from the target. The forward range hodoscope stops protons up to $\sim$320 MeV kinetic energy, deuterons up to $\sim$400 MeV, ^{3}He up to $\sim$880 MeV,

base material	polyvinyltoluene (PVT)
density [g/cm^3]	1.032
H-atoms per cm^3	$5.21 \cdot 10^{22}$
C-atoms per cm^3	$4.74 \cdot 10^{22}$
electrons per cm^3	$3.37 \cdot 10^{23}$
H:C ratio (in volume)	1.1
hydrogen content [% in weight]	8.6
carbon content [% in weight]	91.4
effective charge number	5.612
effective atomic weight	11.157
radiation length [cm]	43.5
damping length [cm]	125
mean pulse width (FWHM) [ns]	2.2
rise time [ns]	0.7
decay constant (main component) [ns]	1.8
light output [% anthracene]	68
emission maximum [nm]	406
mean refractive index	1.58
softening point [°C]	75

Table 2.1: Properties of BC-404 plastic scintillator.

material	polymethylmetaacrylate (PMMA)
mean refractive index	1.49
density [g/cm^3]	1.18
damping length [cm]	600 (for 380 to 780 nm)

Table 2.2: Properties of the plexiglass used for the light guides.

and pions up to ~170 MeV. The energy resolution for 100 MeV protons is < 5 % (FWHM).

2.5 Data acquisition system

Figure 2.5 gives an overview of the data acquisition system [19]. At the present stage, the PROMICE/WASA experimental setup[3] consists of more than 320 active channels which are connected to charge sensitive ADC's, and 136 of them are also

[3]The final setup will hold about 1000 analogue and 4000 binary channels.

cathode material	RbCs
effective cathode diameter [mm]	46
quantum efficiency	26 % at 400 nm
sensitivity region [nm]	300 - 700
nominal cathode sensitivity [μA/lm]	110
no. of dynode stages	12 (linear focused)
dynode material	BeCu
nominal anode sensitivity [A/lm]	500
typical voltage (cathode-anode) [V]	1800
voltage at max. anode sensitivity (cathode-anode) [V]	2300
maximum voltage (cathode-anode) [V]	2800
maximum voltage (dynode-dynode) [V]	450
maximum cathode current [nA]	50
maximum anode current [μA]	200
nominal gain	$4.5 \cdot 10^6$
typical rise time [ns]	2
typical pulse width (FWHM) [ns]	3
typical transit time [ns]	41
typical time jitter (FWHM) [ns]	1.9
typical dark current at nominal sensitivity [nA]	2.4
maximum dark current at nominal sensitivity [nA]	20

Table 2.3: Characteristics of the EMI 9954 B photomultiplier.

broad side	edge
24 μm aluminium foil	12 μm aluminium foil
some strips of 165 μm Tesa tape for fixation	14 μm black mylar foil
250 μm Cobex foil	45 μm aluminized mylar foil for mechanical protection
185 μm black Scotch tape	

Table 2.4: Materials used for the light tight wrapping of the scintillators.

connected to TDC's. The central processing unit is based on VME, using a Motorola 68020 microprocessor as a core, running the VALET operating system. Via VME-based interfaces data is read from CAMAC and FASTBUS front-end equipment, CAMAC crate controller (CCC) and FASTBUS "smart" crate controller (FSCC),

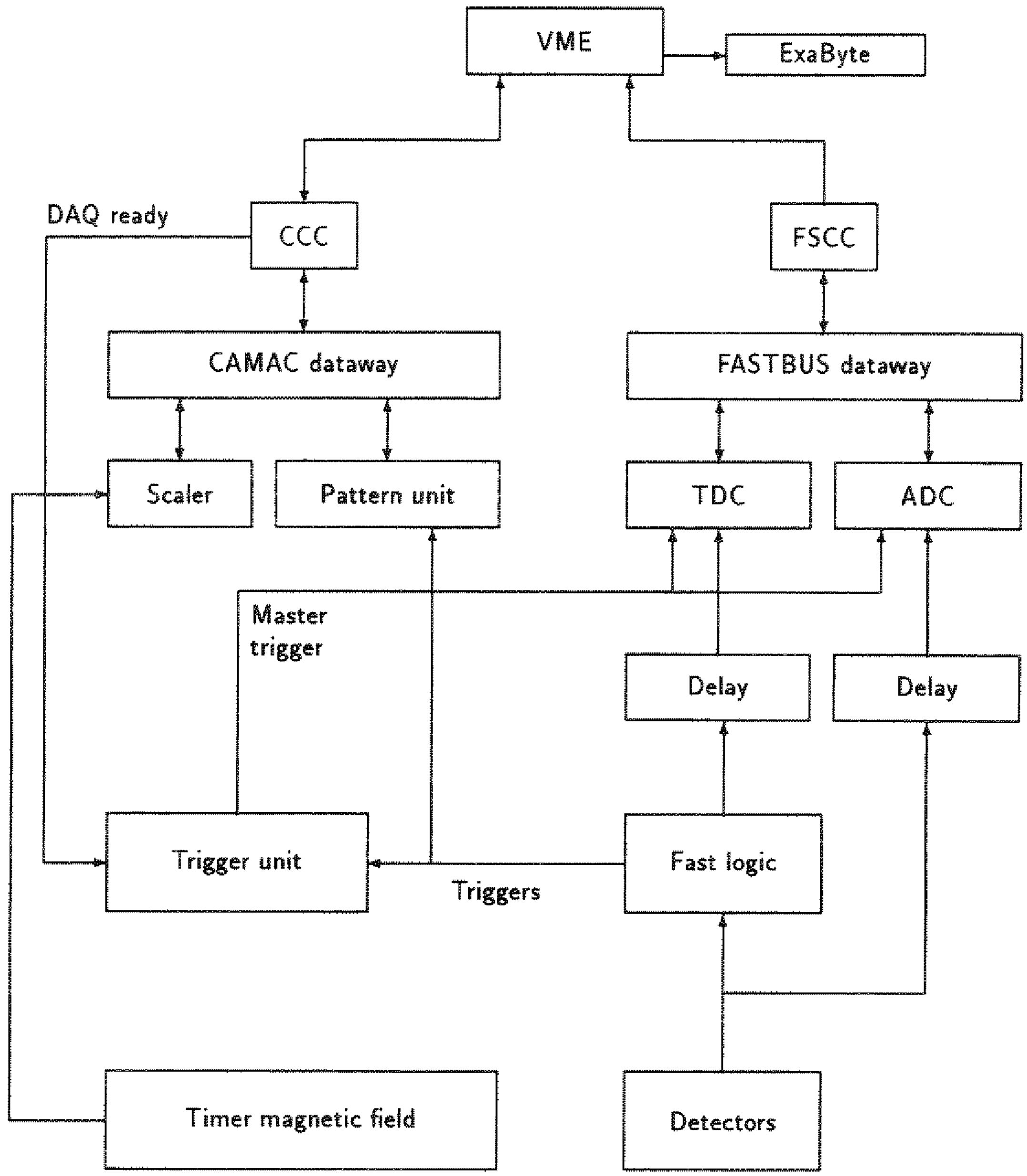

Figure 2.5: Schematic layout of the data acquisition system.

respectively. After on-line processing, selected data is sent through an SCSI interface to an ExaByte magnetic tape unit. This tape drive is able to store data at a maximum rate of about 200 events per second, having a fixed event length of 2460 bytes. Thus the total data rate written to tape was 492 kbytes per second, close to the maximum ExaByte speed of 500 kbytes per second. Pedestal subtraction was not yet implemented at that time. Not only ADC and TDC information, but also data from CAMAC scalers, pattern unit and magnetic field timer are written to tape.

The fast logic was implemented under CAMAC ECL logic. Leading edge discriminators (LeCroy 4413) were used. The next stage included logics for each detector such as OR's of elements, coincidences between subdetectors, multiplicity conditions, vetos etc. The results of these operations were then fed into programmable delays and fanouts as well as permanent coincidences and programmable logic matrices. The final signals were then used to control the data acquisition (master trigger), gate ADC's and TDC's, and have partially been given on scalers, TDC and pattern units.

The table 2.5 contains a list of triggers used for this work. Triggers T3*, T32 and T33 were used for the detection of ^{3}He in the forward detector.

Label	Description
T1	$\geq$ 1 hit in $>$ 1 plane of FHD
T2	$\geq$ 2 hits in $>$ 1 plane of FHD
T3	threshold on analog sum of signals from 1st FRH plane
T3*	T3 with higher threshold for ^{3}He identification
V3	$\geq$ 1 hit in the 3rd FRH plane (veto for quasi-elastic channels)
T4	$\geq$ 2 non-adjacent hit clusters in first FRH plane ($\Delta\varphi > 45°$)
T5	$\geq$ 1 hit in right **or** left CDE
V5	T5 used as veto for charged particles in the CD
T6	$\geq$ 1 hit in left **and** right CDE
T7	$\geq$ 1 hit in left **or** right CEC (central 7×5 elements)
T8	$\geq$ 1 hit in left **and** right CEC (central 7×5 elements)
T14	T8 $\times$ V5 ($\gamma\gamma$ coincidence)
T32	T1 $\times$ T3 $\times$ V3 $\times$ T2 (= 1 high energy FD track with short range)
T33	T32 $\times$ T7 $\times$ V5 (as T32 and one photon in the CD)
LP	light pulser trigger

Table 2.5: Some important triggers.

Chapter 3

Simulation of the detector performance

Detailed detector phenomena have been simulated using Monte Carlo methods. In this context, mainly the results of simulations concerning the reaction pd$\rightarrow^3$Heη around T_p=1250 MeV will be described, since they are essential for this work. The experiment was performed at two slightly different (2 %) beam energies, T_p=1250 and 1276 MeV. The simulation results concerning angular, momentum and missing mass resolution are in a good approach described by one Monte Carlo calculation. The threshold for this reaction is at T_p=891 MeV (P_p=1.57 GeV/c).

3.1 Kinematics

For the reaction pd$\rightarrow^3$Heη at a beam kinetic energy of 1250 MeV (1276 MeV), the excess energy, i.e. the energy above threshold in the center-of-momentum system (CMS), is 195 MeV (209 MeV). Since the ratio of the velocity β_{CMS} (the CMS velocity in the laboratory system) to the velocity $\beta^*_{^3\mathrm{He}}$ (the ^{3}He velocity in the CMS) is $g_{^3\mathrm{He}} = \frac{\beta}{\beta^*_{^3\mathrm{He}}} > 1$, there exists a maximum scattering angle for the ^{3}He nucleus. This so called "Jacobian" peak is at a laboratory scattering angle of 16.6° with respect to the beam axis, well within the acceptance of the forward detector covering a cone with 23° half opening angle. Figure 3.1 shows the kinematical relation between transversal and longitudinal momentum of the recoiling ^{3}He nucleus in the laboratory frame for some reaction channels at T_p=1250 MeV. In this picture, the area between the phase space limit[1] and the channel pd$\rightarrow^3$He$\pi^\circ\pi^\circ$ will be filled with background from multi-pion production because at this energy up to five pions can be produced per event (see figure 3.3 below). In the laboratory system, ^{3}He-momenta at the Jacobian peak around 1.48 GeV/c will show a peak. Of course, all the discrete momenta shown will be smeared out by the finite detector resolution.

[1]The maximum mass which can be produced in conjunction with a ^{3}He nucleus is 742 MeV/c^2 at this beam energy.

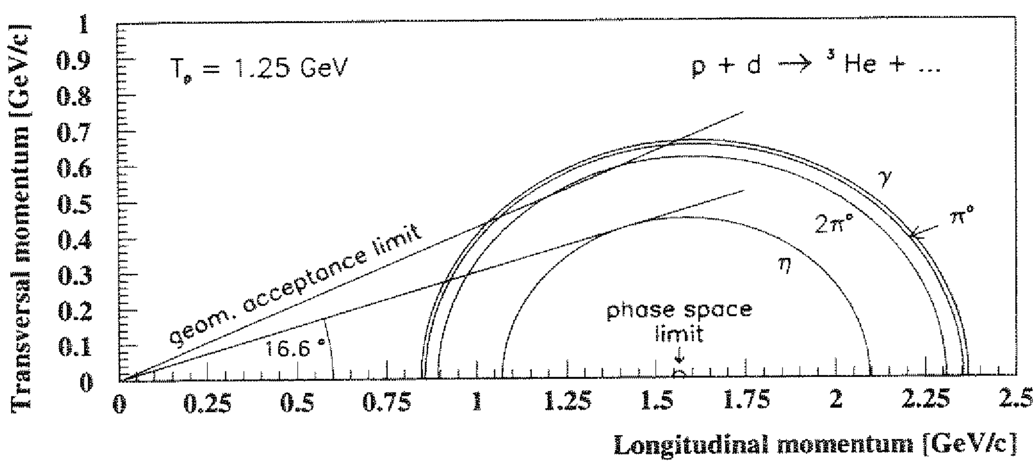

Figure 3.1: Transversal versus longitudinal momentum of the recoil ^{3}He nucleus for some reaction channels at $T_{\rm p}$=1250 MeV.

In figure 3.2 the angular distribution in the CMS for η mesons from the reaction d(p,^{3}He)η at $T_{\rm p}$=1450 MeV [26] is plotted, indicating quite strong forward peaking, i.e. the ^{3}He recoils are dominantly emitted backwards in the center-of-momentum system. The main angular dependence can be described by a phenomenological[2] fit [26] according to the function

$$\frac{\mathrm{d}\sigma}{\mathrm{d}\Omega_{\rm cm}}\left(\theta_\eta^{\rm cm}\right) = A_1 \mathrm{e}^{A_2\left(1+\cos\theta_\eta^{\rm cm}\right)}$$

with parameters

$$A_1 = 7.939 \pm 1.146 \quad \text{and} \quad A_2 = 0.8706 \pm 0.1238.$$

At a beam energy of $T_{\rm p}$=1250 MeV, far beyond the production threshold, up to five pions could theoretically be produced per event. The diagram 3.3 shows the kinematical relation between scattering angle and missing mass reconstructed from one track (^{3}He) in the forward detector for some discrete kinetic energies of the recoil nucleus. For the sake of clearness, some reaction channels involving multiple charged pion production as well as bremsstrahlung have not been included in this picture. The main difference between the single and the multi-meson production channels, i.e. between two-body and multi-body reactions, is that the latter cover a continuous region in this two-dimensional picture due to the variable internal energy in the subsystem, whereas the single-meson channels are vertical lines due to the

[2]Physically, it would be more instructive to perform a Legendre polynomial fit as is done in section 7.5.

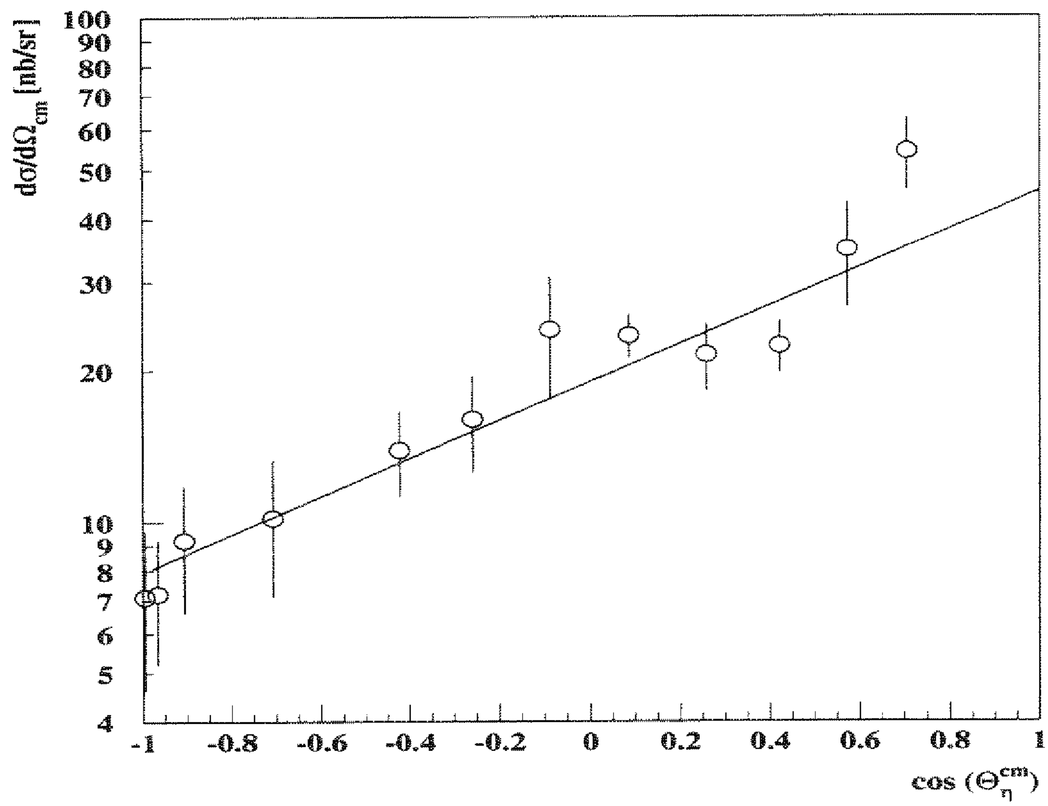

Figure 3.2: Angular distribution in the CMS for the reaction d(p,^{3}He)η from Saclay data at T_p=1450 MeV [26].

discrete missing mass calculated from one of two particles in the exit channel (to be folded with the detector resolution). Figure 3.4 is filled with Monte Carlo events for the reactions pd$\rightarrow$^{3}Heη and pd$\rightarrow$^{3}He$\pi^\circ\pi^\circ$ at T_p=1250 MeV corresponding to diagram 3.3. Isotropically distributed momentum vectors of the reaction products in the center-of-momentum frame were assumed. The two-body final state is clearly distinguished from the three-body channel by the constant missing mass calculated from the ^{3}He track. In the projection onto the abscissa, a relatively sharp (depending on the detector resolution) η missing mass peak is expected on a broad background from (dominantly) $2\pi^\circ$ events giving missing masses between 270 MeV/c^2 and 740 MeV/c^2 (phase space limit).

3.2 Detection efficiency

The geometric detection efficiency of the forward hodoscope is diminished by the space necessary for the light tight wrapping of the individual scintillator elements. This space between single elements in each layer is 400 μm. The length S of the

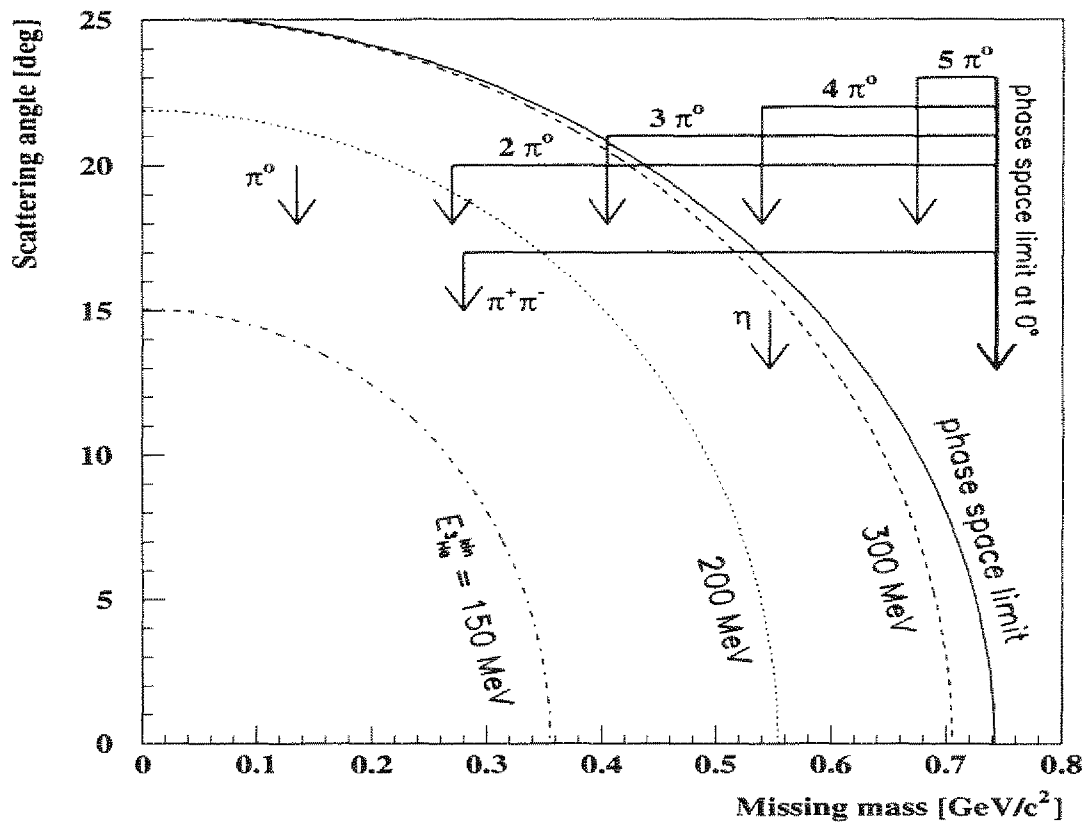

Figure 3.3: Kinematical limits for some reactions of the type pd→^{3}HeX at a beam energy of T_p=1250 MeV.

path along the edge of a spiraled scintillator is given by

$$\begin{aligned} S &= \int_{\varphi_1}^{\varphi_2} \frac{1}{k}\sqrt{1+\varphi^2}\,\mathrm{d}\varphi \\ &= \frac{1}{2k}\left[\varphi\sqrt{1+\varphi^2} + \ln(\varphi + \sqrt{1+\varphi^2})\right]_{\varphi_1}^{\varphi_2}, \end{aligned}$$

with the previously defined $k = \varphi_{max}/r_{max}, \varphi_{max} = 180°, r_{max} = 58$ cm. Thus the length of a bent element is 1086 mm measured from the hole for the beam pipe (42 mm radius) to the maximum radius. Since there are 24 elements in such a plane, the insensitive area is $24 \cdot 1086 \cdot 0.4$ mm^2 = 104.3 cm^2 which corresponds to 0.99 % of the active area in a twisted plane. In the straight plane, the "dead" area amounts to $48 \cdot 538 \cdot 0.4$ mm^2 = 103.3 cm^2, i.e. 0.98 % of the active area in the last plane. When demanding at least two planes hit by a track, the particle has to pass through the overlap area of the slits, which is of the order $\sim 23 \cdot 24 \cdot (0.4 \text{ mm})^2 = 88$ mm^2. Thus the total geometrical inefficiency due to the wrapping of the scintillators amounts to as little as $\sim 8 \cdot 10^{-3}$% which is negligible compared to other losses.

The hole for the beam pipe covers all scattering angles below 3° (laboratory system). This decreases the efficiency for the reaction pd→^{3}Heη at T_p = 1250 MeV

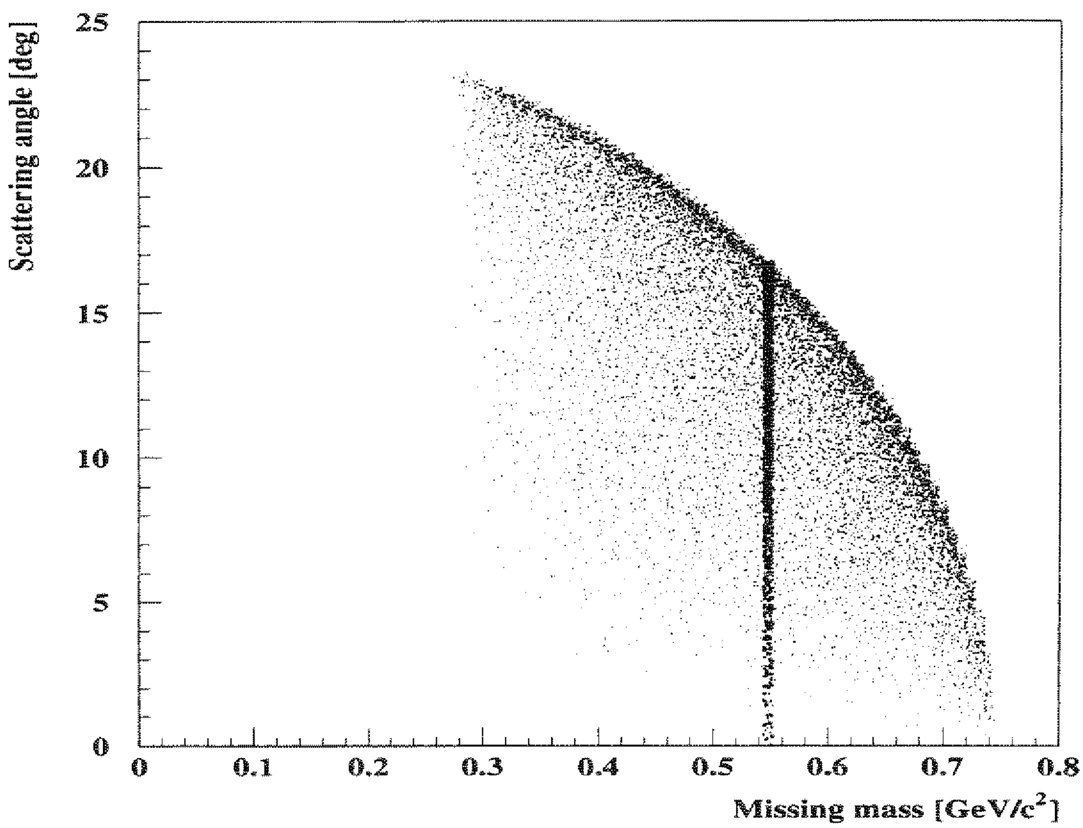

Figure 3.4: Scattering angle versus missing mass extracted from ^{3}He tracks in the forward detector for the reactions pd→^{3}Heη and pd→^{3}He$\pi^\circ\pi^\circ$ at T_p=1250 MeV (Monte Carlo).

by 0.1 % (see table 3.1) only, because the Jacobian is at 16.6° laboratory scattering angle.

Thus the total geometrical acceptance for this reaction is **99.9 %**. Table 3.1 gives information about the geometrical efficiency of the PROMICE/WASA detector for some reactions. The channel pd→^{3}He$\pi^\circ\pi^\circ$ is the dominating background after successful reconstruction of a ^{3}He track, since the main part of the cross section for single pion production with formation of a ^{3}He recoil nucleus is outside of the acceptance of the forward detector. ^{3}He can easily be selected by a hyperbola shaped cut in the d$E - E$ plot using the forward hodoscope as dE counter and the range hodoscope as total energy E counter. Since data acquisition systems are limited in accepting high counting rates (here dominating background from p-d quasi-elastic channels), an on-line threshold of 190 MeV for the energy deposition in a single element in the first range hodoscope plane was set.

Reaction at T_p = 1250 MeV	pd→^{3}Heη	pd→^{3}He$\pi^\circ\pi^\circ$	pd→pdη	pd→pd$\pi^\circ\pi^\circ$
=1 FD track	99.9 %	99.9 %	83.4 %	78.2 %
=2 FD tracks	$5 \cdot 10^{-3}$%	$1.3 \cdot 10^{-2}$%	0.69 %	1.8 %
=1 FD track and ≥1 CD tracks	17.7 %	19.6 %	17.9 %	28.2 %
=1 FD track and =1 CD track	17.3 %	18.3 %	16.6 %	25.5 %
=1 FD track and =2 CD tracks	0.46 %	1.3 %	1.4 %	2.7 %
190 MeV on-line threshold on 1st FRH plane	77.8 %	77.2 %	0.29 %	0.27 %

Table 3.1: Geometrical acceptance for some reactions under different conditions.

3.3 Resolution of the central detector

3.3.1 Shower size in the CsI crystals

The photons from η decays have energies ranging from 70 to 970 MeV with maximum probability at ~350 MeV. The electromagnetic showers they produce in the CsI crystals have been looked at. Figure 3.5 shows the number of CsI crystals hit in a 7 × 8 box of the central electromagnetic calorimeter when one photon from a decaying η (dashed line) of the reaction pd→^{3}Heη at T_p=1250 MeV is absorbed. The solid line shows the same for π° decay photons from the exit channel ^{3}He$\pi^\circ\pi^\circ$. An energy deposition threshold of 1 MeV per CsI element has been assumed. It turned out to be useful to demand a minimum number of crystals hit per impinging photon in order to obtain best possible separation between photons from π° decays and the ones from decaying η's [35]. Due to their lower energy, π° decay photons produce showers with less CsI crystals hit on average. Demanding at least 3 (4) crystals hit by every neutral track will decrease the efficiency for detection of one of the two η decay photons by 4.4 % (8.3 %), for a single π° decay photon by 21.1 % (40.2 %). Therefore, as an optimum solution, at least 3 hit elements were demanded when identifying an η decay photon.

3.3.2 Energy resolution for photons

The energy resolution in detection of these high energy photons is approximately 20 MeV (FWHM). For the relative energy resolution - as shown in figure 3.6 - one gets $\frac{\Delta E}{E} \sim \frac{(2.34\pm1.32)\%}{\sqrt{E[\mathrm{GeV}]}}$. Producing that picture for determination of the relative energy

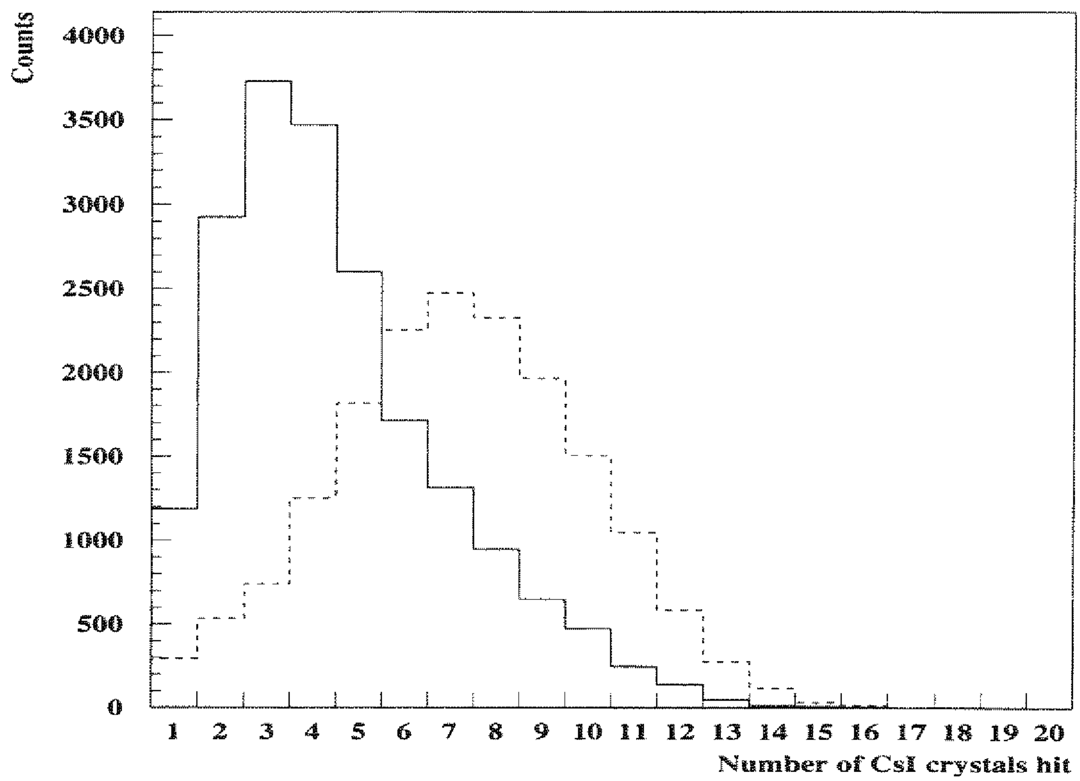

Figure 3.5: Number of CsI crystals hit in one central calorimeter box by absorption of one η decay photon (dashed line), respectively π° decay photon (solid line).

resolution is useful in this case, since we're dealing with a **range** of photon energies.

3.3.3 Angular resolution

The angular resolution in the central electromagnetic calorimeter is limited by the granularity of the CsI crystals (each element covering approximately 7.5° in the horizontal plane and 8.6° vertically). Figures 3.7 and 3.8 show the resolution in the polar and azimuthal angle, respectively. The angular resolutions obtained are 3.1° (FWHM) for the polar angle and 3.8° (FWHM) for the azimuthal angle in the laboratory system. This resolution is much better than expected from the granularity alone because of the significant shower development in the CsI from photons at these high energies (around $E_\gamma \sim 350$ MeV) as was shown in figure 3.5. Therefore the weighted sum over all CsI energy depositions regarded as belonging to the same photon gives a very good track reconstruction. This situation gets worse at lower photon energies where one has smaller electromagnetic showers. The fact that the histograms for the angular resolutions are not completely symmetric is due to the kinematics of the specific reaction which has been simulated here. The η decay photons of the reaction d(p,^{3}He)η at T_p=1250 MeV do not illuminate the front of

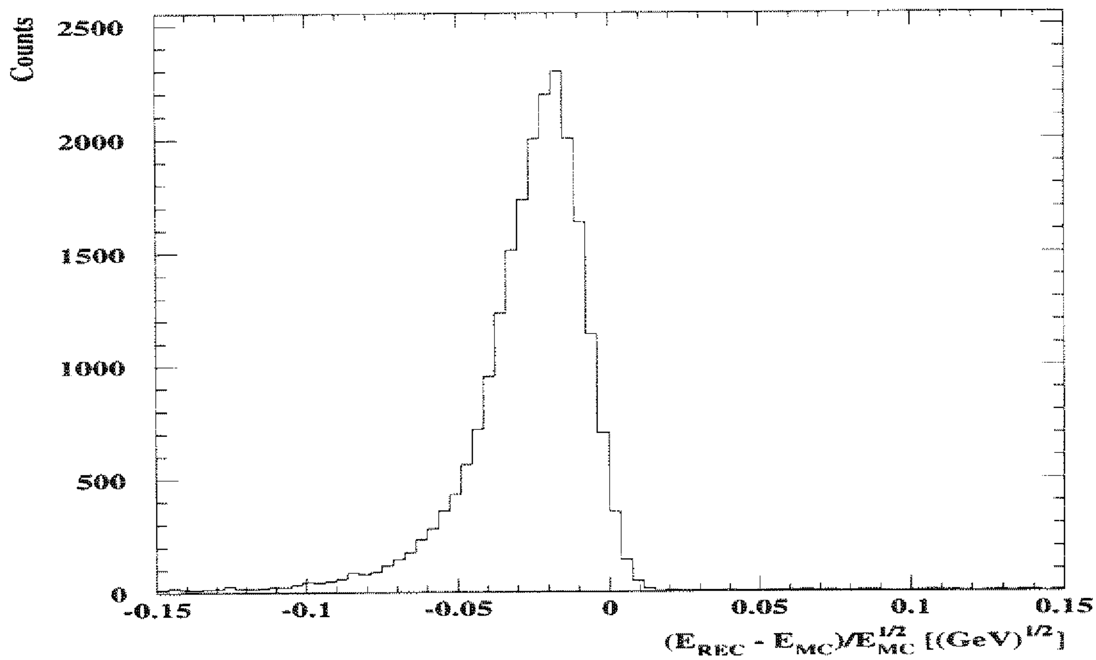

Figure 3.6: Relative energy resolution for reconstructed η decay photons in the CsI.

the CsI box homogeneously. The center-of-gravity of the angular distribution lies at the edge between two crystals thus leading to a preference of a certain - in this case larger - scattering angle. However this illustration has been shown because it provides a more realistic picture of the resolution which can be expected in this specific reaction. The same features will be seen in the simulation of the response of the forward detector to this reaction channel.

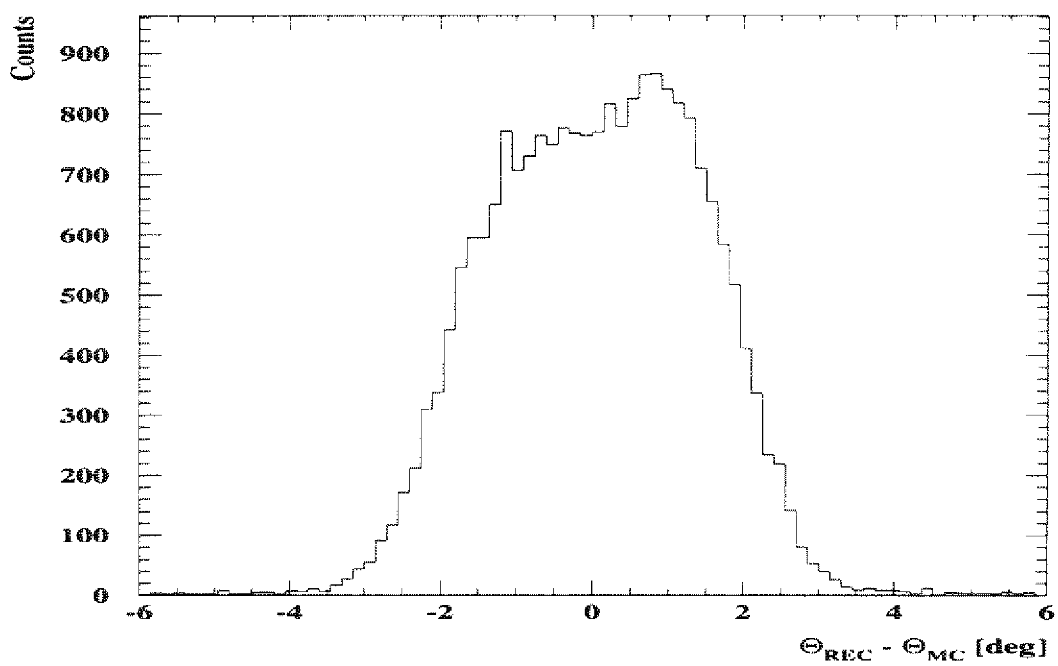

Figure 3.7: Polar angle resolution in the central electromagnetic calorimeter.

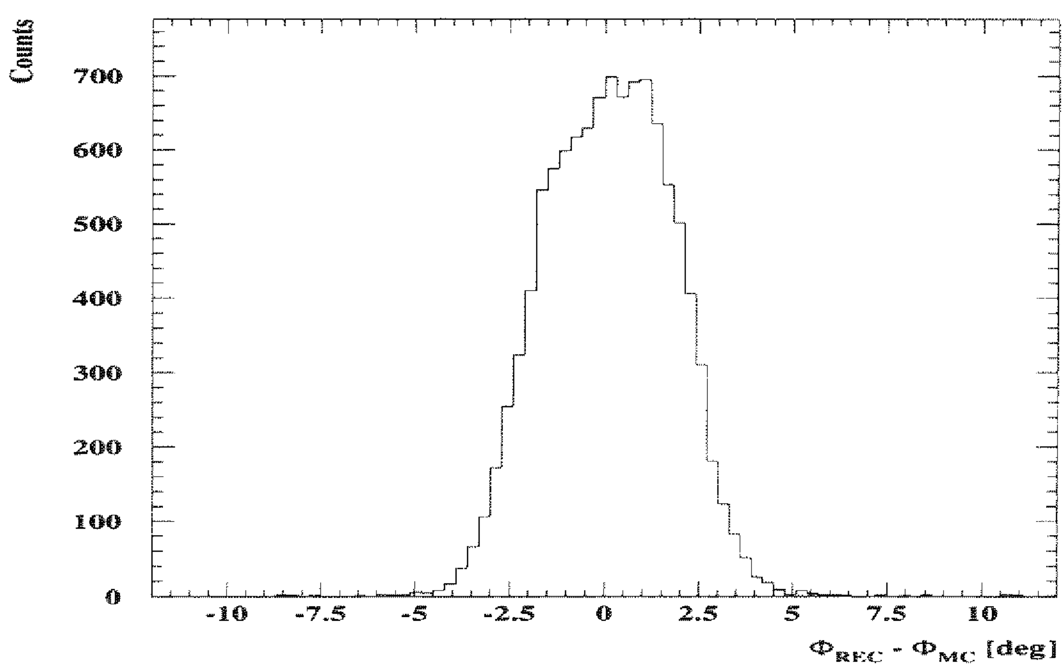

Figure 3.8: Azimuthal angle resolution in the central electromagnetic calorimeter.

3.4 Performance of the forward detector

The PROMICE detector is not designed to perform time-of-flight measurements; the distance between target and forward detector is 110 cm. The idea is that dE − E measurements using the forward hodoscope as dE detector and the range hodoscope as total energy absorber[3] are sufficient for particle separation - at least to separate ^{3}He from single charged particles. Knowledge of the direction and the absolute value of the momentum of the ^{3}He track, i.e. three parameters, will then allow for a missing mass analysis which shall show a clear η signal on the continuous multi-pion background.

3.4.1 The angular resolution

The polar angular resolution in reconstructing forward detector tracks is given by the trigger hodoscope (FHD) only because there exists no other device which can provide such information at this time. Later in 1994, a tracker in front of the hodoscope will improve the situation. Figure 3.9 shows the polar angle resolution

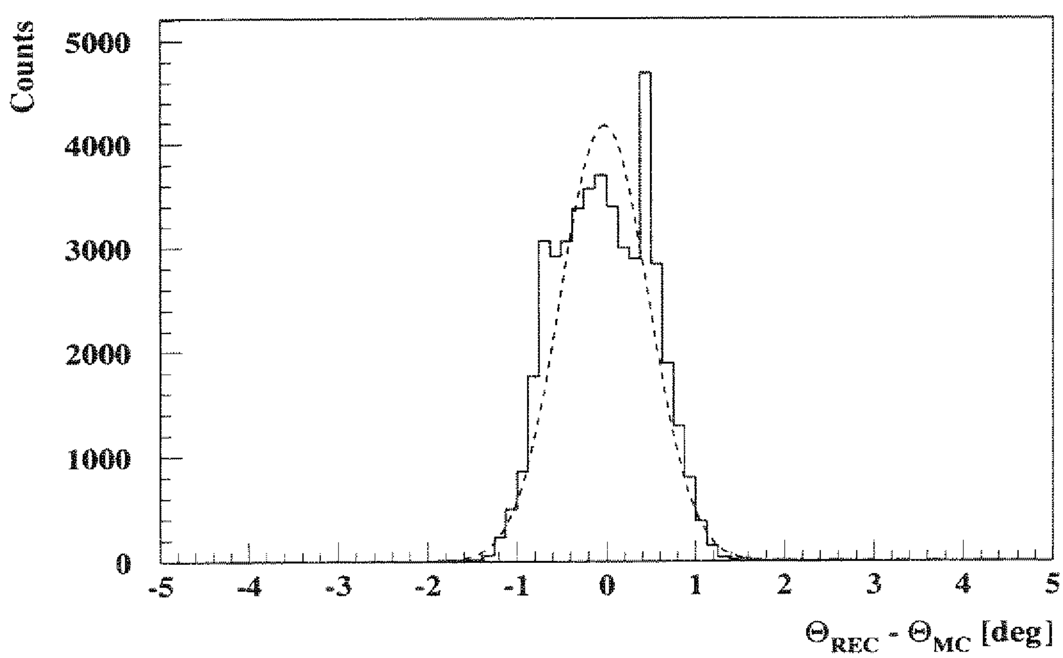

Figure 3.9: Polar angle resolution in the forward detector (solid histogram: Monte Carlo results, dashed line: gaussian fit).

[3]A more advanced method is to compare the energy depositions in all seven FD planes to the ones expected from Monte Carlo for different particle types, calculate a χ^2 for each particle type, and assign the type with lowest χ^2 to the particle track (see section 7.2.2).

obtained by reconstruction of the recoil nucleus from the reaction channel d(p,^{3}He)η at T_p=1250 MeV. At a glance one notices the two sharp peaks on this basically gaussian distribution. The reason for this is - analogous to the results obtained for the central detector - that the Jacobian of the ^{3}He scattering angle distribution ($\sim$ 16.6° laboratory angle to the beam axis) is lying between two radii (defined by the center-of-gravity of the respective pixels) in the forward hodoscope. In figure

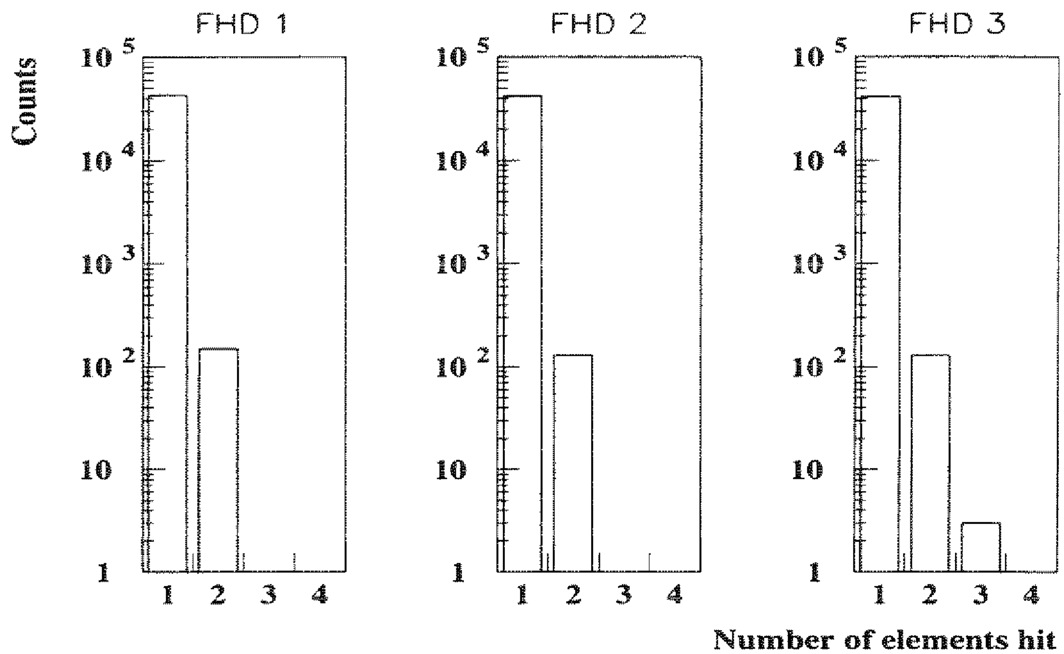

Figure 3.10: Expected hit multiplicity in the FHD planes from one ^{3}He track.

3.10, the number of elements hit in each FHD plane is shown for Monte Carlo events with one ^{3}He track. Obviously the particle tracks very seldomly hit two elements at a time (inclined tracks hitting two elements at their respective edges or nuclear interactions), and there exists no significant shower development when a charged particle passes through the thin scintillator material. Thus the scattering angle of the reconstructed track is determined by one pixel mainly, where the center-of-gravity of the pixel has been taken as push-through point. Having the Jacobian lying between two pixel radii will therefore give either a too large or too small scattering angle in most cases[4]. The basic gaussian distribution, indicated by the dotted line in figure 3.9, comes from the more equally distributed smaller scattering angles. The mean resolution of the scattering angle in the laboratory system relative to the beam axis is 1.2° (FWHM).

The azimuthal angular resolution can be seen from figure 3.11. The full width

[4]One possibility to improve the resolution is to use the time information from all three scintillators connected to the pixel in question (see section 7.4).

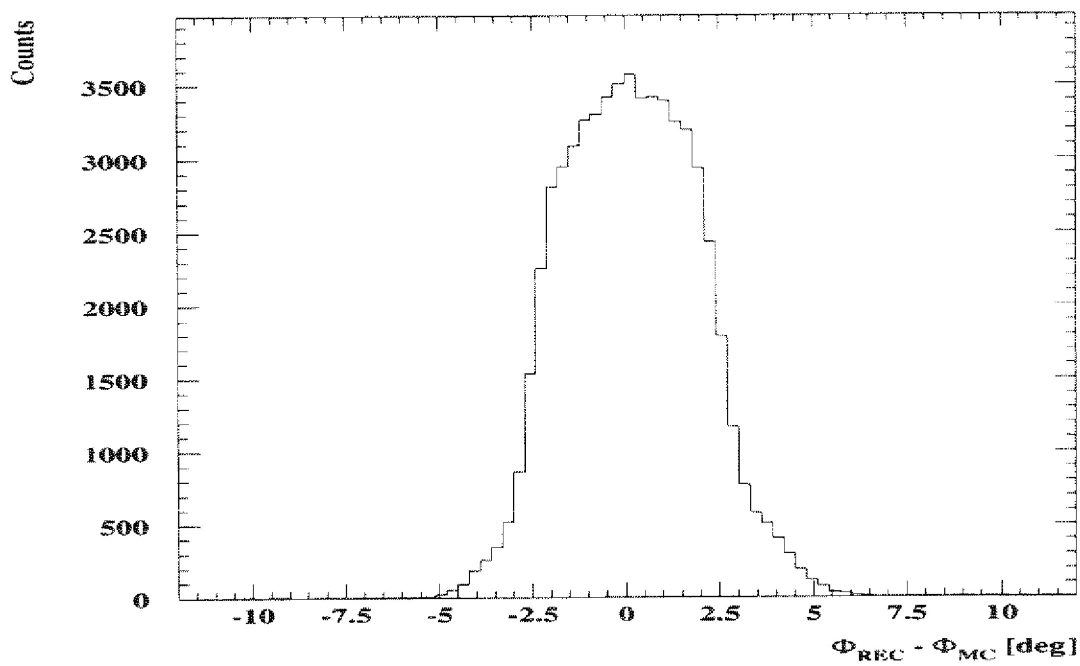

Figure 3.11: Azimuthal angular resolution in the forward detector.

at half maximum of the reconstructed azimuthal angle is found to be 4.1°, slightly larger than the half angular width of a pixel (3.75°).

3.4.2 Energy measurement in the forward detector

Mean energy loss by ionization

When passing through matter, a charged particle loses its energy primarily by ionization. In the early 1930s Bethe and Bloch treated the problem of this energy loss in the framework of quantum mechanics using first-order perturbation theory. For a moderately relativistic particle with charge ze they found the following well known expression for the mean energy loss $\mathrm{d}E$ in a layer $\mathrm{d}x$ of the medium

$$\frac{\mathrm{d}E}{\mathrm{d}x} = 4\pi N_A r_e^2 m_e c^2 z^2 \frac{Z}{A}\frac{1}{\beta^2}\left[\ln\frac{2m_e c^2\gamma^2\beta^2}{I} - \beta^2 - \frac{\delta}{2}\right],$$

where Z is the atomic number and A the atomic weight of the elements in the medium. As usual, m_e denotes the electron mass and r_e the classical radius of the electron, and the product $4\pi N_A r_e^2 m_e c^2$ is equal to 0.3071 MeV g^{-1} cm^2. The mean ionization potential I is approximately given by $16Z^{0.9}$ eV for $Z > 1$. Disregarding density effects (see chapter 5), integration of this formula leads to the average energy loss curves shown in figures 3.12 and 3.13 for a 5 mm thick forward hodoscope plane and an 11 cm thick range hodoscope plane, respectively. Thus the energy loss of a

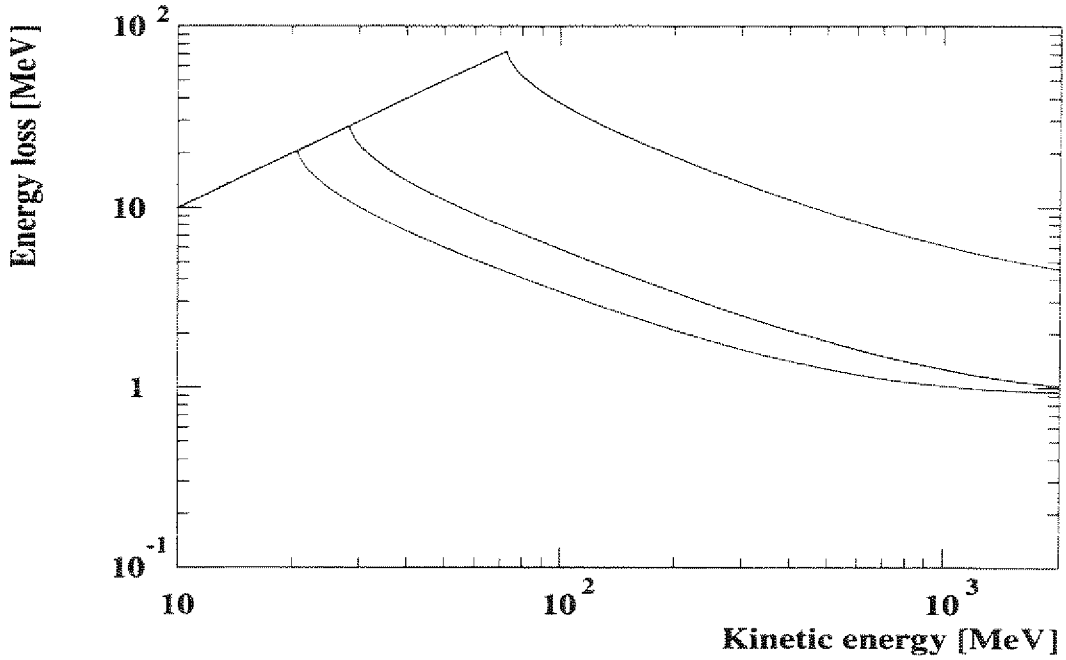

Figure 3.12: Mean ionization loss for protons, deuterons and ^{3}He (bottom to top) in 5 mm plastic scintillator (forward trigger hodoscope).

minimum ionizing proton in a forward hodoscope plane is expected to be 1 MeV, and in a range hodoscope plane 20 MeV. ^{3}He particles of 350 MeV kinetic energy lose approximately 11 MeV per FHD plane, and after passing through the forward hodoscope they are stopped in the first range hodoscope plane since 11 cm plastic scintillator stops ^{3}He particles up to a kinetic energy of 400 MeV.

Energy resolution

Since no time-of-flight information is available in order to separate forward from backward scattered ^{3}He particles in the center-of-momentum frame, the energy deposition in the forward detector is essentially necessary for the determination of the ^{3}He CMS momentum vector. In figure 3.14 the difference between the total measured energy in the forward detector and the original kinetic energy at the vertex given by the Monte Carlo event generator is plotted, thus showing the energy resolution for ^{3}He recoils from the reaction d(p,^{3}He)η at T_p=1250 MeV. These nuclei have kinetic energies ranging from 200 to 700 MeV in the laboratory system at scattering angles up to 16.6°. The width of this distribution is 14.5 MeV (FWHM). The mean value is shifted by 30 MeV, indicating a relatively high amount of unmeasured kinetic energy of the order 10 %. Some inevitable "dead" material such as the scattering chamber window and wrapping of the scintillators is responsible for this loss.

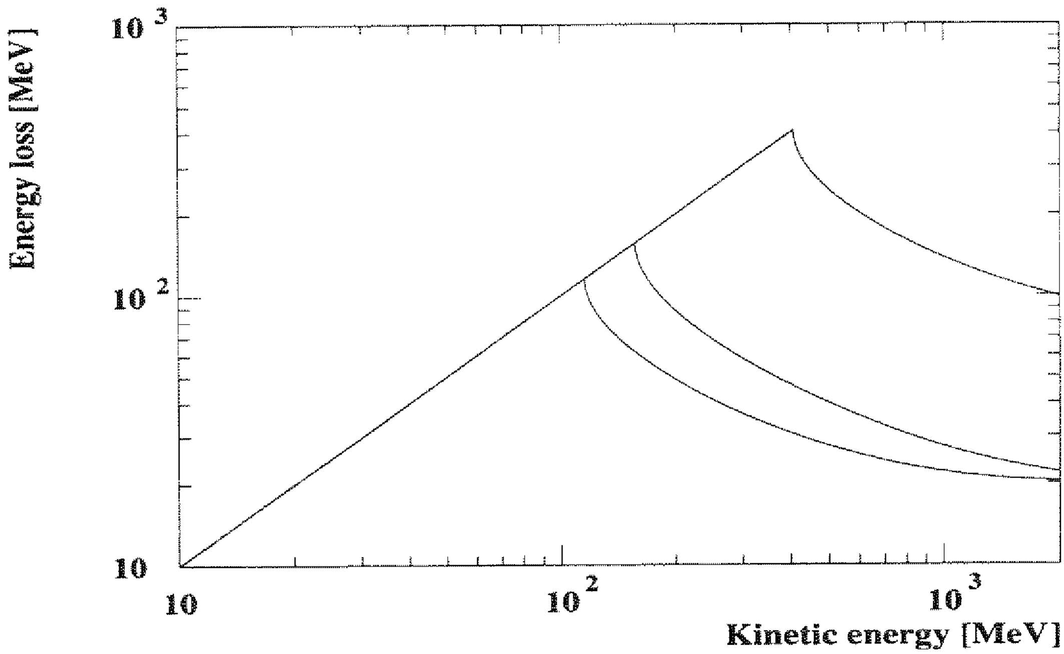

Figure 3.13: Mean ionization loss for protons, deuterons and ^{3}He (bottom to top) in 11 cm plastic scintillator (forward range hodoscope).

Correction for insensitive material

When using the measured energy deposition to reconstruct the kinetic energy of a particle, one has to correct for these losses in the offline analysis. The amount of unreconstructed energy of course depends on the kinetic energy of the traversing particle and on its scattering angle, since the path length within the materials changes. However, the angular dependence was found to be very weak, on the contrary to the energy dependence. Figure 3.15 shows the quotient of Monte Carlo and measured energy in the forward detector versus reconstructed energy (E_{FD}) and scattering angle (θ_{REC}). Thus in the data analysis, for each scattering angle and measured energy deposition, the energy has been multiplied by the corresponding function value given by the diagram.

3.4.3 Missing mass resolution

When extracting the (missing) mass of the η meson in the reaction pd$\rightarrow$^{3}Heη from one measured track (^{3}He) in the forward detector (see figure 3.16), the resolution is expected to be limited to ~80 MeV/c^2 (FWHM)[5] due to the large pixel size. Using a bin size in the graphical representation which is only half that large

[5]The resolution obtained using information from the tracker will be < 20 MeV/c^2 (FWHM).

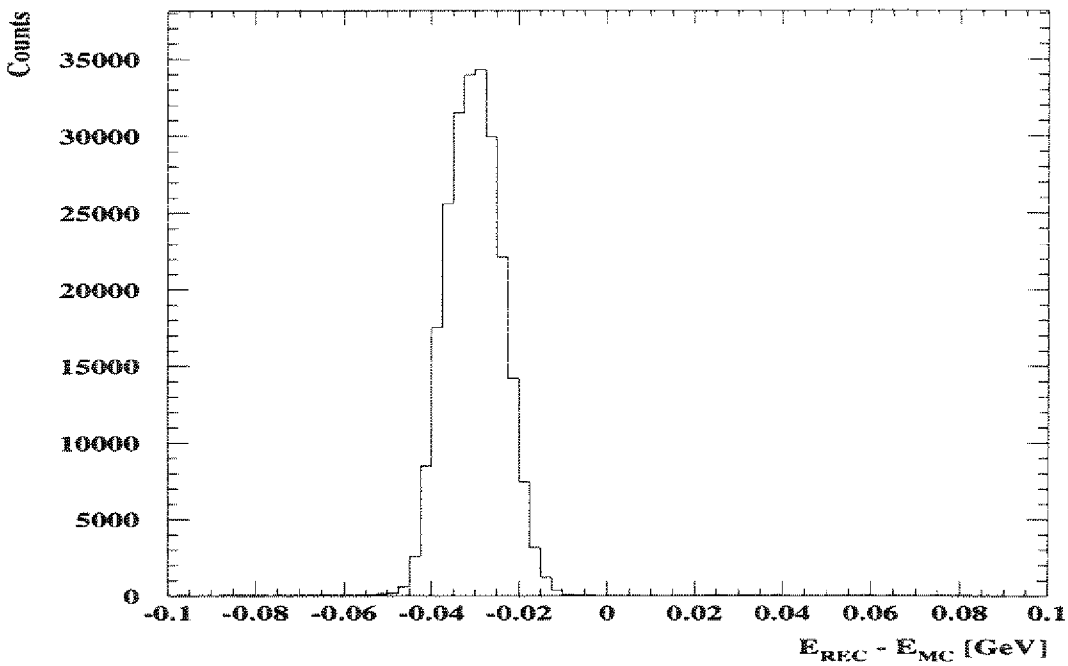

Figure 3.14: Total energy resolution in the forward detector.

(dashed line), again a strong double peak structure is visible similar to the polar angular distribution in figure 3.9. This indicates that the larger bin size (solid line) is probably more appropriate to the problem. But on the other hand, here one sees indirectly that the gradient of the missing mass formula with respect to the measured scattering angle is by far larger than the one with respect to the deposited energy, since one discrete scattering angle directly corresponds to a certain, discrete missing mass value. For this reason, the performance of the forward detector will in the future be improved by a better determination of the track **direction** instead of an increased resolution in measuring the track **energy**.

The background in a measurement of the η missing mass by detection of the ^{3}He recoil nucleus is dominated by multi pion production. In figures 3.17 and 3.18 the missing mass distributions expected from double and triple pion production are shown. Due to the detector resolution missing mass values below the kinematical limit are found.

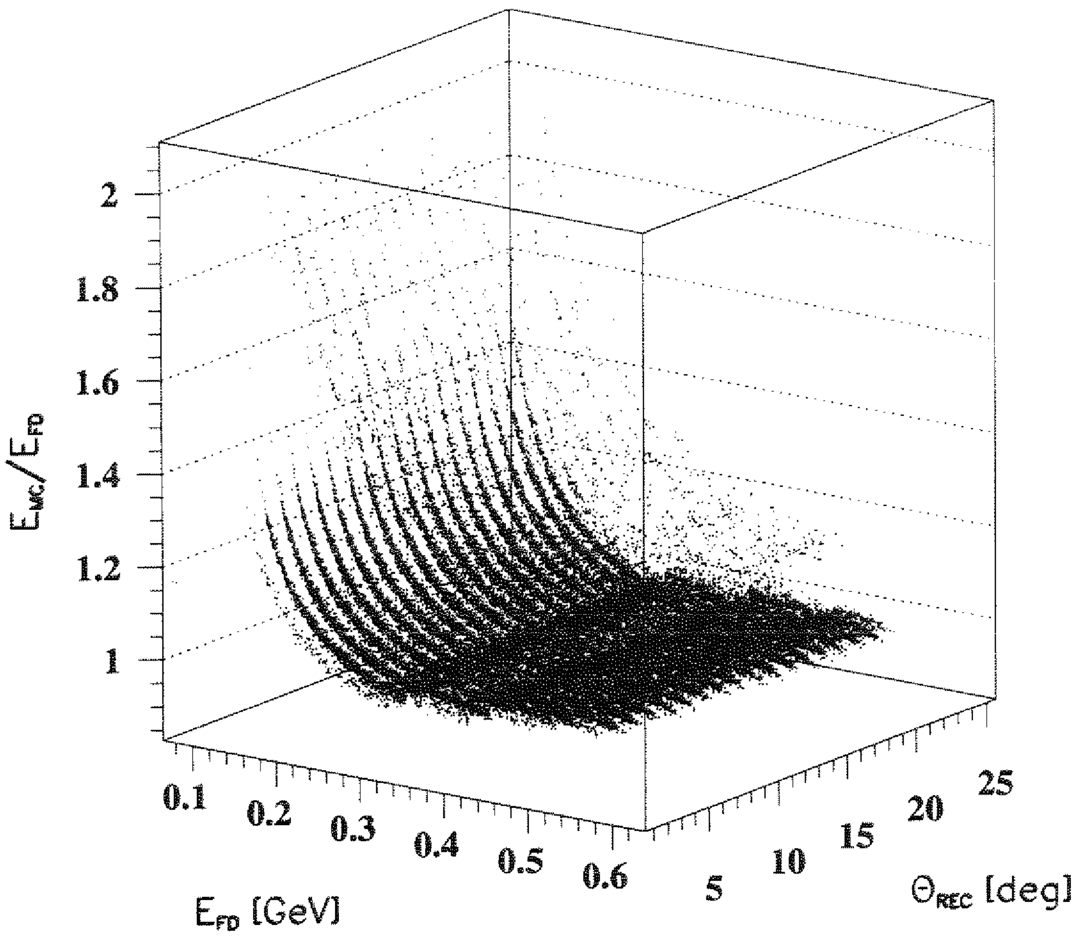

Figure 3.15: Quotient of Monte Carlo and measured energy in the forward detector versus reconstructed energy and scattering angle.

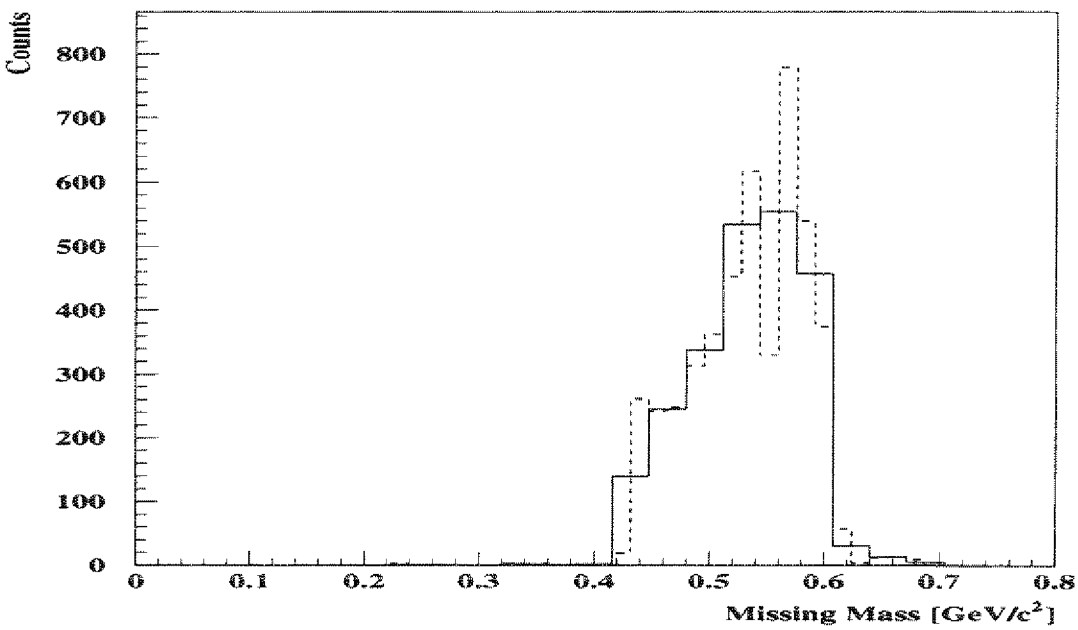

Figure 3.16: Monte Carlo missing mass distribution of the reaction pd$\rightarrow$^{3}Heη using the present experimental setup (dashed line: half of the bin size in the solid histogram).

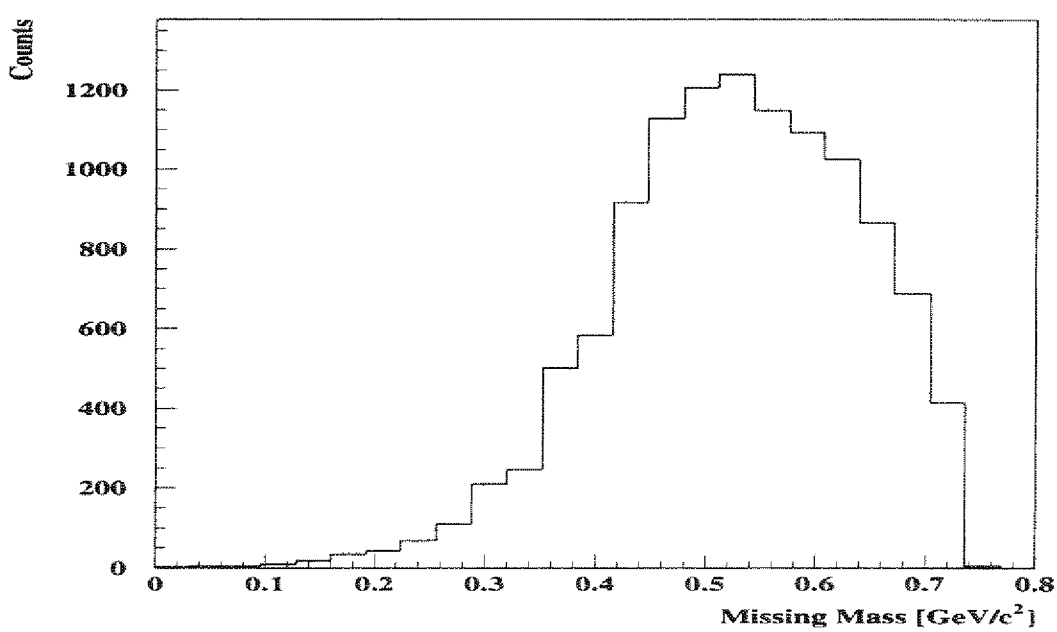

Figure 3.17: Missing mass distribution extracted from simulated ^{3}He tracks of the reaction pd$\rightarrow$^{3}He$\pi^\circ\pi^\circ$.

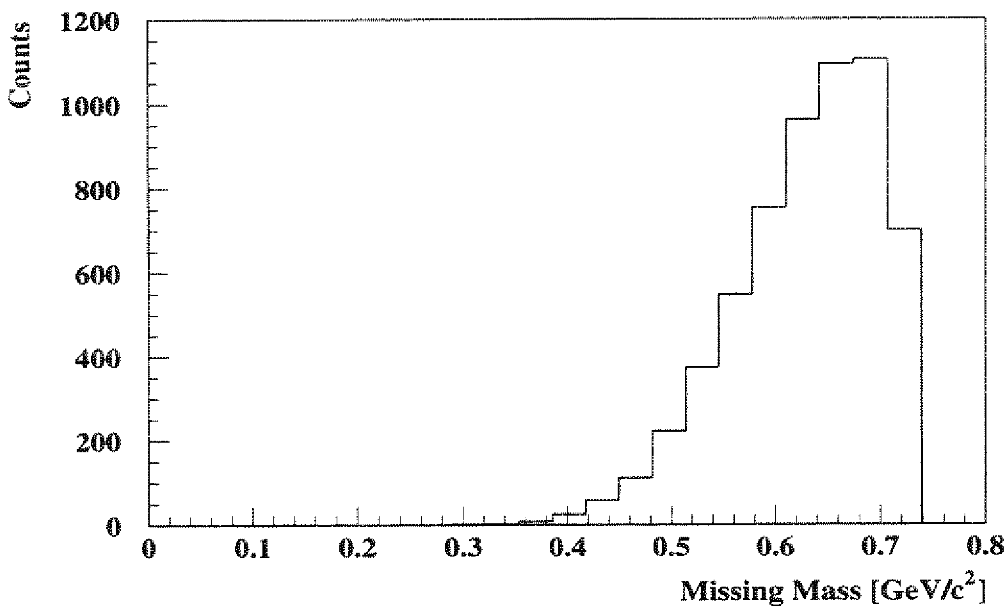

Figure 3.18: Missing mass distribution extracted from simulated ^{3}He tracks of the reaction pd$\rightarrow$^{3}He$\pi^\circ\pi^\circ\pi^\circ$.

3.5 Nuclear interactions in the forward detector

The energy deposition measured in a detector plane may deviate from the expected loss by means of, e.g., break-up or nuclear reactions. Such reactions will lead to a different response of the detector to the impinging particle since it "changes" its nature during the passage through the absorber material which might affect the energy deposition in the respective plane and lead to additional sampling fluctuations.

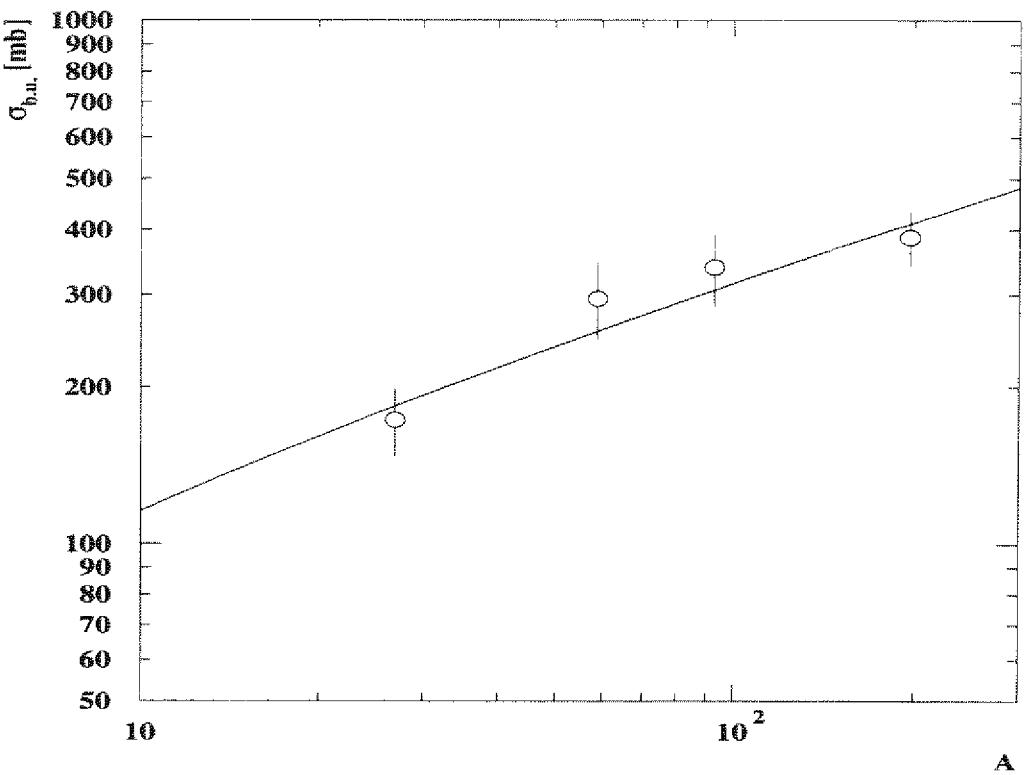

Figure 3.19: Total ^{3}He breakup cross section for some target nuclei.

The ^{3}He particles entering the forward detector might break up during their passage through the scintillator medium due to nuclear interactions. A. Djaloeis et al. [11] have measured the total breakup cross section for the reactions ^{27}Al, ^{59}Co, ^{93}Nb, ^{197}Au(^{3}He,d)X at $T_{^3\mathrm{He}}$=130 MeV (see figure 3.19). The fit function shown here is defined as

$$\sigma_{\mathrm{b.u.}}[\mathrm{mb}] = (80.4 \pm 18.1)A^{1/3} - (57.5 \pm 71.6),$$

with a χ^2 of 0.7. Thus for the average scintillator medium (A=11.157) one gets a total breakup cross section of $\sigma_{\mathrm{b.u.}}$=122 mb at $T_{^3\mathrm{He}}$=130 MeV. With approximately $9.95 \cdot 10^{22}$ atoms per cm^{-3} one obtains a probability for ^{3}He breakup of

$$P_{\mathrm{b.u.}} = 1.22\% \text{ per cm path length within the scintillator medium.}$$

This amounts to ~0.6 % per forward hodoscope plane and ~13.4 % per range hodoscope plane. On average, this might lead to a higher hit multiplicity in the following planes and a lower energy deposition in the respective plane where the breakup occurs. This has to be taken into account as an additional systematic uncertainty when defining cuts on, e.g., the energy deposition in a forward detector plane, or when calculating the detection efficiency.

Chapter 4

Calibration of the forward detector

The calibration procedure for the forward detector is aimed at getting energy dependent calibration constants for each individual detector element and radial position of the ionizing particle's impact point. The calibration has been performed on data samples containing proton-proton elastic scattering at beam energies of 75-100, 282, 500 and 1265 MeV by superposition of the corresponding Monte Carlo distributions.

4.1 Method

Monte Carlo samples for p-p elastic scattering at the different energies have been prepared. For that, events were generated using the S/R GENEV (*FOWL*) event generator which is provided in the *CERN* library. The isotropic phase space distribution in the center-of-momentum system was modified by a phenomenological parametrization of the form

$$\frac{d\sigma}{dt} \sim \exp(A_1 t + A_2 t^2),$$

where t is the four-momentum transfer. This exponential form lacks any fundamental theoretical significance, but is a convenient way to describe the results of Ryan et al. [34] on proton-proton differential cross sections. From these measurements the values for A_1 and A_2 were obtained by interpolation, and are shown in table 4.1.

The (weighted) events produced by the event generator were used as input for a GEANT Monte Carlo study, including the forward range hodoscope, the forward trigger hodoscope, wrapping of the scintillators, beam pipe, scattering chamber, window and bars as well as flanges, i.e. the complete PROMICE setup as shown in figure 2.1. For the calculation of energy losses and multiple scattering in the quasi-continuous physical processes, the following setting of GEANT parameters was used:

Beam energy [MeV]	Beam momentum [MeV/c]	A_1	A_2
75-100	383-445	-0.250	3.900
282	780	-0.821	3.456
500	1090	-1.268	1.110
1265	1994	-8.000	6.954

Table 4.1: Parameters for the proton-proton elastic cross section.

- Decay in flight with generation of secondaries
- Multiple scattering according to Molière theory
- No photo-fission
- Muon-nucleus interactions with generation of secondaries
- Continuous energy loss without generation of δ-rays and full Landau-Vavilov-Gauss fluctuations
- Photo-electric effect with generation of the electron
- Compton scattering with generation of e^-
- Pair production with generation of e^+/e^-
- Bremsstrahlung with generation of γ
- No Rayleigh effect[1]
- Positron annihilation with generation of γ's
- Hadronic interactions with generation of secondaries

The energy depositions in the individual sensitive detector elements found by GEANT were written to a file similar to real data from the experiment. Then the offline software was run on that MC sample. On input, all energy depositions have been smeared out according to a normal (gaussian) distribution because of the limited photoelectron statistics at the photomultiplier output. The number of photoelectrons per MeV energy deposition can be estimated as follows. The photon yield in the amplitude range of photomultiplier tubes is of the order ≈ 1 photon per 100 eV energy deposition in plastic scintillators [29]. The efficiency is decreased by the geometrical light collection efficiency which of course strongly depends on

[1]scattering of photons by atoms as a whole, i.e. electrons in the atom participate as a whole $\rightarrow$ "coherent" scattering

the shape of the scintillators; 10 % is a good estimate for this efficiency factor. The attenuation length of BC-404 is 125 cm, thus leading to an efficiency factor of, e.g., 70 % for 50 cm path length in the scintillator. The light collection efficiency in the light guide might be of the order 60 %. The quantum efficiency of the photomultiplier cathode is (depending on the specific type) of the order 25 %, and the focusing efficiency within the photomultiplier as 25 % (data from Philips). Thus the total number of photoelectrons per MeV energy deposition is estimated to be about 25. But this value strongly depends on the geometrical shape of the scintillators[2] and on the amount of deposited energy (quenching). Therefore, **only** comparison to measured p-p elastic scattering data can give the correct values. 35 photoelectrons per MeV energy deposition for the bent scintillators and 100 photoelectrons per MeV for the straight forward trigger scintillators were found to give satisfactory agreement (see figure 4.1) with the width of the measured energy distributions (30 photoelectrons per MeV for the range hodoscope scintillators).

The smearing was done by the transformation

$$EDEP \to EDEP \cdot \left(1 + \frac{GR}{\sqrt{NPEGEV \cdot EDEP}}\right),$$

where $EDEP$ is the energy deposition in GeV, $NPEGEV$ the number of photoelectrons per GeV, and GR is a gaussian distributed pseudo random variable with zero mean and unit variance ($\frac{1}{\sqrt{NPEGEV \cdot EDEP}}$ is the RMS value of the photoelectron statistics distribution). A normalization is not necessary because the distribution for GR is normalized to unit integral, and only the correct width of the energy distribution is needed.

The distributions of the deposited energies for each radial bin in every detector element have been extracted. These distributions were put on a "card" in the offline job for later comparison to real data.

After that, the offline job was run on real p-p data. In order to make the selected p-p elastic sample as clean as possible, the following conditions have been applied (compare the listing of hardware triggers in table 2.5):

- Skip hardware triggers T4 (coplanar tracks in forward detector), T6 (central detector "charged" coincidence) and T8 (CsI coincidence)
- Select software triggers 1 (single track in single forward detector, namely FHD tracks in non-overlap zone), 2 (forward detector FRH-FHD coincidence) and 7 (forward detector track in coincidence with charged central detector track)
- Skip light pulser events
- Demand one and only one charged forward detector track

[2]Photons which are emitted in a direction perpendicular to the straight connection with the photomultiplier tube will be focused onto the multiplier due to the shape of these scintillators. That is a great advantage compared to scintillators with parallel surfaces.

- Set software threshold slightly above the individual pedestal
- Demand total energy deposition in the forward detector to be greater than $EKMIN$, deposition in the last FHD plane to be greater than $DELOJ3$ and less than $DEUPJ3$, total energy deposition in the forward trigger hodoscope to be greater than $DELOJH$ and less than $DEUPJH$, and deposition in the first range hodoscope plane to be greater than $DELOR1$ and less than $DEUPR1$. The values for these limits at the different beam energies are listed in table 4.2.

Beam energy [MeV]	75 - 100	282	500	1265
$EKMIN$ [MeV]	5	140	105	70
$DELOJ3$ [MeV]	3	1	0.5	0.3
$DEUPJ3$ [MeV]	20	4.1	3.2	2.7
$DELOJH$ [MeV]	8.0	2.8	1.0	0.85
$DEUPJH$ [MeV]	50	13	10	8.5
$DELOR1$ [MeV]	0	36	22	14
$DEUPR1$ [MeV]	100	70	55	40

Table 4.2: Limits for energy depositions used when selecting elastic p-p events.

- Demand FHD-FRH coincidence if polar angle of the track lies in geometrical overlap zone
- Demand at least one FHD spiral plane hit (otherwise scattering angle is not defined)
- Demand one and only one hit in each plane
- Demand TDC info for all hits

In order to obtain sufficient statistics, the radial dependence has been limited to 10 bins which seems to be precise enough for interpolation, i.e. the possible hit radii in the forward hodoscope between 4.2 and 58 cm have been grouped to ten bins. Radial bin no. 3 was chosen as a reference which corresponds to a hit radius between 14 and 19 cm for the range hodoscope, and 15 respectively 20 cm for the forward trigger hodoscope.

In the first run on real data, no ADC to energy conversion and no correction for radial nonuniformity of the output signal was done. Superposition of the Monte Carlo distributions on the real data at one radial bin gives a (1st order) calibration constant for each element. The values for other radii may differ from these due to the nonuniformity of light output and to energy dependent response which is not considered in the Monte Carlo calculation. In order to compensate for the first, nonuniformity constants have to be extracted which are the inverse of the ratio of the calibration constant at another radius and at the reference radius. These numbers are obtained as follows:

A second run on the real data is done **with** ADC to energy conversion. Data at high energy (1265 MeV) have been used for this because of minimum radial energy dependence. The nonuniformity constants are then extracted from the ADC and Monte Carlo distributions. The reference radial bin is given light output efficiency 1, and all ADC calibration constants are rescaled. For better control of the superposition, the ADC distributions with Monte Carlo curves superposed are plotted on output. An example of this can be seen in figure 4.1 which shows Monte Carlo distributions superposed on measured p-p elastic scattering data at T_{p}=1265 MeV for the 10 radial bins of the third (straight) forward hodoscope plane. The agreement is very good, i.e. the photoelectron statistics assumed here seems to be appropriate, and the superposition procedure (shifting and normalizing the Monte Carlo distribution) works well. The energy depositions are of the order 1 MeV per plane, slightly higher at the outer bins which is due to the increased path length within the scintillator material and the (by about 200 MeV) lower particle energy at larger scattering angles. Bins 9 and 10 show a significant lack of statistics due to the fact that these data were taken with a trigger including the range hodoscope, and this device does not have sufficient geometrical overlap with the forward hodoscope at these large radii.

In order to single out the energy dependence of the ADC calibration constants, histograms containing relative calibration constants (measured, nonuniformity corrected energy deposition[3] divided by Monte Carlo deposition) versus the (uncorrected) measured energy from all energies are merged. A linear fit in these histograms relates the relative calibration constants to the measured energy deposition, of which 2nd order ADC calibration constants are extracted as described in section 4.2. A quadratical fit and extraction of 3rd order ADC calibration constants have also been tried, but the deviation from a linear dependence is very small, such that the coefficients for 3rd order are about 3 orders of magnitude smaller than the 2nd order values which in turn are about 3 orders of magnitude smaller than the 1st order coefficients. Therefore 2nd order calibration was considered to be sufficiently precise.

The formulae used for calculation of energy dependent calibration constants (in each iteration step) are derived in section 4.2. Equation 4.3 has been used to extract 2nd order calibration constants. With these constants, again a run on p-p elastic scattering data at higher energy was done, and new nonuniformity parameters were extracted. The whole procedure - running on data from all energies with extraction of ADC calibration constants, and then running on high energy data with calculation of nonuniformity parameters - has been performed several times, because of the

[3]calibration and nonuniformity constants taken from last iteration

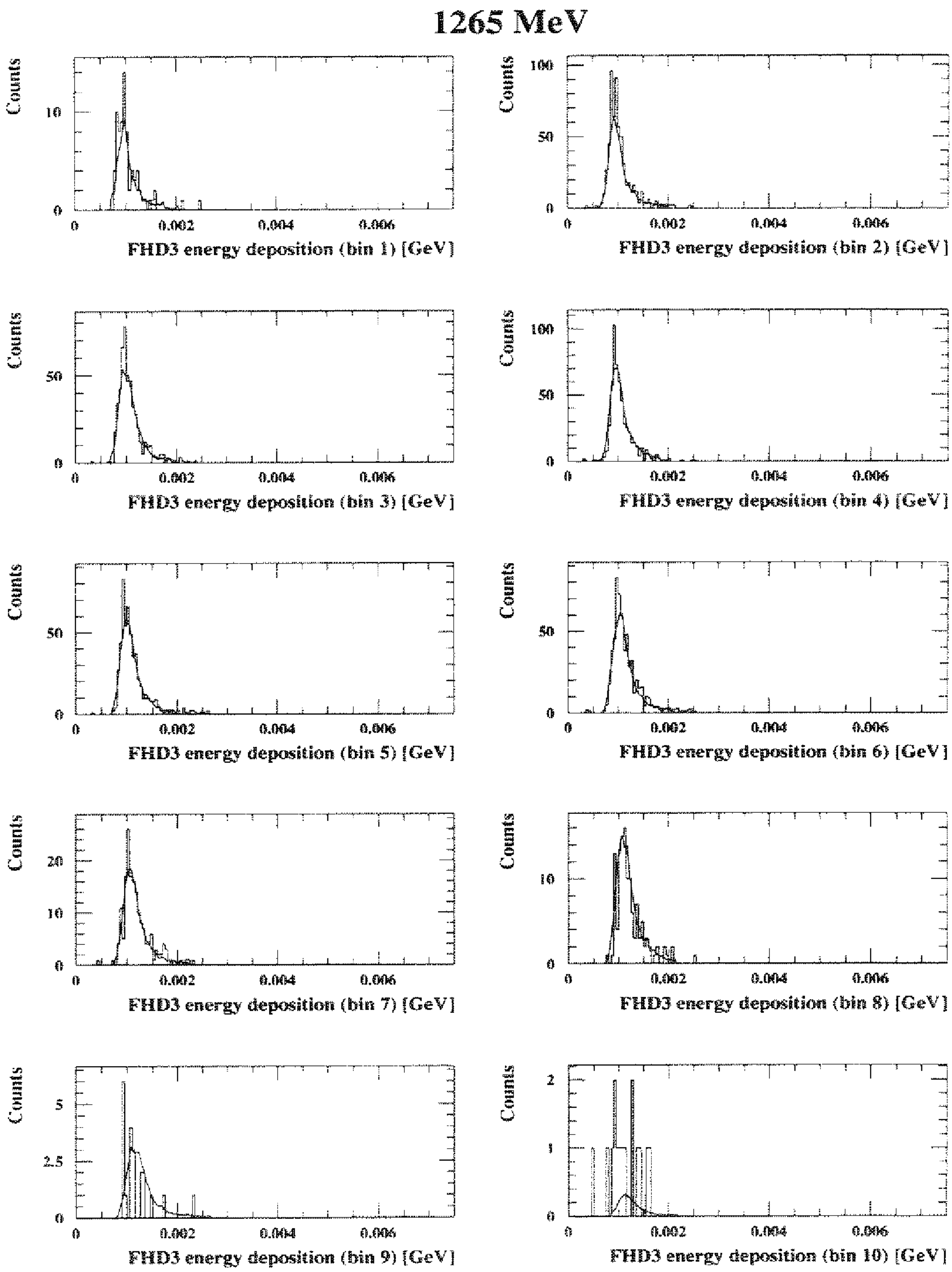

Figure 4.1: Monte Carlo distributions (smooth lines) superposed on measured energy deposition curves at T_p=1265 MeV for different radial bins in the third (straight) forward hodoscope plane.

alternating calculation of calibration and nonuniformity parameters which influence each other.

4.2 Calibration formulae

In a first approach the dependence of the relative calibration parameters on the measured energy deposition for one element can be approximated by a linear equation

$$\frac{A \cdot C_{\mathrm{ADC}}}{l \cdot E_{\mathrm{MC}}} = A_\circ + B_\circ \cdot A \cdot C_{\mathrm{ADC}}, \tag{4.1}$$

where C_{ADC} is the ADC content, E_{MC} the expected energy deposition obtained from Monte Carlo, l the light efficiency, A is the 1st order calibration constant, $A_\circ$ and $B_\circ$ are the constants describing the linear dependence on the measured energy deposition $A \cdot C_{\mathrm{ADC}}$. The left side of equation 4.1, measured nonuniformity corrected energy deposition divided by Monte Carlo energy deposition, might deviate from 1. If there were no pulse height dependence at all, that expresssion would be equal to 1. But in reality, the light output is regressive with increasing pulse height due to quenching and photomultiplier nonlinearity, thus leading to a negative value for $B_\circ$ in the ansatz above. Hereby one assumes that the contribution of the photomultiplier nonlinearity is larger than any energy dependence of the nonuniformity parameters which is therefore not included in this ansatz.

This equation gives an expression for the expected measured energy deposition (MC folded with nonuniformity),

$$l \cdot E_{\mathrm{MC}} = \frac{A \cdot C_{\mathrm{ADC}}}{A_\circ} \frac{1}{1 + \frac{B_\circ}{A_\circ} A C_{\mathrm{ADC}}},$$

which can be approximated by

$$l \cdot E_{\mathrm{MC}} = \frac{A}{A_\circ} \cdot C_{\mathrm{ADC}} - \frac{B_\circ A^2}{A_\circ^2} C_{\mathrm{ADC}}^2 + \ldots. \tag{4.2}$$

The corresponding equation for 2nd order ADC to energy translation is then obtained by replacing A in equation 4.2 by $A + B \cdot C_{\mathrm{ADC}}$. This gives

$$l \cdot E_{\mathrm{MC}} \approx \frac{A}{A_\circ} \cdot C_{\mathrm{ADC}} + \left(\frac{B}{A_\circ} - \frac{B_\circ A^2}{A_\circ^2} \right) C_{\mathrm{ADC}}^2. \tag{4.3}$$

Just for completeness (because this parametrization was also tried), assuming a 2nd order dependence on the pulse height (i.e. replacing A by $A + B \cdot C_{\mathrm{ADC}} + C \cdot C_{\mathrm{ADC}}^2$ in a 2nd order ansatz for equation 4.1), the equation for the energy reconstruction would be

$$\begin{aligned} l \cdot E_{\mathrm{MC}} &= \left(\tfrac{A}{A_\circ}\right)^3 (B_\circ^2 - A_\circ C_\circ) + \left[\tfrac{A}{A_\circ} + 3A^2 B \tfrac{B_\circ^2 - A_\circ C_\circ}{A_\circ^3}\right] C_{\mathrm{ADC}} \\ &+ \left[\tfrac{B}{A_\circ} - \tfrac{B_\circ A^2}{A_\circ^2} + 3 \tfrac{B_\circ^2 - A_\circ C_\circ}{A_\circ^3} A(B^2 + AC)\right] C_{\mathrm{ADC}}^2 \\ &+ \left[\tfrac{C}{A_\circ} - 2\tfrac{ABB_\circ}{A_\circ^2} + \tfrac{B_\circ^2 - A_\circ C_\circ}{A_\circ^3}(6ABC + B^3)\right] C_{\mathrm{ADC}}^3 \\ &+ O(C_{\mathrm{ADC}}^4). \end{aligned}$$

Equation 4.3 was used for calculation of the 2nd order calibration constants. Histograms containing $\frac{A \cdot C_{\mathrm{ADC}}}{l \cdot E_{\mathrm{MC}}}$ versus $A \cdot C_{\mathrm{ADC}}$ from different runs are fitted with a straight line, the crossing with the ordinate giving $A_\circ$, the gradient delivering $B_\circ$. The new calibration constants for 1st and 2nd order in C_{ADC} are then obtained from equation 4.3 by $\frac{A}{A_\circ}$ and $\left(\frac{B}{A_\circ} - \frac{B_\circ A^2}{A_\circ^2}\right)$, respectively, where A and B are taken from the last iteration.

4.3 Results

Generally it must be noticed that the precision of the calibration cannot be better than a few %. The ADC to energy calibration factor for 1st order ADC dependence is of the order 25 keV per ADC count. That corresponds to $\sim 0.6 - 2.5\%$ of the energy deposition in an element of the trigger hodoscope which is typically about 4 MeV for 80 MeV protons and around 1 MeV for 1265 MeV protons, as can be seen from a simple ionization loss calculation according to Bethe-Bloch as is shown in figure 3.12 for the FHD and figure 3.13 for the FRH (see section 3.4). In addition one has uncertainties due to fitting of the Monte Carlo distributions to real data. In these histograms the bin size was chosen as 50 keV, which is at the limit for our statistics. A misadjustment by only one bin therefore corresponds to a relative error of $1.2 - 5\%$. The fit quality can be judged, e.g., by observing the superposition of the Monte Carlo distributions to the Monte Carlo data itself. It was seen that a misadjustment of up to one bin had to be accepted.

The resulting ADC calibration curves using the procedure described above are shown in figure 4.2 for all 24 elements in the second forward hodoscope plane. The response of the system is far from linear. The energy depositions available from the elastic p-p data used for the calibration procedure range from 1 to 4 MeV. Calculations according to the Bethe-Bloch theory predict ~10 MeV mean energy deposition in one FHD plane from ^{3}He at 350 MeV which is the most probable kinetic energy assuming an isotropic phase space distribution. Therefore one has to extrapolate by a factor of 2 to 3 out of the calibration energy range. This might lead to quite large systematic errors. Calibration measurements using double charged particles would be a straightforward improvement of this situation.

Figure 4.3 gives an impression of the radial dependence of the light output obtained from elastically scattered protons passing through the 5 mm thick trigger hodoscope planes at different radii. The number of radial bins has been limited to 10, according to the statistics available in the elastic proton-proton scattering data sample. One bin has a radial height of 5.38 cm, the lowest bin number starting at the inner hodoscope radius of 4.2 cm. Furthermore, due to lack of geometrical overlap between trigger defining range hodoscope and forward hodoscope at the most outside bin, the nonuniformity parameters for radial bin no. 10 have been set equal to those for bin 9 and are not shown in the plot. The dashed lines indicate the response curves obtained by more precise measurements [36] performed at the

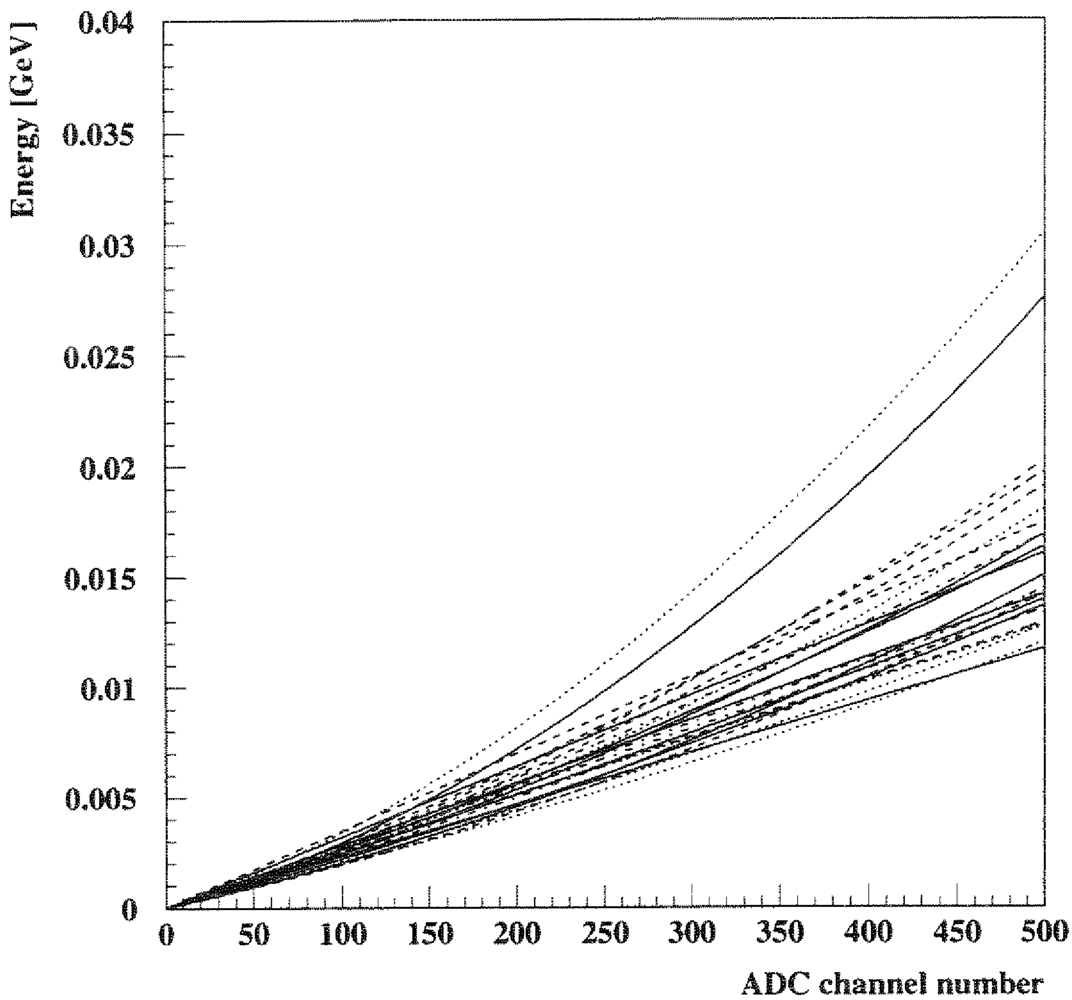

Figure 4.2: ADC to energy calibration curves for all 24 elements of the second forward hodoscope plane.

CERN T11 test beam. This facility provided a monoenergetic proton beam with a nominal momentum of 2 GeV/c ($\pm$ 1.9 %). The position of the particle's impact point was in these measurements determined by wire chambers allowing for a scan of the scintillator surface with a bin size of 8×8 mm^2. Contamination of the beam by other particles than protons was filtered out using the time-of-flight method.

In general, one can see a decrease of the light output efficiency from large radii down to a minimum at a radius of $\sim$ 30 cm (radial bin 5) for the bent scintillators, and again an increase at the tip of the elements. For the straight triangle shaped scintillators the light output at large radii near the photomultiplier was found to be even lower than close to the beam pipe, contradicting the results of reference [36] (dashed bars), even within the error limits exemplarily shown on bin 7. But

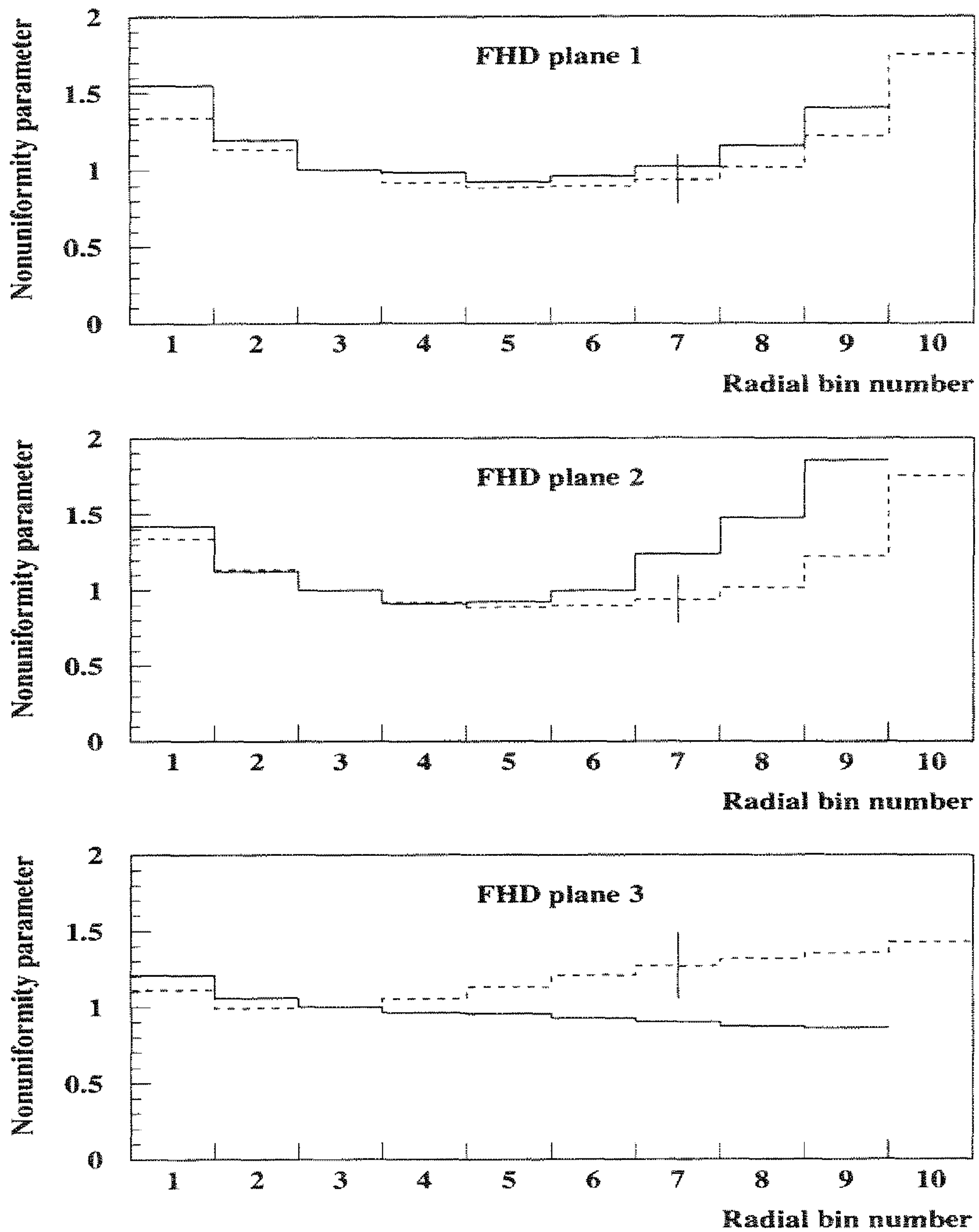

Figure 4.3: Nonuniformity correction factors (= ratio of the light output at the respective radial bin to the light output at radial bin no. 3) for the left bent (top), right bent (middle) and straight (bottom) forward hodoscope plane. The dashed lines show the response according to [36].

the thickness of the scintillators varies by up to ~ 10 % which could explain some difference to the test module.

For the reaction pd$\rightarrow$^{3}Heη at $\sim$ 200 MeV excess energy, the Jacobian is on the edge between radial bin 6 and 7. The angular range up to this hit radius seems to be described well enough with respect to the fact that the energy determination of a charged particle track is mainly done by the forward range hodoscope behind these planes. The forward hodoscope only takes $\sim \frac{1}{30}$ of the total ^{3}He energy deposition in the forward detector. Its off-line purpose is mainly the determination of the track direction.

The larger light output at the tip of the scintillators is due to a kind of mirror effect which occurs because of the shape of the scintillators. Non-parallel surfaces lead to a reflection of the scintillation light in direction of the photomultiplier, even if the photons have been emitted in direction to the tip of the scintillator. This focusing obviously overcompensates efficiency losses in the light collection by absorption and reflection out of the scintillation volume.

4.4 Outlook

The density effect in scintillator material has been neglected so far. In chapter 5 some more information about this feature in general is given, and also with respect to the passage of ^{3}He through scintillator material which of course is of special interest within the scope of this work. This effect which leads to less light output than extrapolated from proton data has to be taken into account during reconstruction of the energy deposition ($\rightarrow$ kinetic energy) of particles other than protons, and on principle even for protons at smaller energies than those used in the calibration procedure.

Furthermore, light pulser signals are available now. In every lightguide an optical fiber has been implemented which is supplied with short light pulses from a common LED (luminescence diode) pulser. The corresponding ADC peaks (easy to identify via the hit multiplicity in a hodoscope plane) will be used to monitor the stability of photomultiplier amplification as well as to make it possible to relate data which has been taken at different times (temperature drift) and energies.

Often statistics are used
as a drunken man uses lampposts -
for support rather than illumination.

Anonymous

Chapter 5

Quenching effects

The calibration of the PROMICE/WASA forward detector has been performed using protons. Heavier particles like deuterons, tritons and especially double charged particles such as ^{3}He and ^{4}He will cause saturation effects in the scintillator material (quenching) leading to less light output. E.g., the light output obtained from α-particles of 120 MeV kinetic energy is about a factor 2 smaller than the one from protons at the same energy [18]. This has to be taken into account during extraction of energy depositions from particles other than protons, and even for protons at smaller energies than those used in the calibration procedure.

5.1 Introduction

Organic, plastic scintillators are widely used in detectors for charged nuclear particles. Though NaI or CsI crystals show better linearity in their fluorescent response, the very high counting rates in some accelerator experiments can more easily be handled with plastic scintillators which have very short decay constants of about 2 to 3 ns (the decay constants of typical inorganic crystals are about three orders of magnitude larger). However, plastic scintillators show non-linear response to heavily-ionizing particles such as multiple charged or stopping particles.

Organic scintillators respond directly to the excitation energy deposited by a penetrating charged particle. Some part of this ionization energy is released as radiation. The scintillation efficiency is of the order of 3.5 % (for anthracene, the best organic material). Absorption of the emitted light leads to an excitation of molecular levels, i.e. of the delocalized valence electrons in the π-molecular orbitals. Some more details about scintillators and the scintillation process in general are given in appendix A.

The response to electrons is linear for particle energies above ~125 keV [10]. The most popular theoretical explanation for the non-linear light output at high ionization densities from heavier, higher charged or stopping particles is that this density along the path of the penetrating particle causes **quenching**, i.e. some kind of saturation effect (ionisation defect). The luminescence centers in the scintillator become saturated because of too large energy deposition. This phenomenon is responsible for the fact that the light output for different particles is not the same even if they lose the same amount of energy within the scintillator material. It is the objective of scintillator response theories to explain observations like this.

5.2 Parametrization of the relative light output

The most cited - because it is extremely successful - approach to describe many of the features of experimental data for organic scintillators stems from J. B. Birks [5]. His theory is based on the assumption that there exists two different energy absorption modes for the molecules along the path of the penetrating ionizing particle. Some part of the excitation energy can be released as radiation, or the ionization energy is dissipated nonradiatively, mainly by losing vibrational energy to the lattice (phonon emission)[1]. C. N. Chou [9] proposed a modified form of Birk's approach to describe the fluorescence light energy emitted per unit path length $\frac{\mathrm{d}L}{\mathrm{d}x}$:

$$\frac{\mathrm{d}L}{\mathrm{d}x} = \frac{S\frac{\mathrm{d}E}{\mathrm{d}x}}{1 + kB\frac{\mathrm{d}E}{\mathrm{d}x} + C\left(\frac{\mathrm{d}E}{\mathrm{d}x}\right)^2},$$

where $\frac{\mathrm{d}E}{\mathrm{d}x}$ is the specific energy loss for the charged particle and S the scintillation efficiency. The constants k and B come from theory where $B\frac{\mathrm{d}E}{\mathrm{d}x}$ is the ratio of the number of molecules dissipating the excitation energy mainly non-radiatively to the number of "radiating" molecules, and k is the corresponding relative quenching probability. The constant C, which is equal to zero in Birk's ansatz, was introduced by Chou in order to optimize the description of the phenomena at high values of $\frac{\mathrm{d}E}{\mathrm{d}x}$.

This equation can also be written as

$$\frac{\mathrm{d}L}{\mathrm{d}E} = \frac{S}{1 + kB\frac{\mathrm{d}E}{\mathrm{d}x} + C\left(\frac{\mathrm{d}E}{\mathrm{d}x}\right)^2},$$

where $\mathrm{d}L$ is the quantity of fluorescence light generated when a charged particle with energy E loses a quantity of energy $\mathrm{d}E$ through ionization along a path increment $\mathrm{d}x$ within the scintillator [10]. The total light $L(E)$ emitted by a charged particle which expends all of its energy E within the scintillator is then

$$L(E) = S\int_0^E \frac{\mathrm{d}\varepsilon}{1 + kB\frac{\mathrm{d}E}{\mathrm{d}x} + C\left(\frac{\mathrm{d}E}{\mathrm{d}x}\right)^2}. \tag{5.1}$$

For electrons with energies above 125 keV, $\frac{\mathrm{d}E}{\mathrm{d}x} \approx 0$, and thus

$$L_e(E) \approx SE + L_o,$$

[1] In this, also some permanent damage will occur which contributes to long-term deterioration of the properties of the scintillator, but it is not responsible for the quenching process being considered [10].

where $L_\circ$ is an arbitrarily assigned offset on a relative scale.

Thus, an energy deposition found in the forward detector has to be multiplied by the correction factor

$$CORR_{\mathrm{theor}}(E) = \frac{L_e(E)}{L(E)} = \frac{SE + L_\circ}{S\int_0^E \mathrm{d}\varepsilon \left(1 + kB\frac{\mathrm{d}E}{\mathrm{d}x} + C\left(\frac{\mathrm{d}E}{\mathrm{d}x}\right)^2\right)^{-1}}, \quad (5.2)$$

where E is the **true** kinetic energy of the particle.

The measured particle energy is in general not equal to the true kinetic energy of the particle before it entered the detector. Therefore an experimental correction factor $CORR_{\mathrm{exp}}(E)$, to be multiplied with each measured energy deposition, has to be determined. It is

$$\frac{E_{\mathrm{true}}}{CORR_{\mathrm{theor}}(E_{\mathrm{true}})} = E_{\mathrm{meas}},$$

where E_{meas} is the measured (kinetic) energy of the particle, E_{true} is the kinetic energy of the particle before it entered the detector, and $CORR_{\mathrm{theor}}(E_{\mathrm{true}})$ the correction factor at this particle energy. From this equation one can - most easily numerically - calculate a new experimental correction function $CORR_{\mathrm{exp}}(E)$ which gives a correction factor for each **measured** particle energy in order to obtain directly the "true" kinetic energy of the particle:

$$E_{\mathrm{true}} = CORR_{\mathrm{exp}}(E_{\mathrm{meas}}) \cdot E_{\mathrm{meas}}. \quad (5.3)$$

5.3 Experimental quenching correction functions

What is needed in order to extract the quenching correction function for a given particle is a measurement of the relative light output obtained from this particle and from electrons. The latter is necessary to normalize to the arbitrary chosen scale for the relative light output and to fold out the intrinsic amplification curve of the measuring device (e.g. photomultiplier). Craun and Smith [10] have measured protons, deuterons and even the response to electrons (no tabled values but diagrams), but they did not measure heavier or even double-charged particles such as e.g. ^{3}He which is of special interest within the scope of the PROMICE project. Becchetti et al. [1] measured protons, deuterons, ^{3}He, ^{4}He and even heavier ions, but they do not show a reference curve for the electron response. Therefore these data are only useful to describe the light output obtained from heavier ions relative to the light output from protons. Gooding and Pugh [18] have given light output response data for protons, deuterons, tritium and α-particles, and also give a reference point for the electron response, but again, no data for ^{3}He.

The correction functions $CORR_{\mathrm{theor}}(E)$ for protons and deuterons according to equation 5.2 have been directly taken from [10], since Craun et al. also give the reference curve for the response to electrons. The parameter values are listed in

Particle	S [a.u.]	kB [g cm^{-2} GeV^{-1}]	C [g^2 cm^{-4} GeV^{-2}]
p	2113000	12.9	9.59
d	1915000	9.17	4.6

Table 5.1: Parameters [10] describing the correction functions for protons and deuterons according to equation 5.2.

table 5.1. In order to get the theoretical correction function for ^{3}He, the data of Becchetti et al. [1] have been fitted according to equation 5.1, with S, kB and C as free parameters. The result can be seen in figure 5.1. In this, $\frac{dE}{dx}$ was calculated

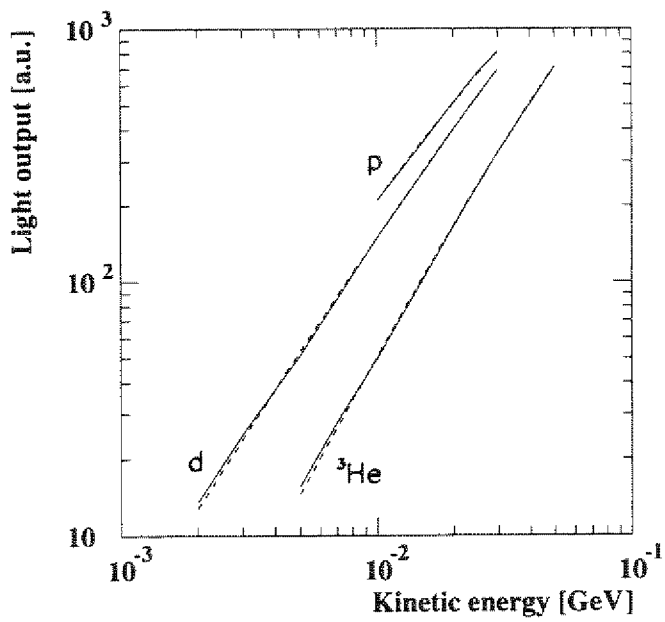

Figure 5.1: Response of NE102 to protons, deuterons and ^{3}He (solid lines: data of Becchetti et al. [1], dashed lines: fits according to equation 5.1).

numerically according to the Bethe-Bloch formula with an effective[2] charge of the medium of $Z_{\text{med}} = 5.612$ and atomic number $A_{\text{med}} = 11.157$. Becchetti's data was measured using NE102 scintillator material. This is very similar to BC-404 which is used in the PROMICE/WASA forward detector. NE102 has $4.75 \cdot 10^{22}$ C-atoms per

[2]In a mixture or compound, the rate of energy loss is approximately $\frac{dE}{dx} = \sum f_i \frac{dE}{dx}|_i$, where f_i is the fraction by weight of the i-th element and $\frac{dE}{dx}|_i$ the mean rate of energy loss in this element. Plastic scintillator material such as Bicron's BC-404 (used e.g. for the forward trigger hodoscope) consists of typically 92 % carbon and 8 % hydrogen (percent in weight), i.e. H:C$\simeq$1.1 (in volume).

cm^3, BC-404 contains $4.74 \cdot 10^{22}$ C-atoms per cm^3, and the H:C ratio (in volume) is 1.032 for NE102 resp. 1.099 for BC-404. The presence of oxygen and nitrogen, so far as the density effect is concerned, can be neglected [28].

From the fits one can derive a correction function for ^{3}He relative to protons, and by multiplying this function with the absolute correction function for protons described above, one gets the absolute correction function for ^{3}He relative to electrons.

As the goal is to obtain an "experimental" correction function for the particles such that the measured energy deposition just has to be multiplied by the corresponding correction factor for this energy, equation 5.3 has been solved numerically, and the result was normalized to the constraint that there is no correction for quenching at very high energies ($CORR_{exp}$(2 GeV)=1).

The original fit function 5.1 is not of any practical use in an offline analysis because of the integral term which is very cpu-time consuming. Therefore, the final "experimental" correction functions have been fit again according to the function

$$CORR_{exp}(E) = \frac{P_1}{P_2 + P_3E + P_4E^2 + P_5E^3} + P_6. \tag{5.4}$$

The correction functions together with the fit results are shown in figures 5.2, 5.3 and 5.4 for protons, deuterons and ^{3}He, respectively.

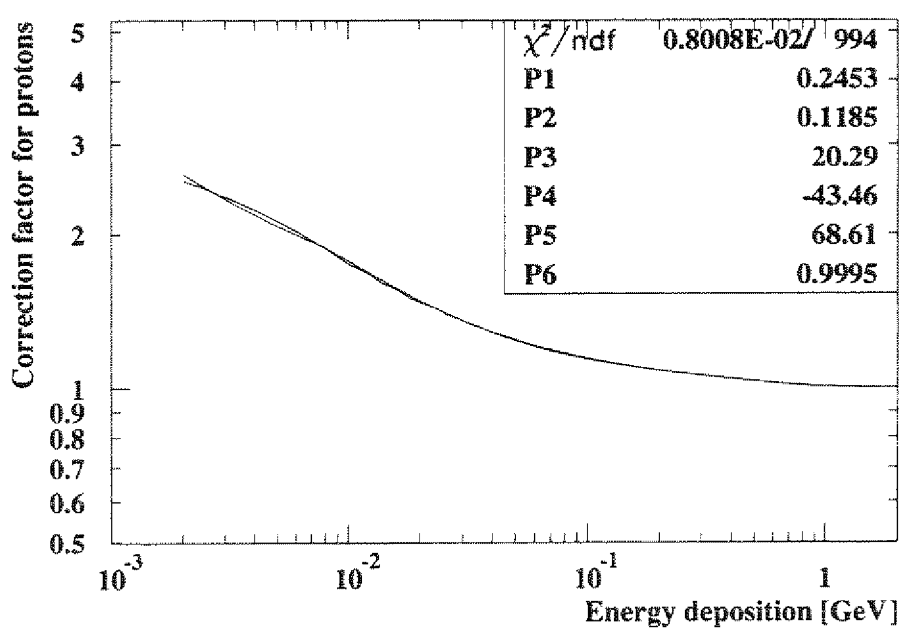

Figure 5.2: Experimental correction function for protons together with a fit according to equation 5.4.

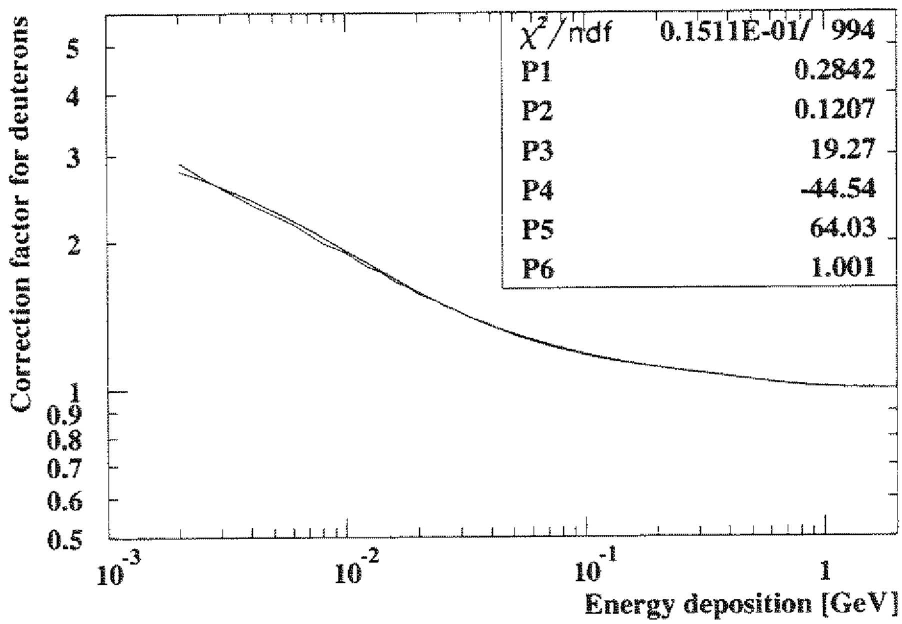

Figure 5.3: Experimental correction function for deuterons together with a fit according to equation 5.4.

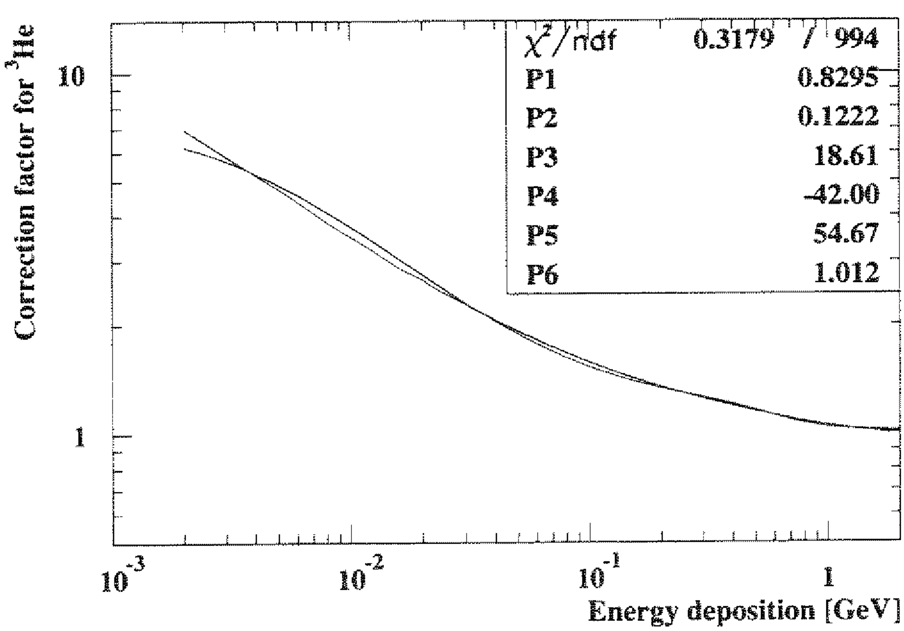

Figure 5.4: Experimental correction function for ^{3}He together with a fit according to equation 5.4.

5.4 Outlook

The correction functions given by equation 5.4 and the parameters specified in figures 5.2, 5.3 and 5.4 can now be used to correct for the quenching effect if one knows which particle actually has been observed in the detector, because this determines which one of the functions has to be applied. For this decision, a particle identification is necessary which in turn depends on the energies deposited in the consecutive detector planes. This demands some kind of iterative (fit) procedure. In a first approximation which was done here, one can simply apply the quenching correction for protons to each charged particle which has been measured in the forward detector, then perform the particle identification using the resulting energy depositions, and after that make a correction relative to protons if the particle was identified as a heavier projectile.

Chapter 6

Kinematical fit

6.1 General method

Kinematical constraints can be used to single out a specific reaction channel, i.e. whenever a decision has to be made about whether the measured observables are within their individual errors consistent with the assumption of a certain reaction process. In that case, one is able to "improve" the measurements by a kinematical fit. This is done by adjusting the measured and unmeasured observables according to their uncertainties in such a way that the set of kinematical constraints, which connects them, is fulfilled as well as possible.

The four constraints used here are momentum and energy conservation. The target particle is assumed to be at rest at the vertex without errors. With masses fixed, beam and identified particle in the forward detector give three measured observables each, while the missing particle in a two-body exit channel leaves three unknown parameters, thus leading to a **one-constraint fit** when applying momentum and energy conservation.

The least squares method has been used since, for a linear dependence of the parameters, this method has the virtue that it, even for small samples, produces unbiassed estimators of minimum variance. All measured quantities are fitted to give the best solution to the constraint equations, and the probability that the hypothesis of a certain reaction channel is correct is also given. Briefly, the least squares principle is as follows [15].

Let $\vec{\zeta}$ be a vector of N_{obs} ideal observables. The measured quantities are the starting values $\vec{\zeta}^{\circ}$ with their respective errors given in the covariance matrix $V(\vec{\zeta}^{\circ})$. Denote that the measurements do not necessarily have to be independent. The set of N_{unm} unmeasured variables is specified as vector $\vec{\xi}$. The measurable and unmeasurable observables are related by a set of N_{cst} constraint equations,

$$f_k(\vec{\zeta}, \vec{\xi}) = 0, \quad k = 1, .., N_{\mathrm{cst}}.$$

The least squares principle states that the best set of estimates for $\vec{\zeta}$ and $\vec{\xi}$ are those values for which

$$\chi^2(\vec{\zeta}) = (\vec{\zeta} - \vec{\zeta^\circ})^T V^{-1} (\vec{\zeta} - \vec{\zeta^\circ}) = \text{minimum},$$

$$\vec{f}(\vec{\zeta}, \vec{\xi}) = \vec{0}.$$

Choosing the method of Lagrangian multipliers to solve this minimization problem, N_{cst} additional unknowns are introduced, the vector $\vec{\lambda}$, and

$$\chi^2(\vec{\zeta}) = (\vec{\zeta} - \vec{\zeta^\circ})^T V^{-1} (\vec{\zeta} - \vec{\zeta^\circ}) + 2\vec{\lambda}^T \vec{f}(\vec{\zeta}, \vec{\xi}) = \text{minimum}$$

is required. The derivatives of χ^2 with respect to all unknowns shall be equal to zero. That delivers the following equations:

$$\nabla_\zeta \chi^2 = 2V^{-1}(\vec{\zeta} - \vec{\zeta^\circ}) + 2F_\zeta^T \vec{\lambda} = \vec{0},$$

$$\nabla_\xi \chi^2 = 2F_\xi^T \vec{\lambda} = \vec{0},$$

$$\nabla_\lambda \chi^2 = 2\vec{f}(\vec{\zeta}, \vec{\xi}) = \vec{0},$$

where the matrices F_ζ and F_ξ are defined by

$$(F_\zeta)_{ki} := \frac{\partial f_k}{\partial \zeta_i}, \quad (F_\xi)_{ki} := \frac{\partial f_k}{\partial \xi_i}.$$

Thus

$$V^{-1}(\vec{\zeta} - \vec{\zeta^\circ}) + F_\zeta^T \vec{\lambda} = \vec{0},$$

$$F_\xi^T \vec{\lambda} = \vec{0},$$

$$\vec{f}(\vec{\zeta}, \vec{\xi}) = \vec{0}.$$

The solution to this set of equations with $(N_{\text{obs}} + N_{\text{unm}} + N_{\text{cst}})$ unknowns has usually to be found via an iterative procedure. In each step of the procedure, new values for the unknown variables will be calculated until the convergence criteria are fulfilled. This is the case if the constraint equations and the change in χ^2 between successive steps are sufficiently small. After the final step, the covariances of the obtained "improved" measurements are calculated applying the law of error propagation. The errors on the fitted quantities are in general smaller than the errors in the observations, and the fitted quantities will be correlated, even if the measurements were independent.

6.2 The fitting procedure

The following values have to be specified for the kinematical fit procedure:

- The masses of all four particles participating in the reaction.

- Beam particle momentum vector and errors.
- Momentum vector of the measured particle with errors.
- At least one convergence criterium, either a limit for the difference in χ^2 between successive steps, or limits for the four constraints (momentum and energy), or both. Suitable limits have to be found via Monte Carlo studies in order to optimize the efficiency of separation between different reaction channels.
- The maximum number of iterations per event.
- Optional, in order to make the selection of a specific reaction channel more strict, it is possible to limit the range for variation of the input parameters. By doing this, the efficiency for "good" events will slightly decrease, but less than for other reaction channels, thus leading to a cleaner event sample.

α	number of standard deviations
31.67 %	1
4.55 %	2
0.27 %	3
$6.4 \cdot 10^{-3}$ %	4
$5.8 \cdot 10^{-5}$ %	5
10 %	1.64
5 %	1.96
1 %	2.58
0.1 %	3.29
0.01 %	3.89

Table 6.1: Confidence coefficients for gaussian errors.

In table 6.1 some confidence coefficients α (= 1 - confidence level) for gaussian errors are listed. From that one can see the correspondence between variation interval limits and efficiency loss.

If an event is accepted, fit results for the momentum vectors of beam, measured and unmeasured particle are obtained together with their respective errors. Since the fit procedure is shifting the measured observables in a way that the kinematical constraints are fulfilled as well as possible, the missing mass distribution of the undetected particle in a two-body exit channel calculated from the improved measurements of the observed particle in accepted events will of course be a very sharp peak at the correct missing mass value specified on input, its width depending on how restrictive the convergence limits have been defined. For the plots shown below, the kinematical fit has therefore only been used to decide whether an event belongs to the desired reaction channel or not, and the missing mass was calculated from the original measurements.

In order to find optimum values for the convergence criteria, one should perform Monte Carlo studies with a realistic detector resolution for the reaction in question. There one can make the criteria as sharp as possible under the condition not to lose "good" events. By choosing these parameters for a run on real data, one will get optimum possible background rejection (as part of the total background subtraction) and selection of a specific reaction channel - in addition to the "improved" measurements. In figure 6.1 the response of the kinematical fit to Monte Carlo data

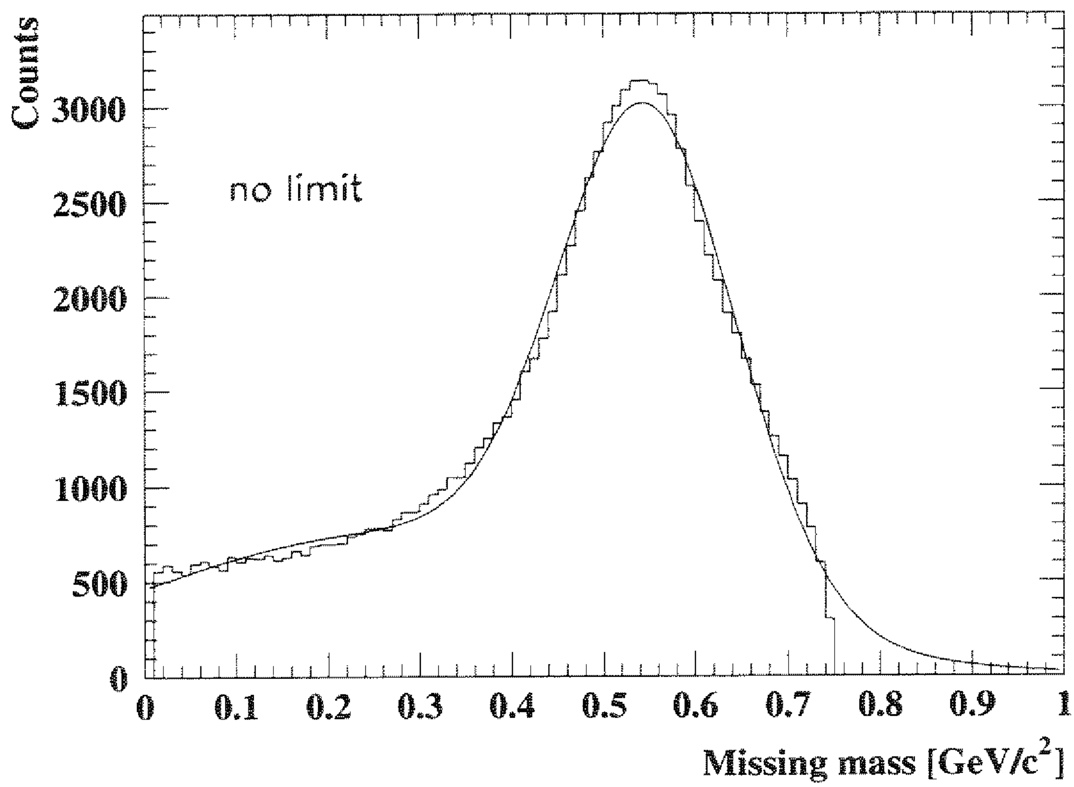

Figure 6.1: Response of the 1C-fit to MC data for the reaction pd→^{3}Heη at T_p=1250 MeV when assuming a mass for the unmeasured particle between 0 and 1 GeV/c^2. 3200 counts corresponds to 100 % acceptance.

is shown for the reaction pd→^{3}Heη at T_p = 1250 MeV. This picture was obtained by assuming masses in the range 0 to 1 GeV/c^2 for the unmeasured particle and studying the response of the fit to these wrong assumptions, i.e. scanning the "rejection efficiency" for a range of missing masses. The variation of the observables was unlimited. The crude fit in figure 6.1 is a double gaussian function,

$$\begin{aligned} f(x_{\mathrm{MM}}) &= (2568 \pm 29) \cdot \exp\left(-\frac{1}{2}\left(\frac{x_{\mathrm{MM}}-(0.5486\pm0.0007)}{0.0964\pm0.0011}\right)^2\right) \\ &+ (749 \pm 10) \cdot \exp\left(-\frac{1}{2}\left(\frac{x_{\mathrm{MM}}-(0.2702\pm0.0096)}{0.2747\pm0.0081}\right)^2\right), \end{aligned}$$

i.e. the full width at half maximum of the dominating peak at the true η mass is 227 MeV/c^2. This shows that events which involve another particle than an η in conjunction with the measured ^{3}He particle will - within a fixed number of iterations - be less often accepted by the fit routine than true η events. Thus single π° production is strongly suppressed. Since within the experimental missing mass resolution of 80 MeV/c^2 (compare section 3.4.3) the multi-pion channels are on principle undistinguishable from the η channel, they cannot be rejected, but at least also suppressed.

6.3 Cleaning an event sample

If the range for variation of the input parameters is decreased, the selection of a specific reaction channel becomes more restrictive, i.e. the final event sample will be "cleaner". When using the fit for a cleaning of real data, one may have to choose a wide range or even no range limit at all. In table 6.2 the acceptance of the

variation range	acceptance for π°	acceptance for $\pi^\circ\pi^\circ$	acceptance for η	max. number of iterations
$\pm1\sigma$	0.037%	34.3%	97.1%	10
$\pm2\sigma$	0.55%	56.3%	97.8%	10
$\pm3\sigma$	10.8%	64.1%	97.8%	10
no limit	21.4%	67.5%	97.8%	10
no limit	42.2%	77.8%	98.1%	45

Table 6.2: Acceptance of the kinematical fit for different reaction channels when limiting the number of iterations. σ stands for the errors in the measurements.

kinematical fit for single π°, double π° and η production in the reaction pd$\rightarrow^3$HeX at $T_{\mathrm{p}} = 1250$ MeV is shown. The convergence limits were:

- change in χ^2 between successive iteration steps $< 3 \cdot 10^{-3}$
- difference between the beam momentum x-component and the sum of the x-components of the outgoing particles $< 6 \cdot 10^{-6}$ GeV/c
- ... y-components ... $< 6 \cdot 10^{-6}$ GeV/c

- ... z-components ... $< 2 \cdot 10^{-6}$ GeV/c
- difference between the total energy in the initial and the exit channel $< 6 \cdot 10^{-8}$ GeV.

No cut on χ^2 was done here. Without any limitation for the variation of the measured observables in units of their respective errors (σ), the fit still accepts $\sim 22\%$ single π° events. One can almost eliminate these events (without CsI and tracker) by restricting the variation interval to e.g. $\pm 1\sigma$, because the errors of the input parameters (especially track direction) are already very large with the present detector setup[1]. By doing that, the efficiency for η-events would be decreased by 0.7 % compared to the efficiency without any variation limit, which is negligible. The reduction is not of the order 30% as one would expect from table 6.1; the fit is still able to converge for "good" events even within the smaller σ-range employing sufficient iteration steps. On the other hand, the maximum number of iterations should not be made too large because then also more backgound events are accepted, as can be seen from the last row in table 6.2. With a 1σ-interval the background from single π° production is negligible, still having 97 % acceptance for η-events. The background from double π° production can of course not be completely rejected but at least reduced by a factor 3. For a significant improvement of this background suppression, the information from CsI and tracker is essentially needed.

The effect of limiting the variation range for input parameters on the missing mass resolution has been tested on Monte Carlo data for the reaction pd$\rightarrow{}^3$Heη at $T_p = 1250$ MeV in the same way as described above, namely by assuming wrong missing masses (in the range from 0 to 1 GeV/c^2) for the undetected particle and checking the response of the kinematical fit, i.e. the rejection efficiency. Figures 6.2, 6.3 and 6.4 show the missing mass distributions for variation of the observables within $\pm 3\sigma$, $\pm 2\sigma$ and $\pm 1\sigma$, respectively, around their measured values. These have to be compared to figure 6.1. As one can see, the selection of the ^{3}Heη channel becomes cleaner with decreasing variation range without almost any loss in acceptance.

The method described here is a possibility to increase the ratio of ^{3}Heη to ^{3}HeX events without performing a cut on the χ^2-value obtained for each event after conversion of the fit procedure. Unfortunately, this has the disadvantage that the final event sample cannot be easily interpreted with respect to its content of "true" η events ($\rightarrow$ confidence level) as is possible by a χ^2-cut only (and close to ∞ iteration steps allowed for each event). But it was shown that a limitation of the number of iterations per event has no significant influence on the acceptance of η events while it strongly suppresses other background channels (compare table 6.2). This was essential for the observation of the η peak in the experimental missing mass distribution extracted from measured ^{3}He tracks in the forward detector as described in chapter 7.3.

[1] Errors specified: $\frac{\Delta P_{beam}}{P_{beam}} = 10^{-3}$, $\Delta E_{meas} = 6$ MeV, $\Delta\theta = 1^\circ$, $\Delta\phi = 2^\circ$.

The possibility to select an enriched ^{3}Heη sample by limitation of the variation of the measured observables during the fit procedure has only been used for test purposes in the beginning of the data analysis. The final missing mass and angular distributions have been extracted without any such limitation but with maximum 45 iteration steps per event since this was found (by Monte Carlo) not to affect significantly the acceptance for "good" events while this demand suppresses background and thus spares cpu time. The effect is similar to a cut on χ^2 as figure 6.5 indicates. The picture top left shows the relation between the missing mass and the corresponding χ^2-value, top right the projection onto the abscissa is shown, i.e. the missing mass distribution without any cut on χ^2. Per event 500 iteration steps were allowed, i.e. eleven times more than in the final analysis, which should improve the acceptance of the fit for "true" ^{3}Heη events beyond the 98.1 % within 45 iteration steps per event (see table 6.2). The limitation to a maximum number of iterations per event during the kinematical fit procedure indirectly corresponds to a cut on χ^2 since, according to the picture top left, events with missing mass values far away from the η mass will need more iteration steps until the conversion limits are fulfilled, i.e. the initial missing mass is shifted to the "true" value given as a constraint to the fit routine. The effect of cuts on χ^2 with stepwise decreased threshold is shown in the six distributions below in figure 6.5. With decreasing threshold the confidence level for having "true" ^{3}Heη events of course increases, but when applying cuts sharper than $\chi^2 < 5$ it is not possible to estimate the amount of background in the remaining peak. The correct determination of background is essential for the extraction of angular distributions as described in section 7.5. Therefore no additional cut on χ^2 was performed apart from the demand that the fit procedure had to converge within 45 iteration steps which corresponds to χ^2-values below ~ 7.

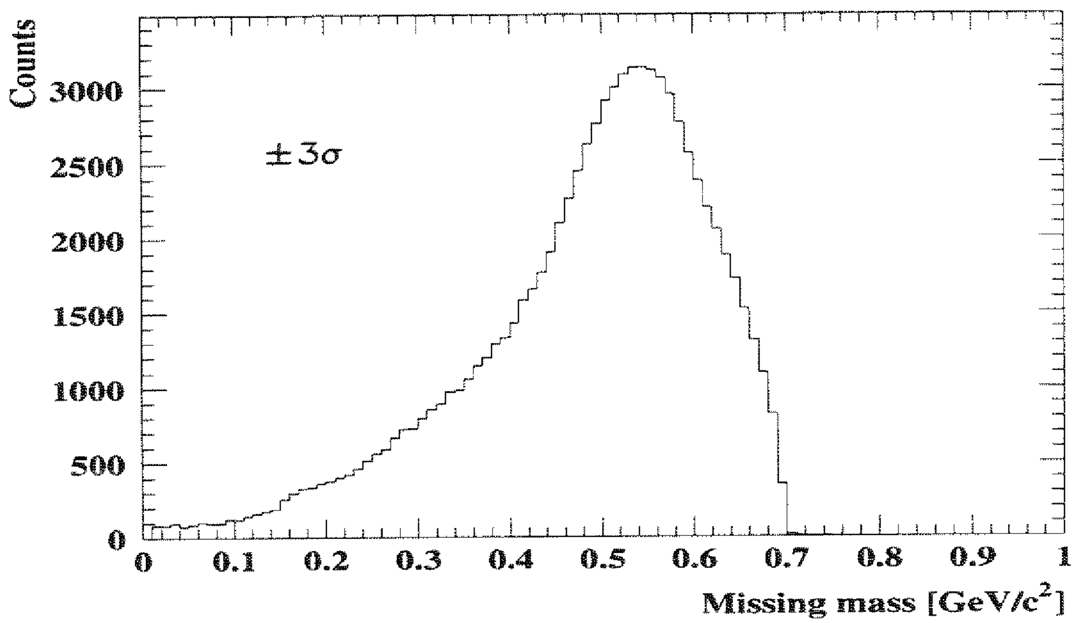

Figure 6.2: Missing mass resolution with a $\pm 3\sigma$ interval for the variation of input parameters.

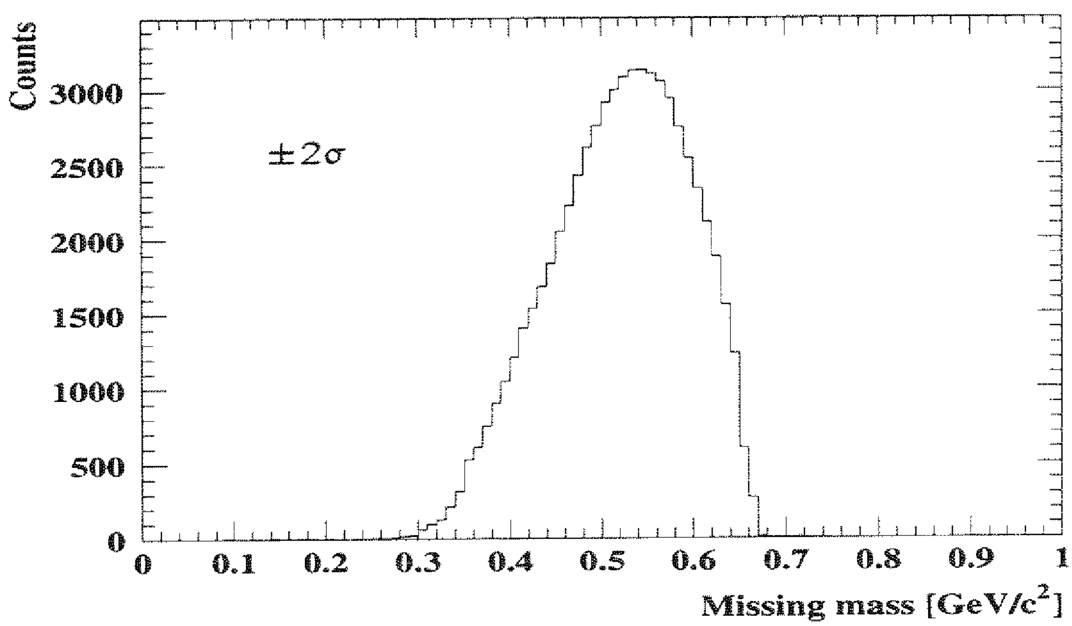

Figure 6.3: Missing mass resolution with a $\pm 2\sigma$ interval for the variation of input parameters.

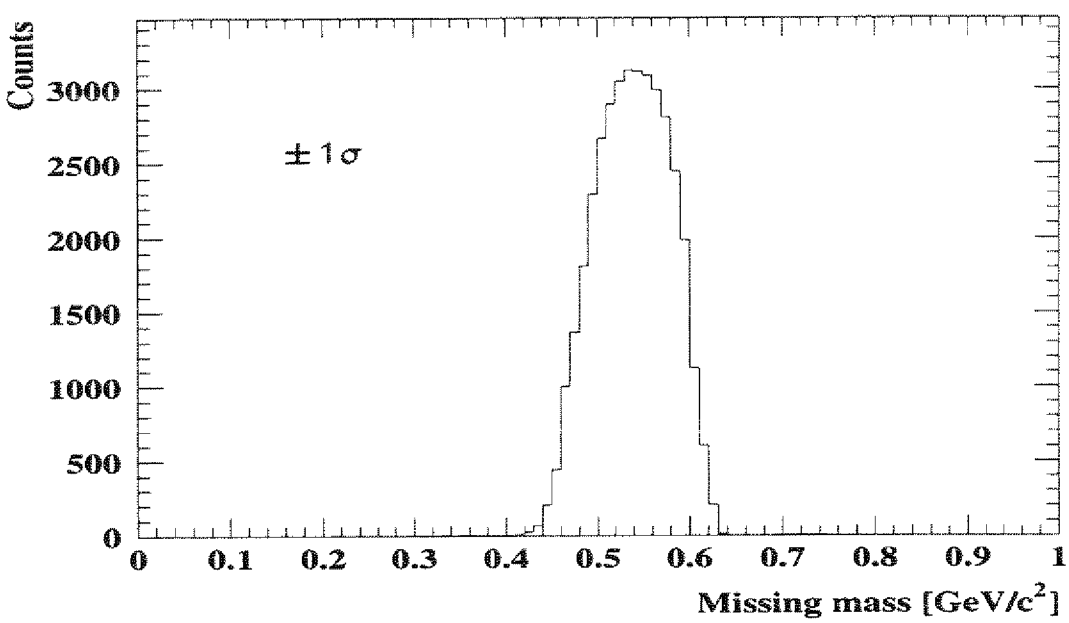

Figure 6.4: Missing mass resolution with a $\pm 1\sigma$ interval for the variation of input parameters.

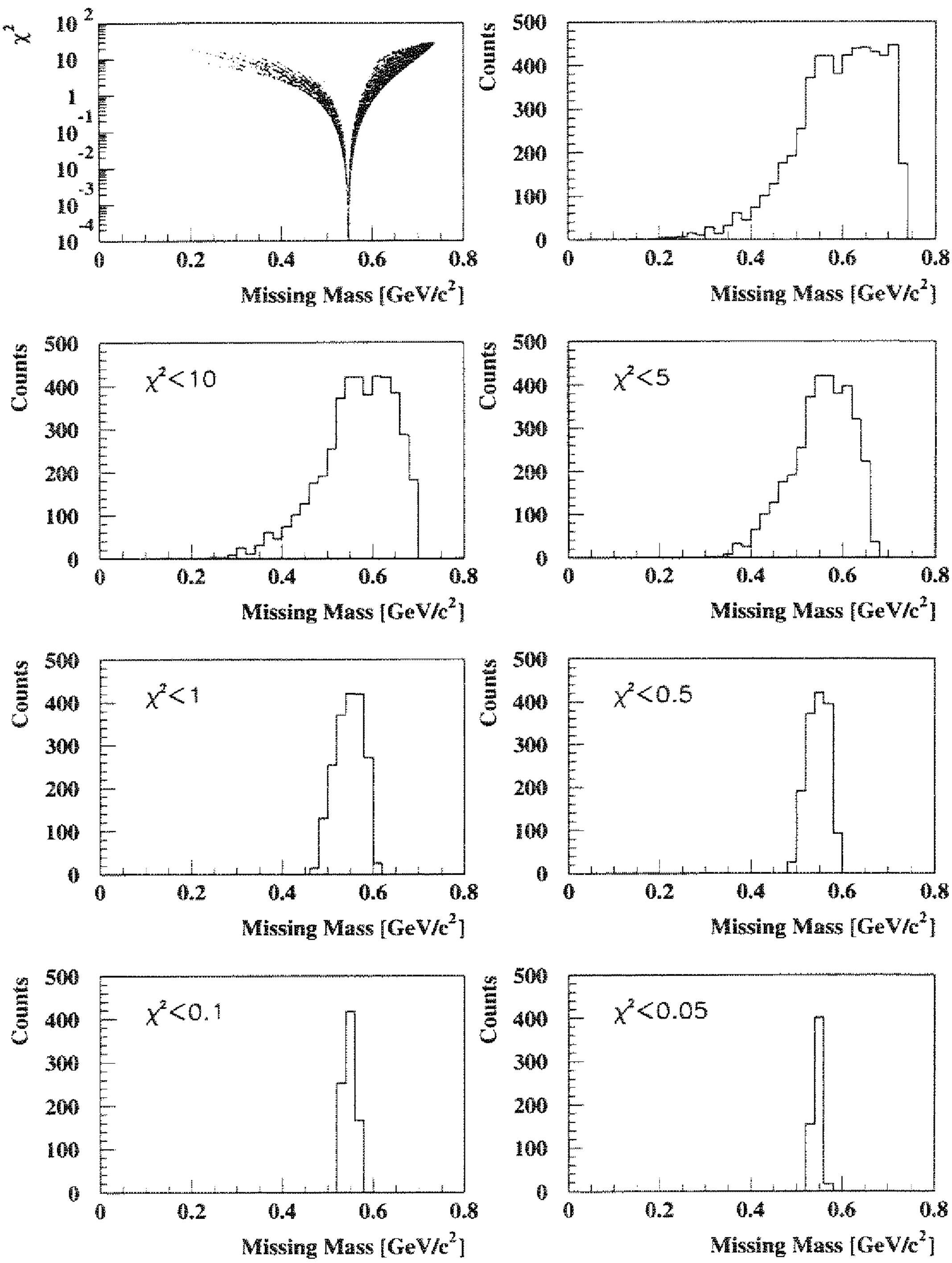

Figure 6.5: χ^2 versus missing mass for all events (top left), corresponding missing mass spectrum without a cut on χ^2 (top right), and the same missing mass distribution with stepwise decreased cut on χ^2 (below) for all events from the reaction pd$\to$^{3}HeX at T_p=1250 MeV.

Chapter 7

Data analysis and results

7.1 The offline analysis scheme

The offline analysis scheme as sketched in figure 7.1 was applied to real data from the experiment as well as to Monte Carlo data. This is favourable since the Monte Carlo data underly exactly the same cuts and reconstruction routines as real experimental data. Especially when calculating the complete detection efficiency - not only the geometrical, but including also reconstruction inefficiencies and cuts - this feature becomes essential.

After initialization of processing flags, reconstruction parameters and definition of the detector alignment, events are read from the respective storage medium (ExaByte or harddisk). In the following accelerator parameters (e.g. magnetic field, time in cycle), hardware and software scalers are processed for each event. Then hit coordinates are calculated and (previously determined) pedestals subtracted. The next stage of the offline analysis is to convert the ADC contents to the corresponding energy depositions. This has on principle to take into account a fully position and energy dependent calibration of the detector elements which is only possible after track reconstruction. The following track reconstruction in turn depends on the energy depositions in the respective elements since the center-of-gravity of a cluster formed by the hit elements in the respective plane is used in the track finding algorithm. After successful track reconstruction the corresponding particle types are identified and their energy determined. Finally physics routines are performed, e.g. fitting of the measured observables to the kinematical constraints, and the output is presented.

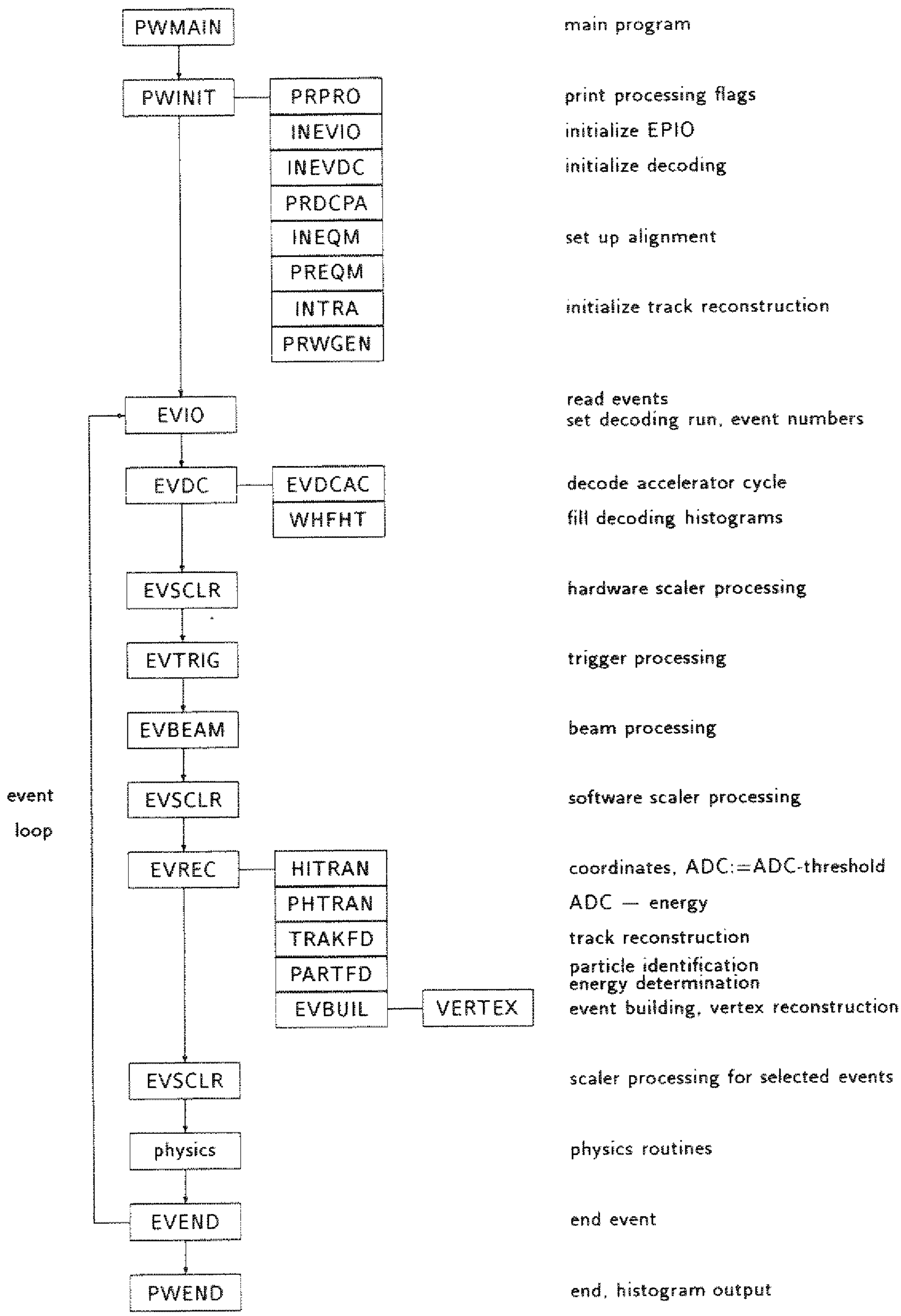

Figure 7.1: Flow chart of the offline data analysis program.

7.2 ^{3}He identification

7.2.1 $\Delta E - E$ selection

The first task in the analysis of p-d reactions with respect to the channel ^{3}Heη is the identification of the double charged recoil nucleus in the forward detector. That can be done using a two-dimensional $\Delta E - E$ scatter plot where the total energy deposition in the three-layered forward hodoscope (FHD) is plotted against the total energy deposition in the range hodoscope (FRH). Figure 7.2 shows the graphical data representation using the program package PAW (=Physics Analysis Workstation) developed at CERN. By default, this program does **not** print one dot in the scatter plot per datum entry but instead scales the number of points with respect to the maximum bin content. Thus one dot in the two-dimensional histogram does not correspond to one but to a number of entries. This is normally useful since a huge number of dots mostly conceals any structure in the distribution. But in cases where the point density is changing drastically over the whole picture, this automatic scaling has the disadvantage that it does not reveal small structures. This effect becomes obvious when limiting the maximum number of entries per two-dimensional bin in this scatter plot to a small number (50 in this case). Now the ^{3}He band becomes visible (see figure 7.3). Without this manual scaling the minimum ionizing single charged particles from quasi-elastic scattering dominate the statistics by far because of the immense difference between the quasi-elastic p-d cross sections, which are of the order of tens of mb, and the ^{3}HeX channels which are expected to have a total production cross section of the order μb. The ^{3}He "band" appears as a spot, even though the kinematic limits allow for a variation of the ^{3}He kinetic energy between 200 and 700 MeV; the relative large cross section at the Jacobian peak corresponding to a kinetic energy of 370 MeV is dominating the entries in figure 7.3. The separation of candidates for ^{3}He events from the quasi-elastic channels was performed by a hyperbola shaped cut slightly above the band resulting from single charged particles (see figure).

7.2.2 ΔE sampling method

An advanced method to identify particles is offered by the energy depositions in several planes the particle has passed through. The rate of energy loss per unit path length is sampled - the results becoming more precise with increasing number of planes. The comparison of measured energy depositions with those obtained from detailed Monte Carlo calculations for the particles in question leads to a χ^2 for each particle type,

$$\chi^2 = \frac{1}{N_{\mathrm{pl}} - 1} \sum_{\mathrm{i}=1}^{N_{\mathrm{pl}}} \left(\frac{edep_{\mathrm{i}}^{\mathrm{meas}} - edep_{\mathrm{i}}^{\mathrm{MC}}}{\sigma_{\mathrm{i}}} \right)^2 ,$$

where N_{pl} stands for the number of planes and σ_{i} for the error in the measurement. For every particle type χ^2 is minimized, and the type giving the lowest χ^2, i.e.

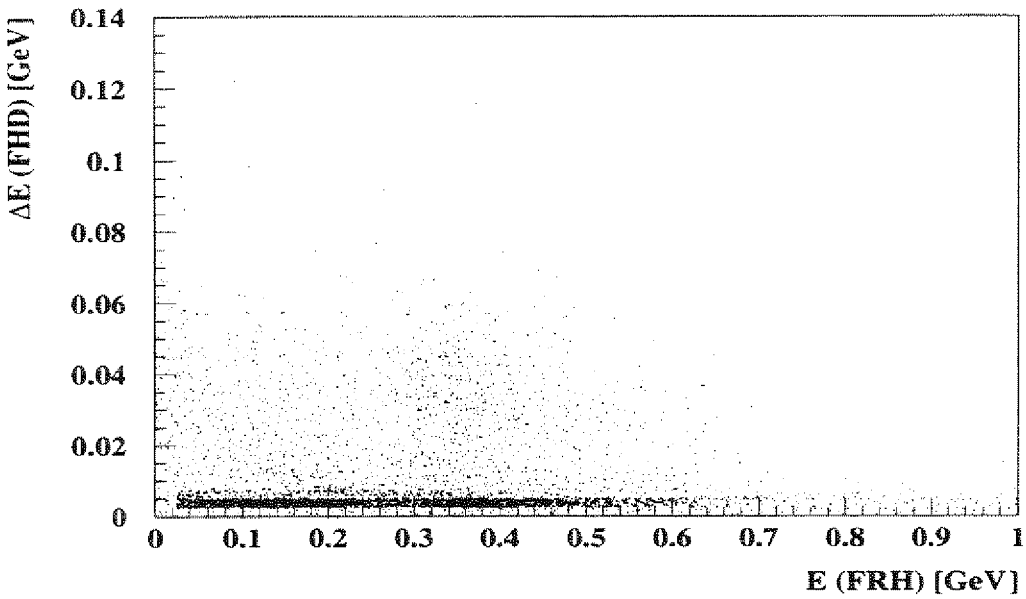

Figure 7.2: Total energy deposition in the forward hodoscope versus total energy deposition in the range hodoscope.

optimum correspondence to the simulated response, is assigned to the track. The only free parameter in this variation procedure is the kinetic energy of the incident particle. After successful conversion of the fit procedure one obtains in addition to the particle type an improved value for the incident energy.

The parameters needed for this identification procedure are the energy depositions for all individual planes together with the spread on the lower und upper side of these distributions for each particle type and kinetic energy range in question. Special care has to be taken in the regions where particles start to penetrate a plane, i.e. if the particle range is of the same order as the thickness of a set of detector planes. Further problems can arise if the sampling is too coarse, i.e. if a huge part of the particle's energy is contained within one plane. Then different particles will give the same ΔE in that plane thus leading to bad identification. Similar problems arise for minimum ionizing particles which deposit the same amount of energy in the consecutive planes.

The software routines necessary for this identification have been tested on the Monte Carlo data itself. There the identification was working perfectly well. But on real data the multi-particle background caused severe problems since it produced energy depositions in the consecutive planes which led to similar χ^2 values as those expected from ^{3}He. Therefore the $\Delta E - E$ curves for the identified particles showed strange structures at their respective edges. Although it was possible to take this information as an additional constraint when selecting a very clean sample of ^{3}He

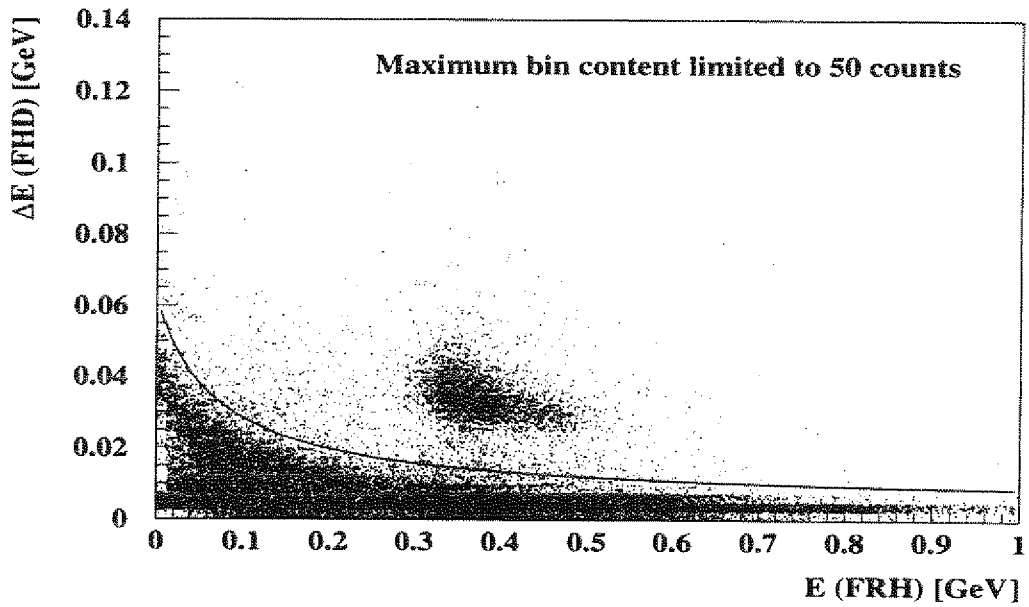

Figure 7.3: Total energy deposition in the forward hodoscope versus total energy deposition in the range hodoscope with limited maximum bin content.

tracks, the method alone was not sufficiently reliable.

7.3 Missing mass of the η

The missing mass of the η is calculated from the measured ^{3}He track in the forward detector. The distribution obtained from data at T_p=1250 MeV is shown in figure 7.4. The dashed line is a fit to the background taking only missing mass values below 490 MeV/c^2 and above 560 MeV/c^2 into account. The result after subtraction of this background is shown in figure 7.5. The tail down to low missing mass values corresponds to the results from Monte Carlo calculations (compare with figure 3.16). Integration gives 170 η's in total. In the sample at T_p=1276 MeV 35 η's in total were found applying the same method. That corresponds to the rates measured at Saturne [26].

The tracks in this final ^{3}He sample had to fulfil several conditions:

- In each forward hodoscope (FHD) plane one and only one hit element (ADC content above pedestal) has to be found together with a signal in the TDC range. This condition was confirmed by Monte Carlo results.
- Each track has to give energy depositions in the forward detector planes such that in the $\Delta E - E$ distribution (see figure 7.3) the entry lies above the hyperbola shaped cut.
- No signal above pedestal in the veto counters was allowed.
- The energy depositions in the forward hodoscope planes may not deviate from each other by more than a factor of three.
- Every plane upstream from the last hit has to have a sufficiently high energy deposition.
- The third range hodoscope plane was used as a veto. At the present energy conditions the ^{3}He particles stop in the second FRH plane.
- Already online, at least 190 MeV energy deposition in the first range hodoscope plane was demanded during data taking at T_p=1276 MeV; at T_p=1250 MeV at least 130 MeV in the first range hodoscope plane was demanded and more than 3 MeV per hit in two of the three forward hodoscope planes.
- The final track has to be accepted by the kinematical fit routine, i.e. it was demanded that the kinematical fit procedure converged after 45 iteration steps.

If one of these conditions was not satisfied the track has been skipped.

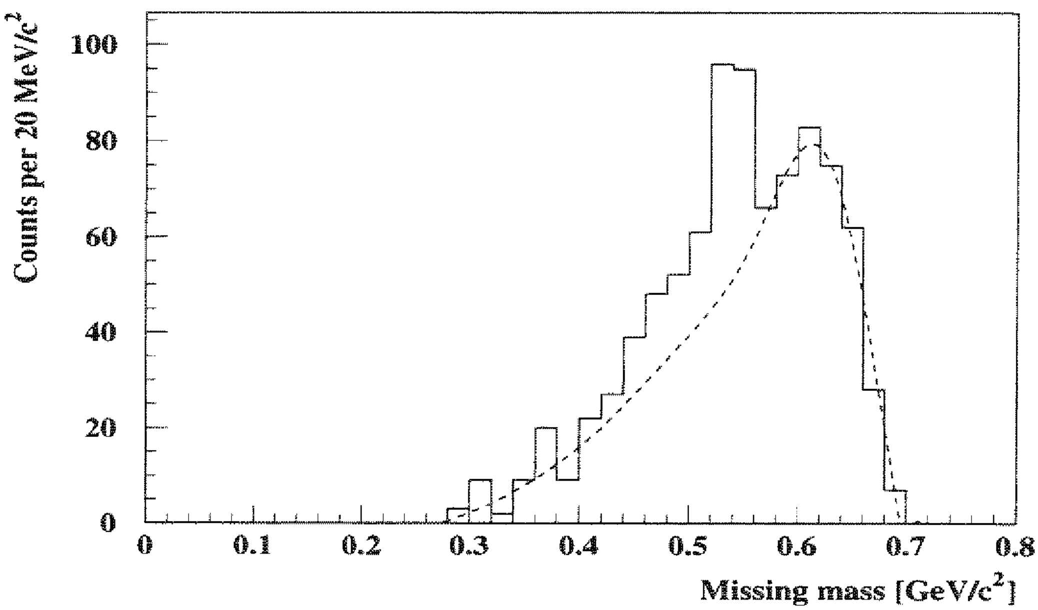

Figure 7.4: Missing mass distribution from ^{3}He tracks measured in the forward detector in p-d collisions at T_p=1250 MeV.

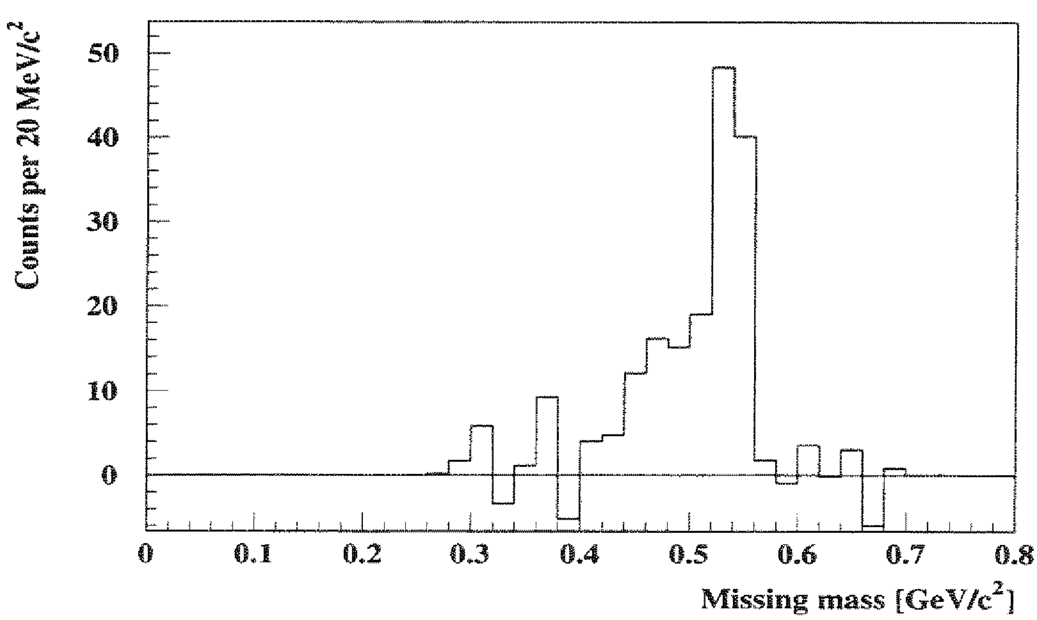

Figure 7.5: Missing mass distribution from figure 7.4 after background subtraction.

7.4 Internal timing

The intrinsic missing mass resolution of the forward detector is limited by the angular resolution which is determined by the pixel structure of the trigger hodoscope placed at a distance of 110 cm to the interaction vertex. One possibility for obtaining more information about the push-through point of a particle **within** a pixel is to look at the time information given by the three hit scintillators - one per hodoscope plane.

From the path length along the center line of a spiraled scintillator as described in section 3.2, a relation can be derived between the hit position, given by the plane polar coordinates r and φ, and the corresponding shift $\mathrm{d}t$ in the light collection time. One gets

$$\mathrm{d}r = \frac{1}{\sqrt{1+k^2r^2}}\, v\, \mathrm{d}t \tag{7.1}$$

and

$$\mathrm{d}\varphi = \pm\, k\, \mathrm{d}r, \tag{7.2}$$

where the positive sign is valid for the "left" bent scintillators and the negative for the "right" bent ones, and k is the constant defined in section 3.4. The velocity v of the scintillation light from its origin to the photomultiplier has $v_{max} = \frac{c}{n}$ as maximum, where c denotes the velocity of light and n the refractive index of the scintillator medium, i.e. $v_{max} = 19$ cm/ns. This maximum will be reached if the light travels to the photomultiplier without any reflection. In the limit of an infinite number of reflections at the surfaces of the scintillator medium the light velocity has $v_{min} = 0$ as lower limit. Experimentally, a mean velocity of (15.3 ± 1.2) cm/ns was extracted [14]. For the straight elements, the relation $\mathrm{d}r = v\ \mathrm{d}t$ holds on average. With respect to an improved missing mass calculation only the radial hit position is of interest which can, e.g., be determined by the bent scintillators.

Multiple reflection of the scintillation light is considered only to a certain extent by this primitive ansatz, but still this should be sufficient for a first estimate of the order of magnitude of a correction accessible by the time information. The order of the change in time within a pixel is expected as follows. All pixels have the same radial height of 4.83 cm, i.e. at the mean velocity given above the maximum time difference will be **315 ps** on average. In figure 7.6 the time difference spectrum between a left and a right bent scintillator is shown for a pixel at half hodoscope radius; the calibration factor is 50 ps per TDC channel. The difference of time signals rejects a possible jitter in the trigger timing. A gaussian fit to that distribution gives a σ-value of 7.8 channels, i.e. 390 ps, corresponding quite well to the time difference estimated above. The two-dimensional scatter plot 7.7 shows the TDC distribution of the right bent scintillator versus the time spectrum of the left bent one. Here one notices directly the dominant diagonal structure which is caused by hits where the run-time of the photons to the photomultipliers is equal for both elements. If the azimuthal angle of the push-through point varies, the path lengths to the respective photomultipliers are not equal anymore which should result in a deviation from this diagonal structure since a variation in the path length corresponds to a change

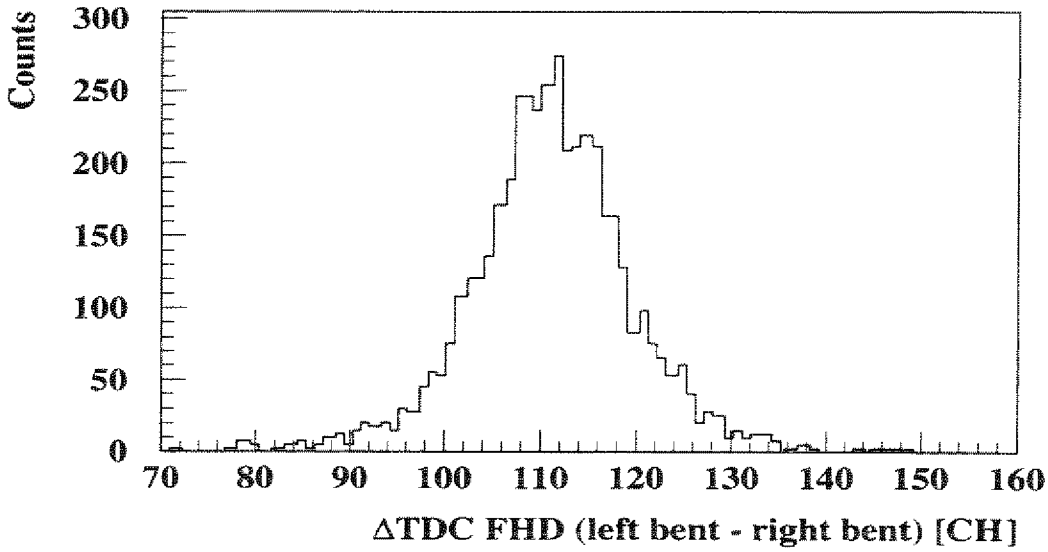

Figure 7.6: Time difference spectrum between left and right bent scintillator for one pixel at 31 cm hit radius. The calibration factor is 50 ps per TDC channel.

in TDC time. This means that the hit position information in one dimension (φ-direction) is given by the spread of the two-dimensional distribution in the direction perpendicular to the diagonal structure. However no such non-diagonal structure becomes visible here. Obviously, having a time resolution which corresponds to the run-time of the scintillation light along the dimensions of the pixel, one might only be able to see any off-diagonal structure in the scatter plot using extremely high statistics. In other words, the off-diagonal structure is hidden by the spread in timing. However, on principle an improvement in the calculation of the track direction, previously determined by the center-of-gravity of the respective pixel only, should be possible by correcting the hit coordinates according to equations 7.1 and 7.2 using the measured TDC times. As a first test, this method has been tried with the aim to visualize the geometrical shape of a pixel at half the radius of the trigger hodoscope, i.e. one and only one hit element was demanded in each one of the three FHD planes, by adjustment of the hit coordinates according to the measured times. Within the limits of the present statistics, only a broad spot was obtained and no triangle like structure was seen. As mentioned above, this is probably caused by multiple reflection of the scintillation light on its path to the photomultiplier. Thus an optical verification of the method in this way might on principle not be possible. However the missing mass distribution calculated from ^{3}He tracks in the forward detector could possibly be improved by adjusting the impact points of the measured tracks according to the time information. This has also been tried. The time corrected missing mass distribution for the data sample at T_p=1250 MeV is shown in figure 7.8 and the result after background subtraction in figure 7.9. In

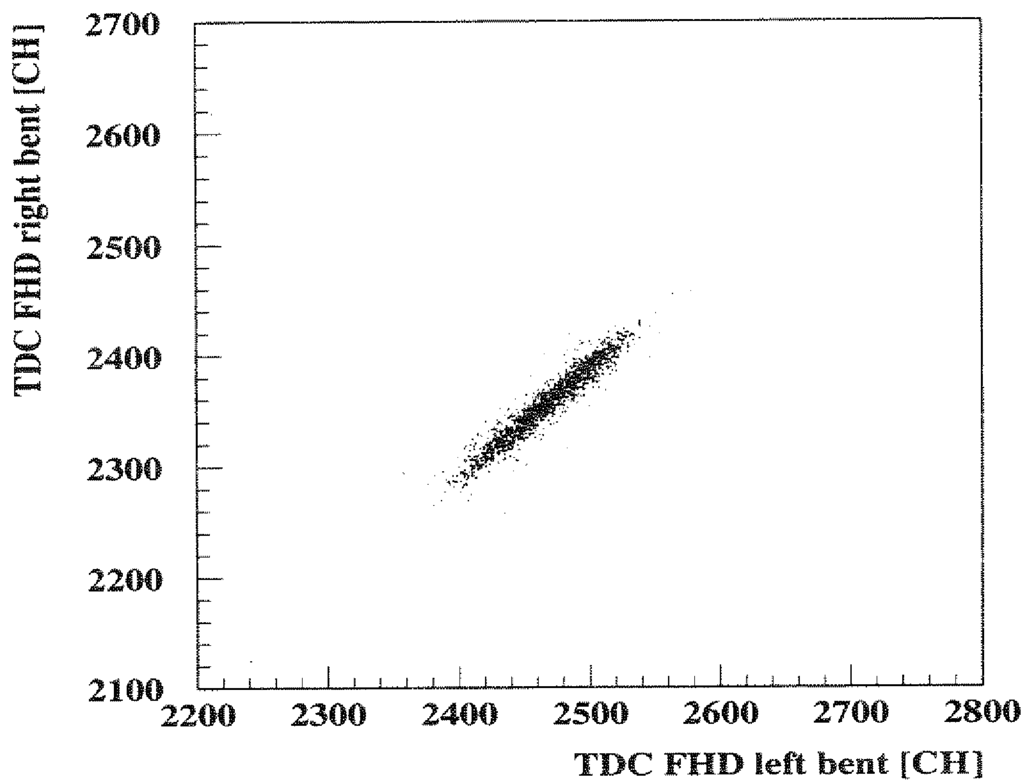

Figure 7.7: TDC spectrum of right versus left bent scintillator for one pixel (1 CH $\hat{=}$ 50 ps).

total 190 η's are found compared to 170 in the missing mass distribution without timing correction. Thus it seems to be possible to improve the resolution in track determination respectively missing mass calculation by an adjustment of the hit position according to the measured times.

Using information from the tracker, the results from time corrected hit positions can in the near future be compared to the track reconstruction with these straws which will give very reliable information about the direction of a charged particle track.

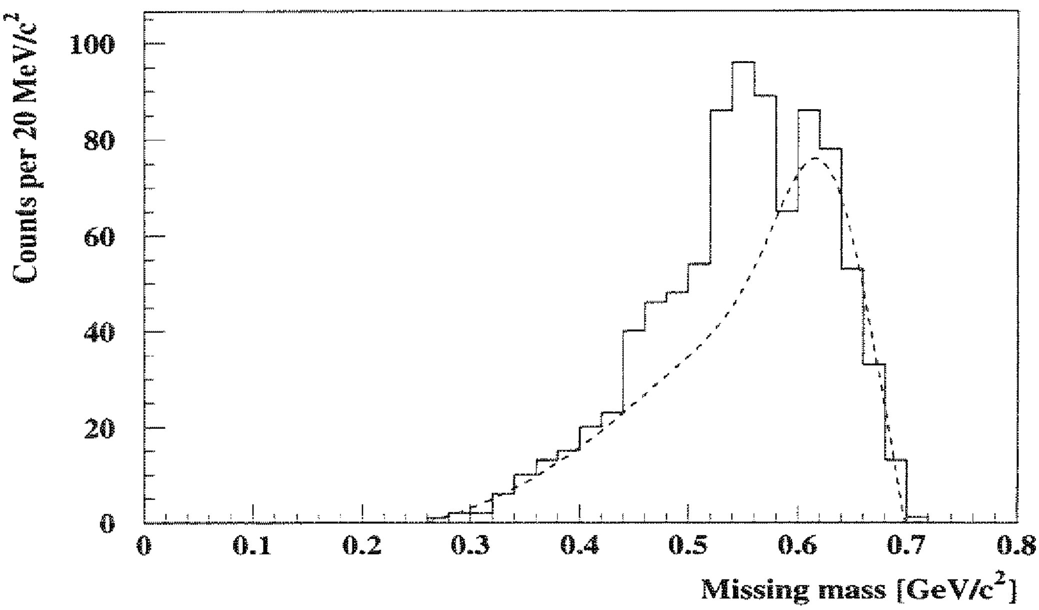

Figure 7.8: Missing mass distribution from ^{3}He tracks measured in the forward detector in p-d collisions at T_p=1250 MeV using time information in hit position determination.

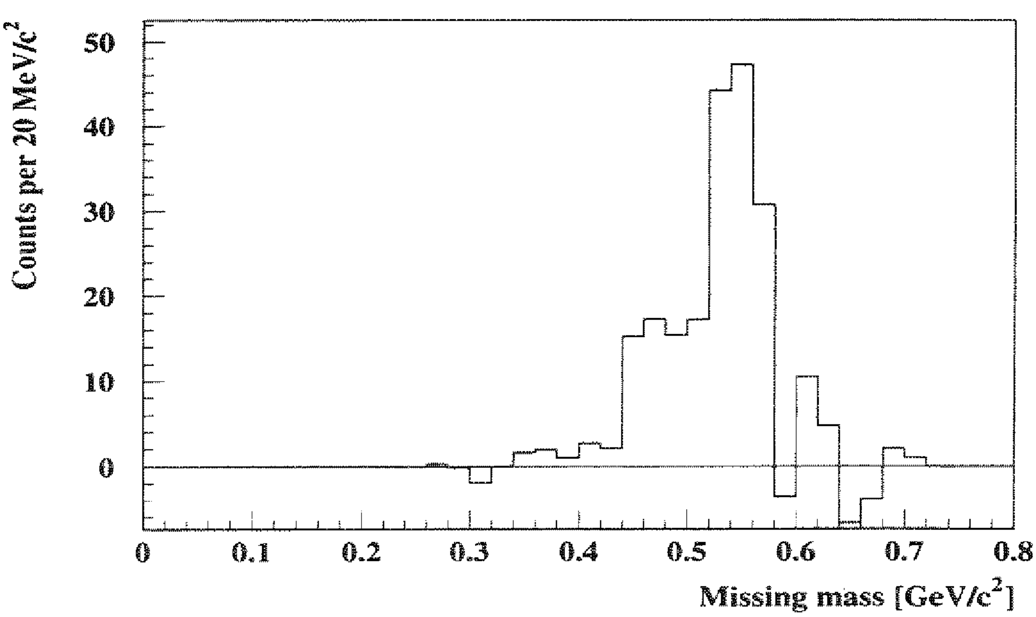

Figure 7.9: Missing mass distribution from figure 7.8 after background subtraction (time corrected).

7.5 Angular distribution of the η

If angular momentum quantum numbers shall be determined angular distributions have to be extracted. Here one is facing the main difficulty that a distinction between a pd$\rightarrow^3$Heη event and a pd$\rightarrow^3$HeX, where X stands for two up to five pions at this beam momentum (compare with figure 3.3), can not be made on an event by event basis. These two reaction types are on principle undistinguishable in ranges of the phase space where the missing mass for the multi-pion system is in the range of the η missing mass within the resolution of $\sim$ 80 MeV/c^2 (compare section 3.4.3). Thus a background subtraction can only be performed on a statistical basis. The channels ^{3}Heγ and ^{3}Heπ° do not play a role here as the missing mass spectrum (figure 7.4) indicates - the number of accepted events from these reactions is negligible compared to multi-pion production since the online veto on the third range hodoscope plane suppressed those reaction channels involving high energetic and thus long-range ^{3}He particles.

For all angular distributions shown below the result of the kinematical fit has been used. Since the statistics do not allow for a reasonable background fit in the two dimensional scatter plot of $\cos(\theta_X^{cm})$ versus the missing mass of the rest system, another method was applied. Six slices with a width of 70 MeV/c^2 each were cut out of the missing mass spectrum in order to extract the angular dependence of the background with respect to different mass regions. For each slice the angular distribution of the unmeasured neutral rest system (denoted as X) was calculated and is plotted in figure 7.10. Then the arithmetic mean of the angular distributions corresponding to the missing mass slice to the left and right of the one containing the η peak was taken as the "true" background distribution and is indicated by the shaded area in the "η" slice in figure 7.10 (mean of the distributions mid left and bottom left). The result after subtraction of this background is shown in figure 7.11.

This distribution has to be folded with the efficiency curve in figure 7.12 for the reaction pd$\rightarrow^3$Heη at this beam momentum including all online (e.g. trigger threshold cuts) and offline selection criteria. The efficiency curve was calculated in a full GEANT Monte Carlo run applying thresholds to the detector signals as they have been set during the online data taking. The energy depositions found were processed by the same offline data analysis chain as real data from the experiment. Finally the distribution was normalized to unit integral. Dividing by the efficiency gives the angular distribution shown in figure 7.13. The η center-of-momentum scattering angle is strongly forward peaked. The same was found in the analyis of data at T_p=1276 MeV (see figure 7.14). In figure 7.15 the η CMS angular distribution at T_p=1250 MeV is compared to the results for the same reaction at T_p=1450 MeV from reference [26]. The comparison is only meaningful for $\cos(\theta_\eta^{cm}) > 0.4$ since nearly all data points below are consistent with zero measured events within their errors from the experiment described here. In this region where the η mesons are favourably emitted in a forward cone ($\theta_\eta^{cm} < 66°$) the shapes of both angular distributions are

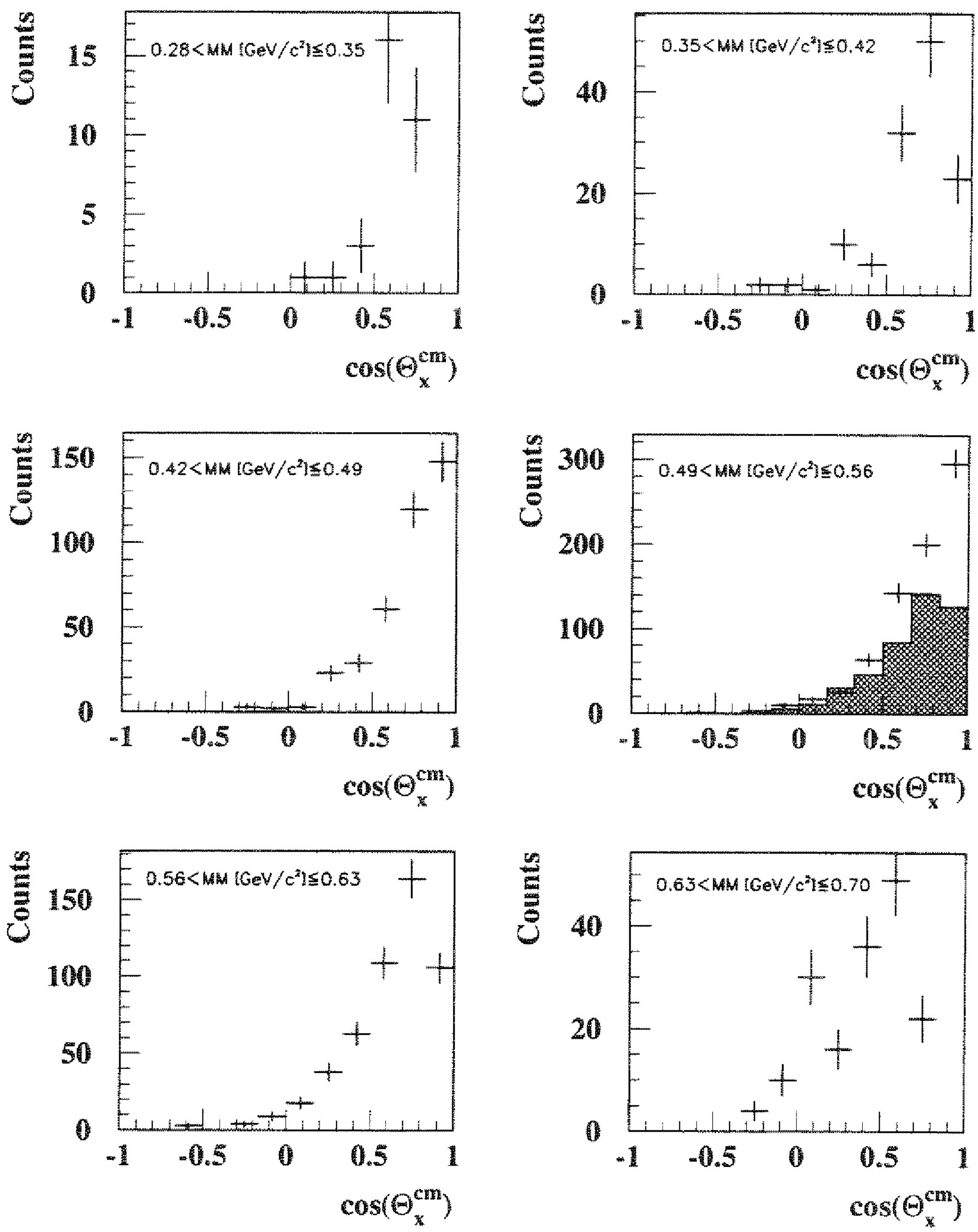

Figure 7.10: Angular distributions (CMS) of the unmeasured rest system in the reaction pd$\rightarrow$^{3}HeX for six missing mass ranges (T_p=1250 MeV).

similar to each other.

The fit functions shown in the final η CMS angular distributions are a superpo-

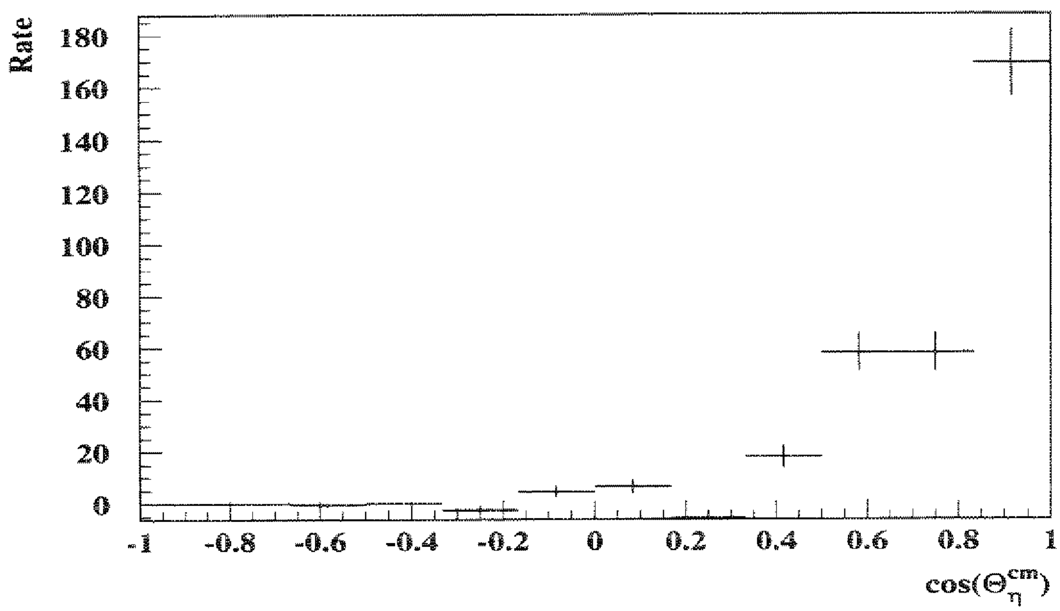

Figure 7.11: η angular distribution (T_p=1250 MeV) before efficiency correction. The ordinate shows events per bin after background subtraction, the bin size is 0.167 on the abscissa.

sition of Legendre polynomials up to 6th degree:

$$\frac{d\sigma}{d\Omega} = \sum_{n=0}^{6} A_n P_n(\cos\theta_\eta^{cm}).$$

These A_n are a measure for the contribution of different partial waves to the differential cross section as explained in more detail in appendix B. Pure s-wave production can be described by A_0 only, whereas p-waves involve amplitudes up to A_2 etc., i.e. $n \leq 2l$ where l is the angular momentum quantum number of the partial wave. Table 7.1 gives a list of the coefficients from Legendre fits to the η CMS angular distributions. Only the ratio of the coefficients with respect to the lowest order coefficient A_0 is meaningful since these quotients are independent of the cross section calibration ($A_0 \hat{=} \sigma_{tot}$). In figure 7.16 the Legendre fit coefficients for the two data samples, normalized to the lowest order coefficient, are shown together with their ratio (bottom). The lines are drawn just to guide the eye. The comparison of both data samples proves the consistency of the measurements since the data for both energies have been taken at different times, i.e. in the meantime the beam energy had been changed, and another target had been used (hydrogen). One may conclude that s-wave production is suppressed compared to p-waves or contributions from higher partial waves. Possibly, at the by only 2 % higher beam energy (1276 MeV compared to 1250 MeV) contributions from higher order partial

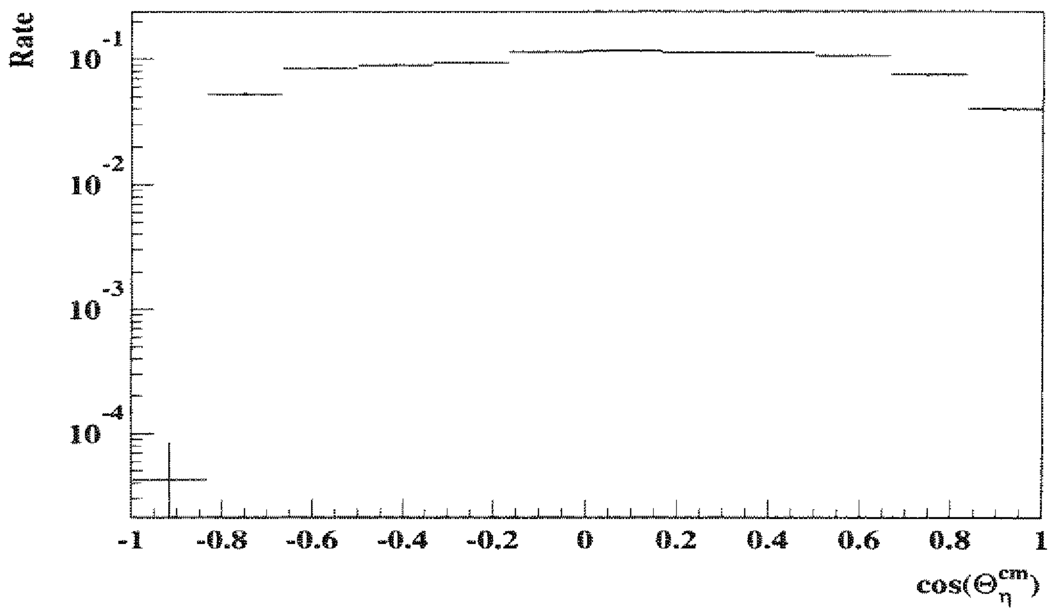

Figure 7.12: Efficiency curve (normalized to unit integral) for the η angular distribution (CMS) from the reaction pd$\to^3$Heη at T_p=1250 MeV.

waves slightly increase. The dominance of p-wave production corresponds very well to the experimental results from Saturne [2] (compare with figure 1.1). In these measurements a peak in the excitation function was clearly seen at a beam energy of T_p=1.3 GeV, corresponding to the threshold (on-shell excitation of the center of the resonance) for the reaction pd$\to$dN*(1710). In this picture, the resonance state of three nucleons then forms a ^{3}He nucleus with emission of an η meson from the N* decay. Figure 7.17 makes plausible that close to this threshold the production dynamics is expected to be dominated by the P_{11} resonance. Only two baryonic resonances are shown since these were experimentally found to couple strongly to the η meson. This is confirmed by table 7.2 which gives an overview [29] of the N* resonances (coupling of Δ resonances to the η is forbidden by isospin conservation). The (L>0)-resonances in the energy regime discussed here are candidates to explain the contributions from higher order partial waves found in the Legendre fits.

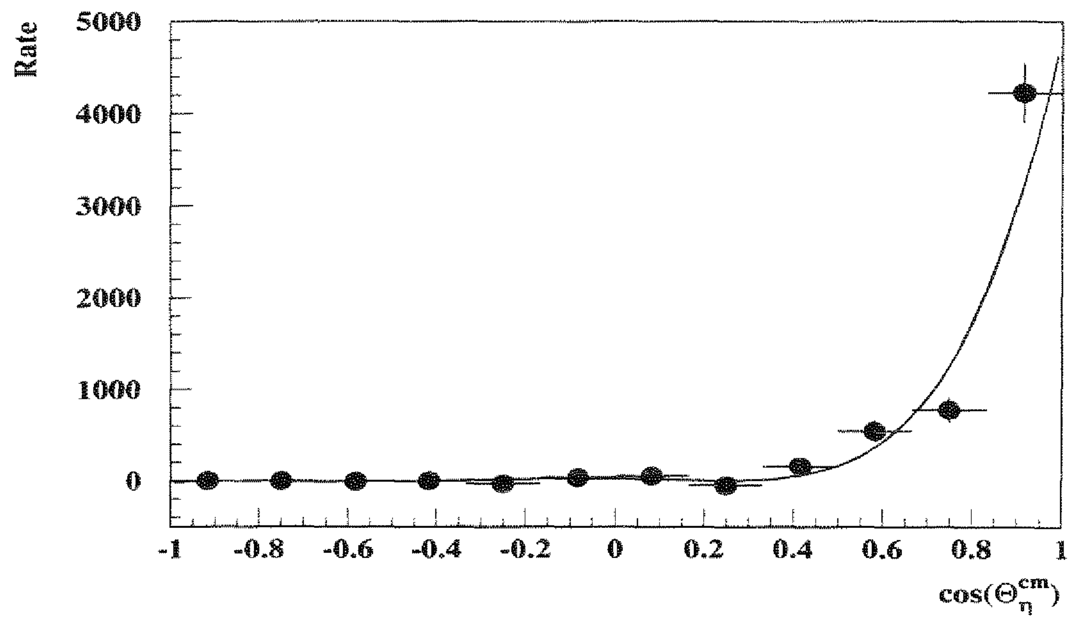

Figure 7.13: Acceptance corrected η angular distribution (CMS) from the reaction pd$\rightarrow$^{3}Heη at T_p=1250 MeV with Legendre fit.

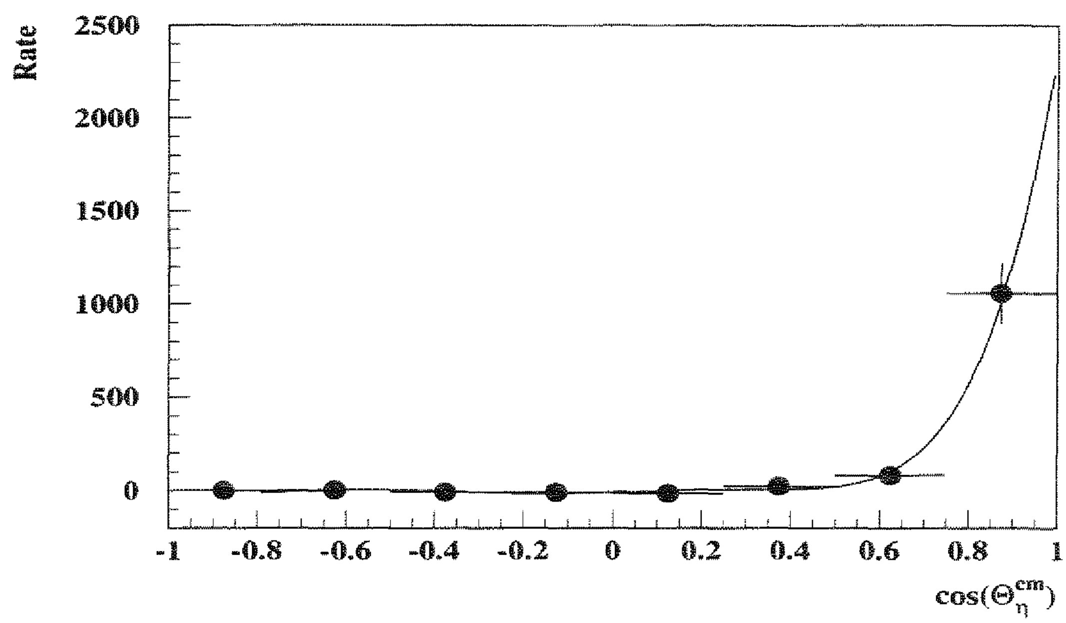

Figure 7.14: η angular distribution (CMS) from the reaction pd$\rightarrow$^{3}Heη at T_p=1276 MeV with Legendre fit (acceptance corrected).

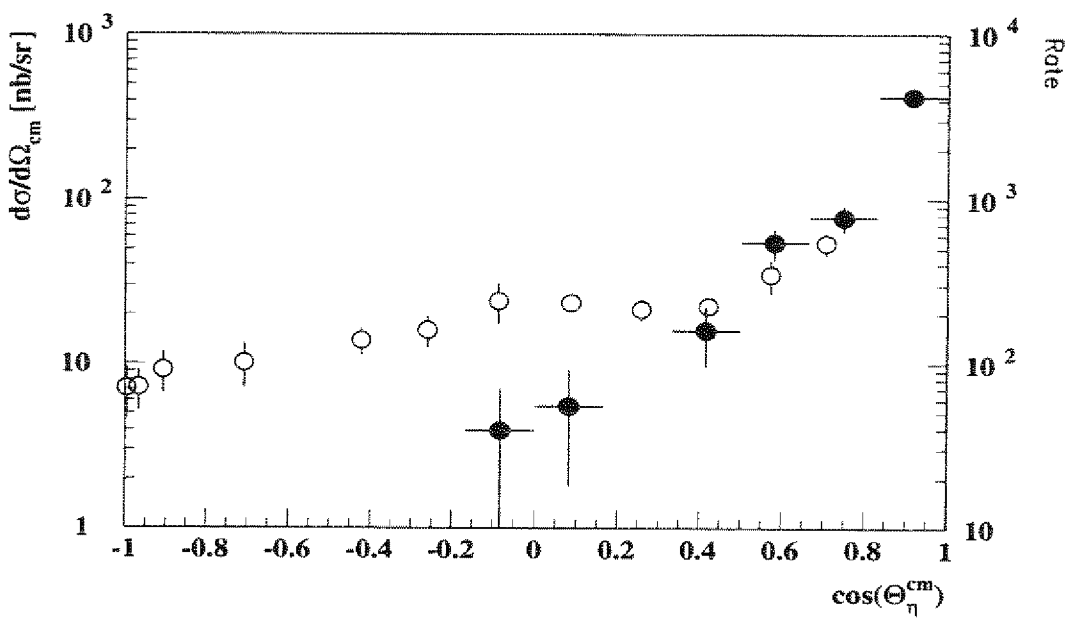

Figure 7.15: Comparison of the η CMS angular distribution at T_p=1250 MeV to the results for pd→^{3}Heη at T_p=1450 MeV from reference [26] (open circles).

T_p [MeV]	1250	1276
χ^2	6.43	2.00
A_1/A_0	2.537 ± 0.289	2.612 ± 0.271
A_2/A_0	3.021 ± 0.354	3.496 ± 0.330
A_3/A_0	2.556 ± 0.333	3.152 ± 0.331
A_4/A_0	1.570 ± 0.247	2.488 ± 0.387
A_5/A_0	0.610 ± 0.110	1.368 ± 0.281
A_6/A_0	0.069 ± 0.016	0.740 ± 0.366

Table 7.1: Coefficients from Legendre fits to the η CMS angular distributions.

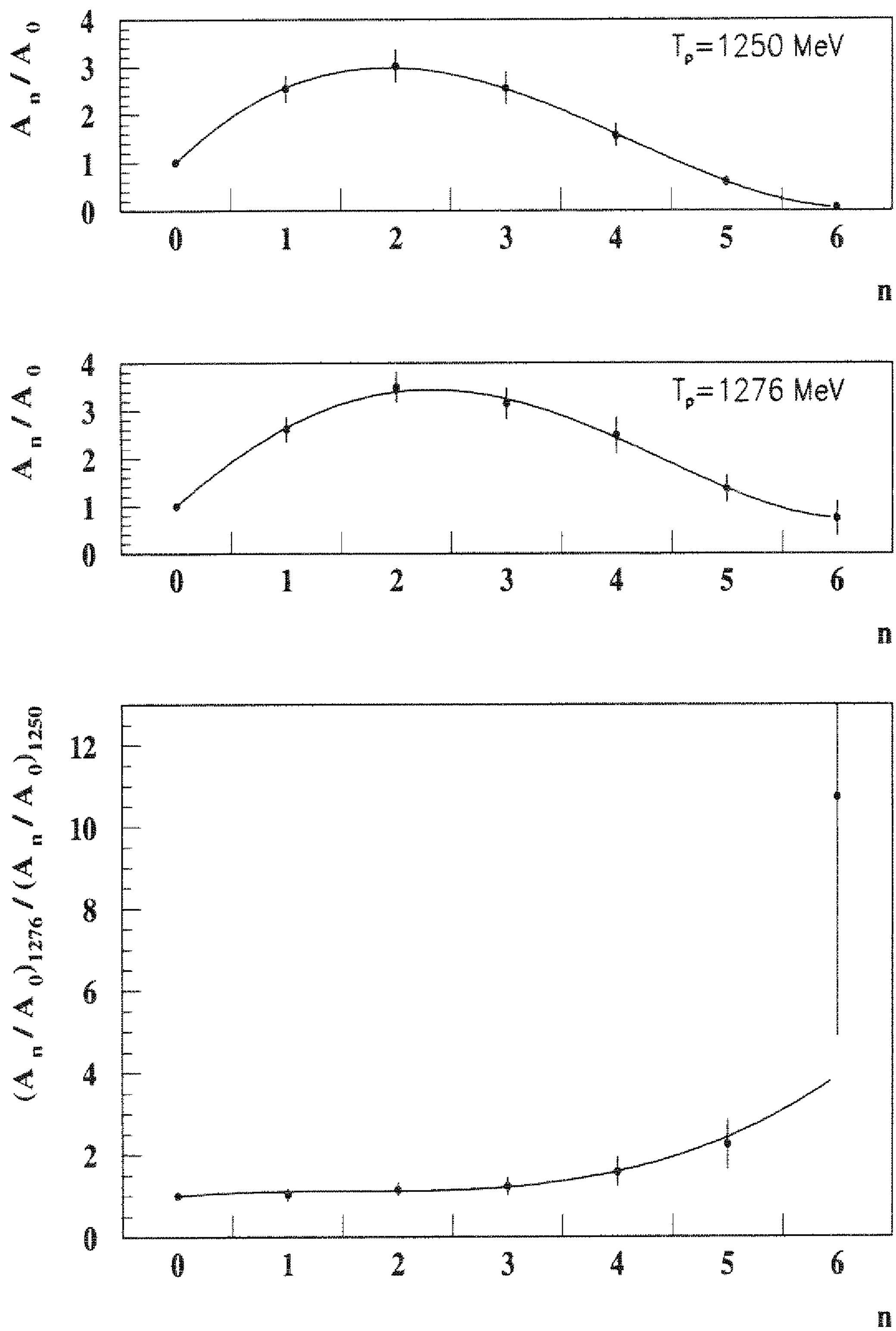

Figure 7.16: Statistics of the relative Legendre fit coefficients for the two beam energies and their ratio (bottom).

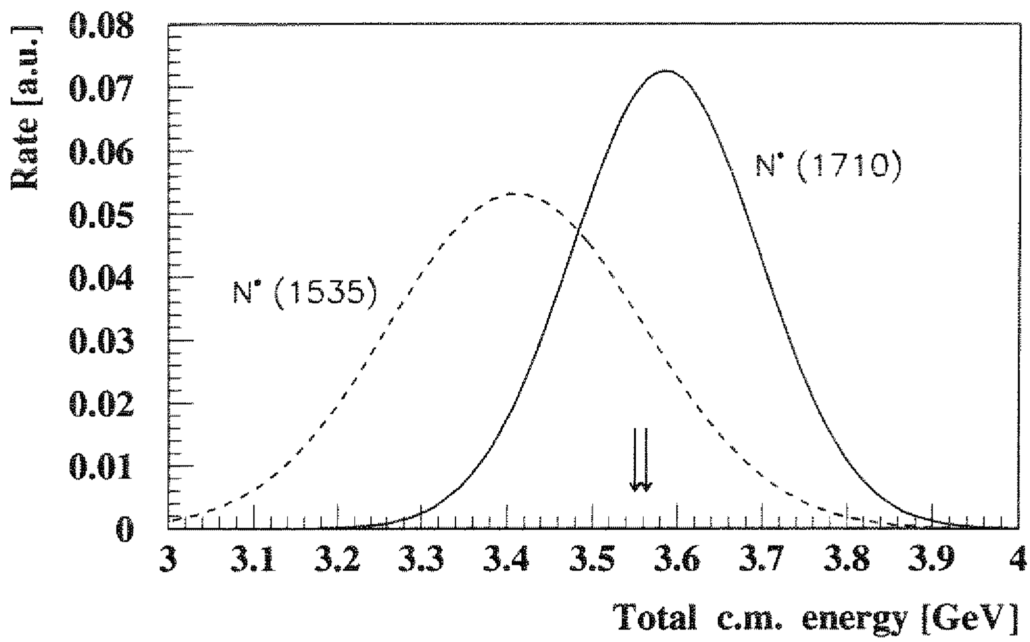

Figure 7.17: Position of the S_{11} $N^*(1535)$ and P_{11} $N^*(1710)$ resonance relative to the total center-of-mass energies available in this experiment indicated by the arrows. The resonances are centered at their respective thresholds in the reaction $pd \rightarrow dN^*$ and are normalized to unit integral.

Particle	$L_{2I\ 2J}$	Status as seen in		Branching ratio for decay into	
		$N\pi$	$N\eta$	$N\pi$	$N\eta$
$N^*(1440)$	P_{11}	$\star\star\star\star$	$\star$	50 - 70 %	
$N^*(1520)$	D_{13}	$\star\star\star\star$	$\star$	50 - 60 %	$\sim$ 0.1 %
$N^*(1535)$	S_{11}	$\star\star\star\star$	$\star\star\star\star$	35 - 50 %	45 - 55 %
$N^*(1540)$	P_{13}	$\star$			
$N^*(1650)$	S_{11}	$\star\star\star\star$	$\star$	55 - 65 %	$\sim$ 1.5 %
$N^*(1675)$	D_{15}	$\star\star\star\star$	$\star$	35 - 40 %	$\sim$ 1 %
$N^*(1680)$	F_{15}	$\star\star\star\star$		55 - 65 %	$<$ 1 %
$N^*(1700)$	D_{13}	$\star\star\star$	$\star$	5 - 15 %	$\sim$ 4 %
$N^*(1710)$	P_{11}	$\star\star\star$	$\star\star$	10 - 20 %	$\sim$ 25 %
$N^*(1720)$	P_{13}	$\star\star\star\star$	$\star$	10 - 20 %	$\sim$ 3.5 %
$N^*(1900)$	P_{13}	$\star$			
$N^*(1990)$	F_{17}	$\star\star$	$\star$		
$N^*(2000)$	F_{15}	$\star\star$	$\star$		
$N^*(2080)$	D_{13}	$\star\star$	$\star$		
$N^*(2090)$	S_{11}	$\star$			
$N^*(2100)$	P_{11}	$\star$			
$N^*(2190)$	G_{17}	$\star\star\star\star$	$\star$	$\sim$ 14 %	$\sim$ 3 %
$N^*(2200)$	D_{15}	$\star\star$	$\star$		
$N^*(2220)$	H_{19}	$\star\star\star\star$	$\star$	$\sim$ 18 %	$\sim$ 0.5 %
$N^*(2250)$	G_{19}	$\star\star\star\star$	$\star$	$\sim$ 10 %	$\sim$ 2 %
$N^*(2600)$	$I_{1\ 11}$	$\star\star\star$		$\sim$ 5 %	
$N^*(2700)$	$K_{1\ 13}$	$\star\star$			

Table 7.2: The status of the N^* resonances [29]. $\star\star\star\star$: existence is certain, $\star\star\star$: existence ranges from very likely to certain, $\star\star$: evidence of existence is only fair, $\star$: poor evidence of existence.

Chapter 8

Summary and outlook

The PROMICE detector - a subset of the future WASA 4π-detector - at the CELSIUS storage ring in Uppsala has successfully been used to study the production of η mesons in the reaction d(p,^{3}He)η at beam energies of T_p=1250 and 1276 MeV via both invariant mass determination of the two photons from the η decay [35] and the detection of the recoil ^{3}He nucleus. The double-charged ^{3}He particles were identified from the dE/dx information of the forward scintillator counters. On a broad background from multi-pion production, a clear η signal was observed in the missing mass distribution calculated from the forward detector tracks. Center-of-mass angular distributions have been extracted, and those events corresponding to missing mass values outside the range of the η missing mass peak have been used to interpolate the structure of the background in the "true" η sample. Extensive Monte Carlo simulations have been performed in order to calculate the total detection efficiency. The final angular distributions obtained after folding with the efficiency are strongly forward peaked, and Legendre fits indicate that at ~200 MeV excess energy s-wave is suppressed compared to p-wave or higher partial wave production. This is reasonable since the measurements were carried out close to a system where a P_{11} $N^*(1710)$ resonance with a width of ~110 MeV is embedded in a nucleus $\{dN^*\}$; the threshold for the reaction pd$\rightarrow$dN* (on-shell excitation of the center of the resonance) is at 1.3 GeV beam energy, whereas the threshold for the on-shell production of the S_{11} $N^*(1535)$ with a width of ~150 MeV is at a beam energy of 990 MeV in this reaction. The measurements at the two beam energies are consistent in a way that at the slightly higher energy also increasing contributions from higher partial waves were found.

Additional measurements of angular distributions at other beam energies would help to verify this resonance behaviour. In order to clearify the importance of resonances for η-production close to threshold reactions involving three particles in the exit channel should also be investigated since Dalitz plots can reveal information about intermediate resonance states. Furthermore the production of η mesons on targets with A>2 is of interest because an enhancement in the excitation function due to "velocity matching" only occurs with the deuteron as target. With increasing number of participating nucleons multi-step (cascade) processes will play a role in the meson production since they allow for an efficient sharing of the high momentum transfer. The WASA 4π-detector will in the future enable exclusive measurements of the reactions discussed here. This will improve the efficiency for studies of the intermediate formation of resonances, their role in the nuclear wave function and their importance for bound nuclear systems.

The earth has many riddles;
but it has as many solutions
which are a hundred times more beautiful than the riddles.

Martin Liechti

List of Figures

List of Tables

Bibliography

[1] F. D. Becchetti et al., NIM 138(1976)93.

[2] P. Berthet et al., Nucl. Phys. A 443(1985)589.

[3] J. Berger et al., Phys. Rev. Lett. 61(1988)919.

[4] BICRON corporation, "Physical constants of plastic scintillators", 1986.

[5] J. B. Birks, "The theory and practice of scintillation counting", Macmillan, New York, 1964.

[6] Y. Le Bornec and C. Wilkin, contribution to the workshop on "Baryon spectroscopy and the structure of the nucleon", Paris, internal report IPNO-DRE 91-36, 1991.

[7] D. Bour et al., "Study of η and η' production and interaction", COSY proposal 12, 1989.

[8] H. Brody et al., Phys. Rev. D 9(1974)1917.

[9] C. N. Chou, Phys. Rev. 87(1952)904.

[10] R. L. Craun and D. L. Smith, NIM 80(1970)239.

[11] A. Djaloeis et al., Phys. Rev. C 27(1983)2389.

[12] C. Ekström et al., Phys. Scr. T 22(1988)256.

[13] C. Ekström, contribution to the "CERN Accelerator School", Noordwijkerhout, 1991.

[14] A. Empl, Diploma thesis, KFA Jülich, Jül-Spez-510, 1989.

[15] Frodesen et al., "Probability and statistics in particle physics", Universitetsförlaget Bergen, 1979.

[16] J. F. Germond and C. Wilkin, J. Phys. G 15(1989)437.

[17] F. J. Gilman and R. Kauffman, Phys. Rev. D 36(1987)2761.

[18] T. J. Gooding and H. G. Pugh, NIM 7(1960)189.

[19] L. Gustafsson, Uppsala accelerator news 11, 1993.

[20] B. Höistad and T. Johansson (spokesmen), "Neutral meson production in light ion collisions", TSL proposal CA3, approved November 1988.

[21] S. Holm et al., Phys. Scr. 34(1986)513.

[22] A. Johansson and I. Zielinski (spokesmen), "Nuclear physics using WASA", TSL proposal CA4, approved November 1988.

[23] C. Kerboul et al., Phys. Lett. B 181(1986)28.

[24] K. Kilian and H. Nann, contribution to the workshop on "Particle production near threshold", Nashville, 1990, edited by H. Nann and E. J. Stephenson, AIP conference proceedings 221(1990)185.

[25] J. M. Laget and J. F. Lecolley, Phys. Rev. Lett. 61(1988)2069.

[26] E. Loireleux, PhD thesis, Paris University, IPNO-T 90-02, 1990.

[27] F. Osterfeld, KFA Jülich, private communication.

[28] J. M. Paul, NIM 96(1971)51.

[29] Particle data group, Phys. Rev. D 45(1992).

[30] F. Plouin et al., contribution to the workshop on "Production and decay of light mesons", Paris, 1988, edited by P. Fleury, World Scientific, 1988.

[31] F. Plouin et al., Phys. Lett. B 276(1992)526.

[32] N. A. Roe et al., Phys. Rev. D 41(1990)17.

[33] RÖHM GmbH, Datenblatt Plexiglas, Darmstadt, 1985.

[34] B. A. Ryan et al., Phys. Rev. D 3(1971)1.

[35] U. Schuberth, Uppsala University, private communication.

[36] J. Thimmel, Diploma thesis, KFA Jülich, Jül-2804, 1993.

[37] THORN EMI Electron Tubes Ltd., Catalogue, 1993.

Appendix A

Some more details about scintillators

A scintillator is any material that produces a pulse of light after the passage of a particle, i.e. after absorption of a part of its energy deposited in the scintillator material (**luminescence**). There are two types: inorganic crystals and organic scintillators.

Inorganic scintillators:

- Principle: Ionizing particles traversing the crystal produce free electrons and holes (excitons), which diffuse through the lattice until they are captured by an activator center. After recombination, the excited center emits light when it returns to the ground state.

- Advantage: transparency to their own radiation, light output larger than that of organic scintillators

- Disadvantage: long pulse duration ($\sim$ 1.5 μs) due to the long penetration time of the excitons in the crystal, and furthermore significant temperature dependence

Organic scintillators:

- Three main types: organic crystals, liquid scintillators and plastic scintillators

- Advantage: transparency to their own radiation, short output pulses, and emission spectra can be well adapted to the spectral sensitivity of the photomultiplier cathode using "wavelength shifters"

- Disadvantage: The light output saturates for large energy deposits.

A.1 Electronic structure of organic molecules

The structure of organic molecules is mainly determined by the structure of the carbon atom. The electronic configuration in the ground state is $1s^2 2s^2 2p^2$, but in forming compounds the electronic configuration appears to be $1s^2 2s 2p^3$, i.e. it has four valence electrons. These valence electrons are considered to be hybridized in three alternative configurations:

1. sp^3 hybridization (tetrahedral): In this configuration the four equivalent hybrid orbitals are directed towards the corners of a regular tetrahedron, i.e. they are inclined at equal angles of $109°28'$ to each other. These compounds are **not** luminescent.

2. sp^2 hybridization (trigonal): In this configuration one of the original p-orbitals is not changed, and three equivalent hybrid orbitals are produced which lie in the same plane, and are inclined at equal angles of $120°$ to each other. This configuration provides the ring structure of benzene and polycyclic aromatic hydrocarbons, which are planar molecules. The orbitals which are responsible for the binding in the hybrid plane are known as **σ-electrons** and the bonds as **σ-bonds**. The unchanged p-orbitals are mirror symmetric about the hybrid plane and are called **π-electrons** and the bonds **π-bonds**. Not only the σ-electrons can form bonds between the atoms, but also the π-electrons. These π-electrons achieve maximum interaction when their nodal planes are coplanar, i.e. the molecule is planar, producing an additional C-C-bond, known as a π-bond. In the cyclic ring structure of hydrocarbons, the π-electrons interact to form a common nodal plane. In this molecular orbital they are completely **delocalized**. The excited states of these π-electron systems are responsible for the luminescence effect.

3. sp hybridization (digonal): In this configuration two of the original p orbitals remain unchanged in the hybridization process, and two equivalent σ-orbitals are formed which are directed at $180°$ to each other. Also in this case the two p-orbitals can produce π-bonds. These triple-bonded molecules are also luminescent.

Often used as scintillator materials are so called **cata-condensed** hydrocarbons consisting of condensed systems of benzene rings in which no C atom belongs to more than two rings, and every C atom is on the periphery. Besides the singlet ground state and its excited states, there also exist triplet states among the electronic levels of an organic molecule with unpaired electron spins. Each electron level has a fine structure which corresponds to excited vibrational modes of the molecule (spacing between electron levels $\sim$ few eV, between vibrational levels $\sim$ few tenths of eV).

A.2 The scintillation process

Some part of the excitation energy deposited by a penetrating particle is released as radiation. The scintillation efficiency, i.e. the fraction of the deposited energy that appears as radiation, is of the order of 3.5 % (for anthracene, the best organic material). Absorption of the emitted light leads to an excitation of molecular levels, i.e. of the delocalized valence electrons in the π-molecular orbitals without changing the internuclear distances (Frank-Condon principle) due to the fact that the position of the energy bands does not change within the short transition times.

The photon absorption is constrained by multipole selection rules for electric dipole transitions, which inhibits transitions between singlet and triplet states. The electromagnetic interaction is parity conserving, so the singlet and the triplet state will have the same parity. Therefore the main component of the transition matrix, the dipole operator which is of the form $\vec{\varepsilon} \cdot \vec{r}$, will vanish. In other words, the parity equation $\pi_{\text{singlet}} = \pi_\gamma \pi_{\text{triplet}} = (-1)^l \pi_{\text{triplet}}$ (with l = angular momentum) cannot be satisfied with $l = 1$, so dipole radiation cannot contribute. Therefore this transition is strongly suppressed ($\sim 10^{-4}$). Thus only the singlet electronic modes as well as their vibrational modes are excited.

The higher singlet states decay immediately ($\leq$ 10ps), without emission of radiation, to the first excited singlet state ("internal degradation") by losing vibrational energy to the lattice ("phonon" emission). The efficiency for this process is near to 100 %. Due to the fact that the potential energy minimum of the ground state and the excited state are shifted in space, the emission of luminescence photons takes place in another wavelength region than the photon absorption. In other words, the first excited singlet state decays to excited vibrational states of the singlet ground state. In this process photons with lower energies are emitted than those which are necessary to populate the first excited singlet state from the ground state because the lowest vibrational sub-level of the ground state is the predominantly populated level at normal temperatures. Therefore the molecule is transparent to its own radiation.

There is also a certain probability for a non-radiative decay of the first excited singlet state to the ground state, called **quenching**. This process can occur if the energy difference between the excited and the ground state is in the region of the (thermal) vibration modes of the molecule. Then the molecule loses its energy mainly via this mode.

Besides the **fluorescence** process as described above, there also exists a similar process called **delayed fluorescence**, which also involves the triplet states of the molecule. The excited singlet states can undergo radiationless transitions into the triplet states ("inter-system crossing"). For the triplet states, there is a similar non-radiative degradation process, but the decay of the triplet to the singlet ground state is highly forbidden by multipole selection rules as mentioned above. Instead, the triplet ground state interacts with another triplet ground state leaving one molecule in the singlet ground state and the other in an excited singlet state (+phonons). The excited singlet state then decays as described into the ground state by emission of **delayed** photons with an identical spectrum to the fluorescence. The random excitation of the scintillator material leads to an exponential time dependence for the photon emission. Therefore, for the two components of scintillator light output, one can scribe

$$N = A \exp\left(-\frac{t}{\tau_{\mathrm{p}}}\right) + B \exp\left(-\frac{t}{\tau_{\mathrm{d}}}\right),$$

where τ_{p} and τ_{d} are decay constants for the prompt and delayed components, respectively. Here we've neglected the finite rise time of the light pulses. This cannot be ignored in the description of the extremely fast signals of plastic scintillators, which have decay constants of about $2-3$ ns. The time evolution of their output pulses is better described by

$$N(t) = N_{\circ} \exp\left(-\frac{t^2}{2\sigma^2}\right) \exp\left(-\frac{t}{\tau}\right),$$

where $\sigma \sim 0.5$ ns and $\tau \sim 2$ ns.

What has not been mentioned here, is the **phosphorescence**. Phosphorescence corresponds to a radiative transition from the long-lived (10^{-4}s up to a few seconds) triplet ground state to the singlet ground state. This is most readily observed in rigid solutions at low temperatures, where the non-radiative quenching process to the singlet ground state, which competes with the phosphorescence, is inhibited. The phosphorescence spectrum has longer wavelengths than fluorescence, but shows a similar vibrational structure, since the transition can occur into the various vibrational sub-levels of the singlet state.

The efficiency of light collection can be increased by the admixing of about 1 % of a "wavelength shifter". These are dye molecules which absorb the emitted photons from the scintillator and emit photons in a wavelength region that is well matched to the spectral acceptance of the photomultiplier, and also further decrease the probability for reabsorption of the photons in the scintillator. Loading, however, usually causes a lengthening of the decay time and a drop in light output because of quenching. But much of the quenching effect can be removed by adding naphthalene, biphenyl and other compounds to the solvent.

Plastic scintillators are the most widely used ones of the organic detectors today. They are so called "binary solution" scintillators containing two molecular species X and Y such that the lowest π-electronic excited states of the solute Y lie at lower excitation energies than the corresponding states of the solvent X.

The early stages of the scintillation process are similar to those in an unitary scintillator, i.e. primary excitation, ionization quenching and internal degradation of excitation energy take place as in an unitary system. The only major systematic differences are in the mechanisms of intermolecular energy transfer. The energy transfers from X^* to Y via a radiative or non-radiative process, and the probability for a non-radiative transfer increases with increasing solute concentration. In plastic scintillators, in which the π-electron systems which carry the solvent excitation energy are localized in individual aromatic segmers, X^* and Y remain effectively stationary, apart from possible Brownian rotation, and the transfer occurs by a long-range, radiationless dipole-dipole interaction process. Furthermore a higher concentration of solute will lead to a faster scintillation rise time.

Appendix B

Partial wave expansion

The differential cross section is the square of the scattering amplitude,

$$\frac{\mathrm{d}\sigma}{\mathrm{d}\Omega} = |f(k,\theta)|^2 ,$$

where k and θ are the center-of-mass momentum and scattering angle, respectively. This center-of-mass scattering amplitude $f(k,\theta)$ may be expanded in Legendre polynomials $P_l(\cos\theta)$,

$$f(k,\theta) = \frac{1}{k}\sum_{l=0}^{\infty}(2l+1)a_l P_l(\cos\theta),$$

with

$$a_l = \frac{\eta_l \exp(2i\delta_l) - 1}{2i}, \quad 0 \le \eta_l \le 1.$$

δ_l is the phase shift and a_l the scattering amplitude for the l^{th} partial wave [29]; these quantities depend on the form of the potential and the energy of the incident particle. The higher the particle energy the more partial waves may contribute. η_l is a measure for absorption out of the purely elastic channel; for elastic scattering $\eta_l = 1$ (unitary circle in the Argand diagram).

This expansion is possible since the Legendre Polynomials form a complete orthogonal basis, i.e.

$$\int P_l(\cos\theta)P_{l'}(\cos\theta)\mathrm{d}\Omega = \frac{4\pi\delta_{l,l'}}{2l+1},$$

where $\delta_{l,l'}$ is the delta function. Figure B.1 shows the Legendre polynomials up to 7^{th} order. The functions are defined as

$$P_n(x) = \frac{1}{2^n n!}\frac{\mathrm{d}^n}{\mathrm{d}x^n}\left(x^2-1\right)^n$$

and have n real intersection points with the x-axis in the interval [-1,1]. The first eight are

$$\begin{aligned} P_0(x) &= 1, \\ P_1(x) &= x, \\ P_2(x) &= \tfrac{1}{2}(3x^2 - 1), \\ P_3(x) &= \tfrac{1}{2}(5x^3 - 3x), \\ P_4(x) &= \tfrac{1}{8}(35x^4 - 30x^2 + 3), \\ P_5(x) &= \tfrac{1}{8}(63x^5 - 70x^3 + 15x), \\ P_6(x) &= \tfrac{1}{16}(231x^6 - 315x^4 + 105x^2 - 5) \text{ and} \\ P_7(x) &= \tfrac{1}{16}(429x^7 - 693x^5 + 315x^3 - 35x). \end{aligned}$$

The differential cross section contains interference terms between different Legendre polynomials $P_l(\cos\theta)$ and will therefore in general lead to asymmetric angular distributions. The optical theorem states that the total cross section is given by the imaginary part of the forward scattering amplitude,

$$\sigma_{\text{tot}} = \frac{4\pi}{k}\text{Im}f(k,0),$$

and thus the cross section of the l^{th} partial wave is bounded:

$$\sigma_l = \frac{4\pi}{k^2}(2l+1)\left|\frac{\eta_l \exp(2i\delta_l) - 1}{2i}\right|^2 \leq \frac{4\pi}{k^2}(2l+1).$$

If contributions from partial waves with $l > L$ are negligible, then the differential cross section can be written as a polynomial of degree $2L$. If on the other hand the experimental center-of-mass angular distribution can be well described by a fit with Legendre polynomials of degree up to $2L$,

$$\frac{d\sigma}{d\Omega} = \sum_{n=0}^{2L} A_n P_n(\cos\theta),$$

then mainly partial waves up to L^{th} order are involved. Pure s-wave production involves only $P_0(\cos\theta)$, i.e. the differential cross section is constant, $\frac{d\sigma}{d\Omega} = \frac{\sin^2\delta_0}{k^2}$, and thus the scattering is isotropic. p-wave production involves Legendre polynomials up to 2^{nd}, d-wave production up to 4^{th} degree etc.

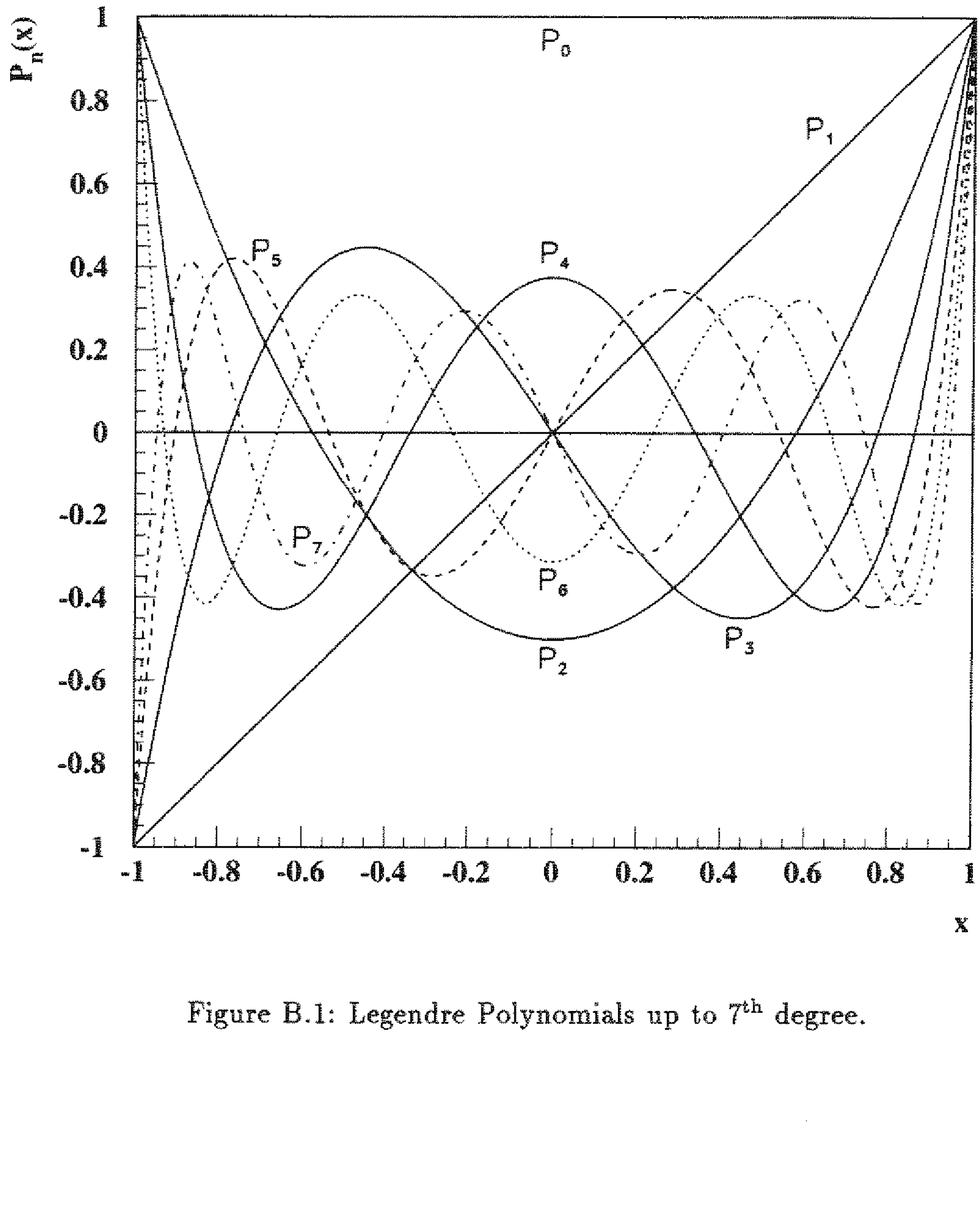

Figure B.1: Legendre Polynomials up to 7^{th} degree.

Acknowledgements

The complexity of medium energy physics experiments is inevitably connected with the constructive cooperation of a number of people. Unfortunately, not all of them can be mentioned here. In this place I shall therefore mention merely those people who significantly contributed to the enforcement of my thesis.

First of all, I like to thank my supervisor Dr. habil. Walter Oelert for the invaluable support he has provided throughout all phases of this work. His unconventional attitude, immense enthusiasm and encouragement were of great help. Thanks to you and your wife Brigitte for outstanding assistance and hospitality.

I am grateful to Prof. Dr. Kurt Kilian for stimulating discussions and the possibility to perform this graduation in his medium energy group.

The fruitful and joyful co-operation with Prof. Dr. Bo Höistad and Dr. habil. Tord Johansson I appreciate very much. Thanks for all your help and the pleasant working climate.

My co-supervisor in Uppsala, Dr. Hans Calén, I owe a deep debt of gratitude for his advice on how to design reliable, flexible and self-documenting computer code in a large software environment. Thanks for kindly answering stupid questions.

I have never met before secretaries as kind and helpful as Inger Ericson and Birgitta Holmgren. Thanks for your support and hospitality! Tusen tack Gun Lundin för att det fanns alltid kakor och kaffe. De underbara instituts utflykterna ska jag inte glömma bort.

I am very grateful for the friendly working climate among the members of the Uppsala group: Dr. Staffan Carius, Dr. Leif Gustafsson, Stina Häggström, Dr. Ib Koersner, Anders Mörtsell, Roger Ruber, Ulf Schuberth and Dr. Jozef Zlomanczuk. Thanks to all of you for your open minds and for giving me an inside into the bright side of northern life.

Special thanks are directed to the members of our medium energy group for the pleasant atmosphere and their humorous moral support: Ralf Bröders, Martin Dahmen, Dr. Eduard Roderburg, Michael Rook, Kirsten Sachs, Dr. Thomas Sefzick, Dr. Rüdiger Stratmann, and Magnus Wolke. Squash on thursday?

Thanks to Dr. Adam Turowiecki for his help during wrapping of the scintillators and Tracy Curtis for carefully profreadng the manuscript.

I am very thankful to my parents Ulrike and Leopold Waters for their everlasting support.

Last but not least I thank my girlfriend Monika Ostermann who has always been by my side and has given me all conceivable encouragement.

FORSCHUNGSZENTRUM JÜLICH GmbH

Jül-2917
Mai 1994
ISSN 0944-2952